UNIVERSITY OF LIVERPOOL

Adapting Numerical Models of Surface Barrier Discharges to Real-World Conditions

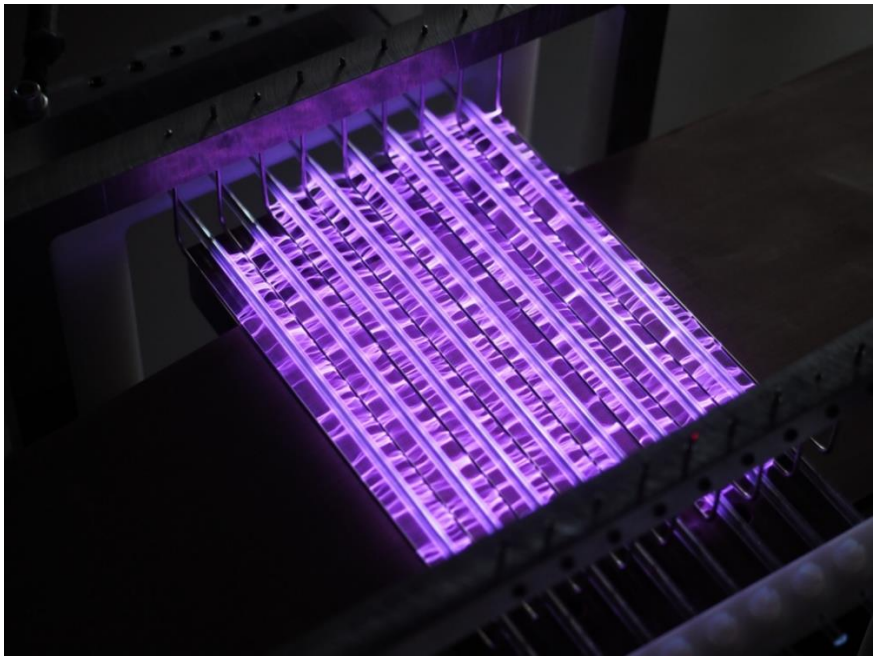

Thesis submitted in accordance with the requirements of the University of Liverpool for the degree of Doctor of Philosophy by:

Benjamin Gilbart

June 2022

Declaration

I hereby declare that the work displayed here is entirely my own; that it has not been submitted for any other professional qualification and that no information sources other than those referenced were used.

Abstract

The work described here aims to advance the numerical modelling used for Surface Barrier Discharges (SBDs) so that their design takes into account the non-idealised conditions encountered in real life. Starting from a two-dimensional fluid model of an SBD describing a single discharge gap, the model was used to analyse the effect of varying humidity on the species generated in the discharge. Furthermore, the model was upgraded to take into account heat transfer processes induced by the plasma, in addition to the mutual interaction between multiple discharge gaps when they are placed closely together. Wherever possible, the predictions of the model were compared to experimental data.

For any application of SBDs where ambient air is the working gas, humidity varies at different times of the day and during different seasons. Therefore, it is vital to understand how the variation in humidity affects the generation of Reactive Oxygen and Nitrogen species (RONS). This motivated the first investigation in this work, in which the humidity level was used as an input to the model and the behaviour of the resultant species was analysed as a function of humidity. It is reported that the densities of HNO_x species increase as humidity is increased, with the rate of increase slowing at higher humidity. Hydrogen-free species were only marginally influenced by humidity. These findings indicate that for applications where Hydrogen-free species are key, varying humidity from day to day is not a concern. For applications where HNO_x species are important, the application should use synthetic air with a controllable added H_2O fraction to maintain a steady dose of reactive species.

A second observation on the operation of SBDs in ambient air is the rapid rise in their temperature. Considering that many reaction coefficients are functions of gas temperature, it is vital to understand how the increase in gas temperature impacts the performance of the SBD as a source of reactive species. This motivated a key development made in this work which was incorporating heat transfer treatment into the SBD model. This was achieved by coupling the heat equation to the model. Two sources of heat were computed: the heat flux to the dielectric surface due to ion bombardment and the volumetric heat source in the gas due to inelastic collisions between the background gas and energetic electrons. The work revealed that ion bombardment was the primary heating mechanism of the dielectric. The impact of accounting for the increase in temperature was also investigated, where it was shown that it can cause a difference of up to 40% in the densities of some species, particularly the Reactive Nitrogen species (RNS). The impact of this finding is that it paves the way for controlling the long-lived species chemistry of the discharge by controlling the temperature of the dielectric. Consequently, for a practical application where Reactive Oxygen Species (ROS) are of interest,

active cooling of the dielectric is recommended, while for an application focused on RNS, active heating of the dielectric is advantageous. Another impact of this investigation was quantifying the errors in species density predictions from numerical models describing SBDs when the temperature effect is ignored, which were up to 40%.

The third aspect of SBDs applications investigated was the use of an SBD array, consisting of closely spaced discharge gaps, instead of a single discharge gap configuration as is typically used for research studies. The proximity of discharge gaps may induce emergent phenomena which cannot be observed in a single discharge. To capture such phenomena, the model was upgraded to investigate an array of 6 discharge gaps with a controllable distance between them. Supporting evidence was provided by Particle Image Velocimetry (PIV) experimental data. It was shown in this work that increasing the electrode width resulted in the discharge power decreasing exponentially for a fixed applied voltage. It was also shown that decreasing the distance between the discharge gaps forced flow vortices to overlap, creating a ripple in the flow downstream of the discharge, where the velocity varies by 200% from maximum to minimum value. This ripple has a significant impact on the flux of species to a downstream sample when the flux is convection dominated. These findings show that while bringing the sample to be treated closer to the SBD array increases the flux to it as it is convection dominated, it comes at the expense of uniformity. Thus, a trade-off must be made between the magnitude of the arriving flux to a sample and its uniformity.

Briefly, the work presented in this thesis provides a set of recommendations to be considered when designing an SBD for a particular application.

List of publications

(1) Gilbart, B. Dickenson, A. Walsh, J. L. Hasan, M. I. (2021) *Dominant Heating Mechanisms in Surface Barrier Discharges.* Journal of Applied Physics D, 54, 175202.

(2) Gilbart, B. Dickenson, A. Walsh, J. L. Hasan, M. I. (2022) *Mutual interaction among multiple Surface Barrier Discharges.* Plasma Processes and Polymers, 2100181.

Acknowledgements

I would like to express my sincerest thanks to my supervisor Dr Mohammad Hasan, for his input and guidance throughout my postgraduate studies. He has helped me develop my skills in numerical modelling, programme debugging and academic writing. I would also like to thank Dr James Walsh for his input on my academic papers and Dr Aaron Dickenson, who completed all of the experimental work presented in this thesis.

I would also like to thank all of my fellow students in office 310, who helped make post-graduate life tolerable and gave me perspective on my work numerous times.

I thank the University for providing me with the opportunity and the funding to pursue my PhD.

I'd like to thank my parents for encouraging me to pursue my scientific interests and for helping me find a way to afford them. Lastly, I am eternally indebted to Felicity Radomska, without her emotional support I would never have been able to complete my PhD.

Contents

List of figures

List of tables

1. Introduction

Plasma is the most basic state of matter, consisting of a quasi-neutral mixture of free positive and negative charges [1], which interact through binary collisions and the (longer-scale) electromagnetic force [2]. This contrasts with the 'standard' states of matter: solids, liquids and gases, which can interact through countless mechanisms, all of which are based on the four fundamental interactions: electromagnetic, strong nuclear, weak nuclear and gravitational. While plasmas experience the same four interactions, the standard states of matter have been studied much more thoroughly, as a result of being far more prevalent on earth, so understanding of their nature has advanced far further. Plasma, on the other hand, was only defined as a state of matter by Langmuir in 1927 [3] and, while there are many examples of naturally occurring plasmas, such as lightning, bioluminescence and flames, isolating them in a laboratory is more challenging. Plasma physics is a diverse scientific field encompassing astronomy, electromagnetism, nuclear physics, fluid dynamics, thermodynamics and material science. Plasmas are extremely common in space: nebulae, solar cores & coronas and interstellar dust are all examples [4]. In fact, some define plasmas to be 'any matter which emits light' [5], underlining their enormous physical significance. In a technological context, plasmas are found in nuclear fusion reactors, where they represent a potential sustainable energy source for the future [6], and in industrial applications such as surface coating [7], waste reformation [8], chemical activation [9] and lighting [10].

Focusing on technological plasmas, they can be divided into *thermal plasmas* and *non-thermal plasmas*; the latter are also known as *Low-Temperature Plasmas (LTPs)*. In both categories, the plasma can be thought of as a mixture of an electron fluid and a positive ion fluid, where each fluid has its own temperature. Thermal plasmas can be generated by heating the gas to a point where the gas constituents (either molecules or atoms) are energetic enough to cause ionisation, leading to the formation of the plasma. Consequently, the ion fluid is in thermal equilibrium with the electron fluid [11]. In low-temperature plasmas, an electric field is applied

that is strong enough to cause electrical breakdown to occur, converting the gas into a conductive media, leading to the formation of an electrical discharge in the gas. Since the energy is coupled to the electron fluid in this case, as will be explained in section 2.1, the electron fluid has a much higher temperature than the ion fluid which stays close to the ambient temperature, earning the name 'low-temperature' plasma. Because of this property, low-temperature plasmas can be used in applications involving heat-sensitive surfaces, such as human skin and materials with low melting temperatures, without the risk of thermally damaging the surfaces. Such applications include surface etching [12]; bacterial decontamination [13]; cutting [14] and even cancer therapy [15]. A more thorough review of low-temperature plasma applications is found in chapter 2.

In most cases, LTPs are weakly ionised, meaning that the electron and the ion fluids are diluted in a neutral background gas fluid. Typically, the densities of the electrons and the ions are approximately 10^{-6}-10^{-4} times that of the background gas [16], which has multiple implications. One is the dependence of the plasma properties on the background gas pressure. As the operating pressure is increased, the collisions between neutral atoms or molecules and charged species become more frequent than collisions among charged species. As a result, the transport of charged species in weakly ionised plasma is dominated by drift and diffusion, in contrast with the free acceleration of charged particles in an electric field [4]. Increasing the gas pressure also limits non-local physical processes such as plasma waves [4]. It also creates pathways for the generation of reactive species and allows for momentum transfer between charged species and the background gas, both of which are effects that will be discussed at length in this work.

1.1 Plasma parameters

In this section, a brief review of the plasma parameters relevant to the context of this work is given. The parameters covered here provide a mathematical description of the processes governing LTPs at atmospheric pressure.

1.1.1 *Plasma density and electron temperature*

While plasmas consist of a mixture of charged particles, the Coulomb force among the particles causes the plasma to be in a 'quasi-neutral' state, which prevents a strong electric field from forming in the bulk plasma in a similar manner to conductors. Mathematically, the concept of quasi-neutrality is expressed as $n_e = n_i$ where n_e (m^{-3}) is the electron density and n_i (m^{-3}) is the ion density. Since this equality holds, the ion and electron density can both be referred to as the plasma density. In fact, the plasma density and the electron temperature T_e (eV) are the necessary parameters to describe a wide range of plasma processes. Figure 1.1 shows the range of plasma density and electron temperature for a diverse range of plasmas.

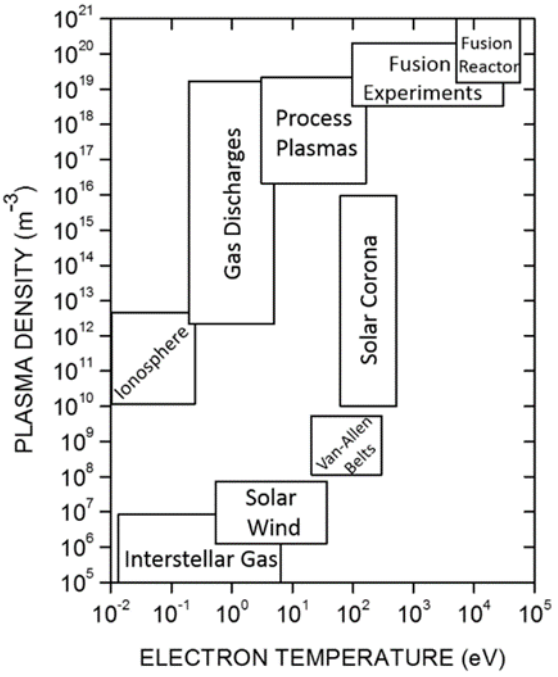

Figure 1.1: The plasma density and electron temperature of a wide range of plasmas [17].

Due to thermal charge fluctuations, the quasi-neutrality of the plasma can be temporarily broken, generating an electric field that extends over a characteristic length known as the Debye length, as given in equation (1.1).

$$\lambda_D = \sqrt{\frac{\varepsilon_0 T_e}{q_e n_e}} \tag{1.1}$$

In equation 1.1, λ_D is the Debye length (m), ε_0 is the free space permittivity, and q_e is the electron charge (C).

The importance of the Debye length becomes apparent when discussing plasma sheaths. When an electric field is applied at a boundary of the plasma bulk region, a charge separation is induced to shield the external applied electric field. Quasi-neutrality is broken in this region of charge separation which is known as the plasma *sheath*. It is characterised by the dominance of one of the charged species (positively or negatively charged) and a strong electric field. The sheath's width is typically 2-12 times the Debye length for a slightly ionised plasma [18, 19]. The existence of the sheath is critical for maintaining the quasi-neutrality of the bulk plasma, as without it, fast-moving electrons would quickly escape and the bulk plasma would be left with a positive charge.

1.1.2 *Boundary fluxes*

When gaseous species fill a volume. The flux of particles of species *s* crossing any given geometric surface is equal to the expression given in equation 1.2.

$$\Gamma_s = \frac{1}{4} n_s v_{th} \tag{1.2}$$

In equation 1.2, Γ_s is the normal flux across the boundary ($m^{-2} \cdot s^{-1}$), n_s is the density of species *s* (m^{-3}), and v_{th} is the thermal velocity of the species *s* ($m \cdot s^{-1}$) given by equation 1.3.

$$v_{th} = \sqrt{\frac{8 k_B T_g}{\pi m_s}} \tag{1.3}$$

In equation 1.3, k_B is the Boltzmann constant ($J \cdot K^{-1}$), T_g is the gas temperature (K), and m_s is the atomic mass of the species *s* (kg). When equations 1.2 and 1.3 are used to describe electrons the gas temperature is replaced with the electron temperature.

Assuming the mathematical surface splits the volume of the gas into a left volume and a right volume, the flux going from the left to the right volume is given by equation 1.2, which is also equal to the flux from the right to the left. Consequently, the net flux crossing the imaginary surface is 0. If the mathematical surface is constructed at the right wall of the chamber, the flux from the right to the left (from the wall into the gas volume) is 0 which means the flux of species leaving the domain at that boundary is equal to that given by equation 1.2.

1.1.3 *Mean free path and collisions*

The mean free path λ (m) is the average distance a particle travels between two consecutive collisions. It is given by equation 1.4 for a particle moving in a background of gas *n*.

$$\lambda = \frac{1}{n_g \sigma} \tag{1.4}$$

In equation 1.4, σ is the collisional cross-section (m^{-2}), which is a parameter determined by quantum mechanics to describe the probability of a specific type of collision. When multiple types of collisions are involved the overall mean free path can be computed using the sum of cross-sections. The cross-section is a function of the particles' energy as shown in figure 1.2.

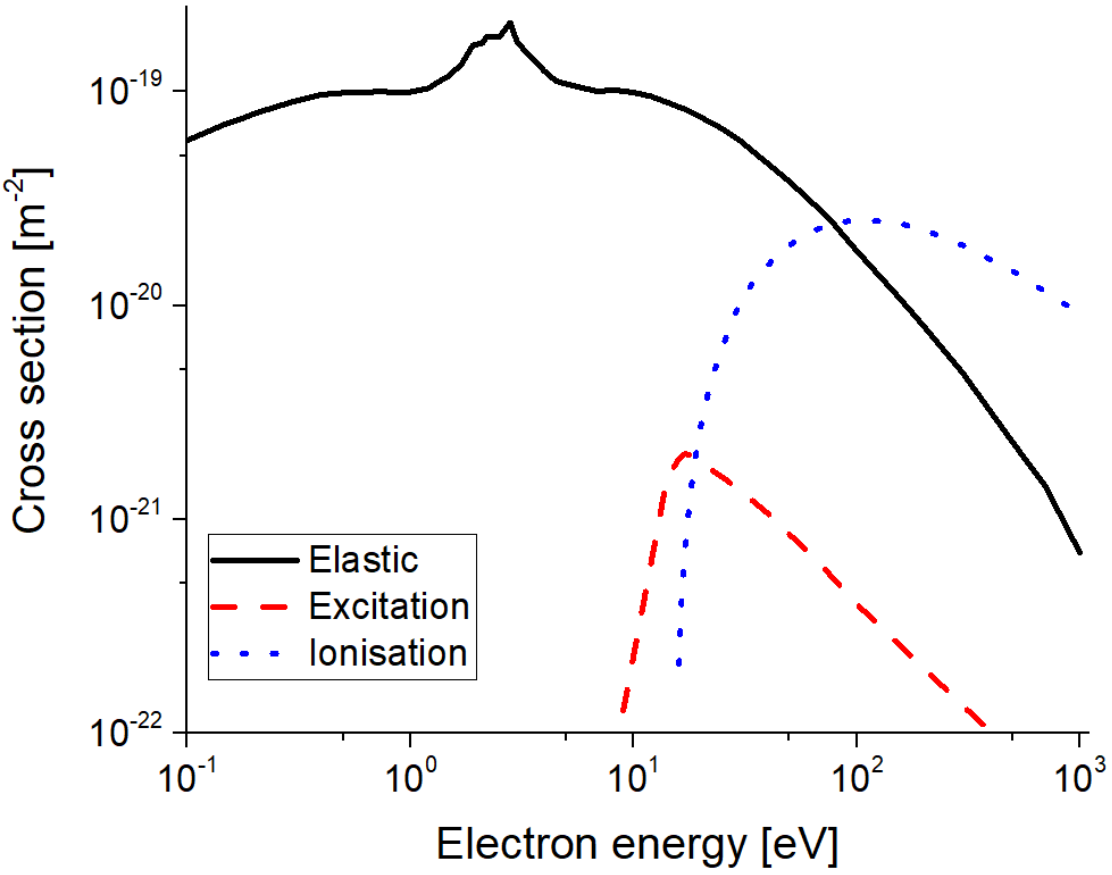

Figure 1.2: Electron cross-section for elastic, excitation, and ionisation collisions in nitrogen gas. The data is taken from [20].

Cross-sectional data not only varies by the type of the collision, it also varies with the background gas (i.e. helium, argon, or nitrogen) and the colliding particle (i.e. electron, He^+ ion or Ar^+ ion). Considering that the most probable species to deviate from the Maxwellian distribution function is the electrons, most collisional cross-section data available in the literature is for electrons.

By dividing the thermal velocity, given in equation 1.3, by the mean free path, given in equation 1.4, the collision frequency can be computed as is given in equation 1.5.

$$\nu_{Coll} = \frac{v_{th}}{\lambda} = n_g \sigma v_{th} \tag{1.5}$$

It should be noted that equation 1.5 is applicable to a species with a Maxwellian velocity distribution function. For a generalised case, equation 1.5 is modified as given in equation 1.6.

$$\nu_{Coll} = n_g \langle \sigma v \rangle \tag{1.6}$$

In equation 1.6 the angular brackets represent averaging over the velocity distribution function as indicated in equation 1.7.

$$\langle \sigma v \rangle = \int_0^\infty \sigma_{(v)} v f_{(v)} dv \tag{1.7}$$

In equation 1.7, $f_{(v)}$ is the velocity distribution function. The importance of the collisional frequency is that it is the main factor determining the transport coefficients of species in a collisional environment, namely the mobility and the diffusion coefficients, which are given in equations 1.8 and 1.9 respectively.

$$\mu_s = \frac{q_e}{m_s \nu_{Coll}} \tag{1.8}$$

$$D_s = \frac{k_B T_g}{m_s \nu_{Coll}} \tag{1.9}$$

In equations 1.8 and 1.9, μ_s and D_s are the electron mobility and the diffusion coefficient of the species *s* respectively.

1.2 Electrical breakdown

The process by which an insulating gas transforms into a conducting plasma is known as electrical breakdown. For any medium to conduct electricity it must have free electrons, which gases generally do not. Photons from cosmic rays, or other radiation sources, can produce photoelectrons in the gas. The electron densities generated by this process are not sufficient to conduct current. However, when a strong enough external electric field is applied, these photoelectrons are accelerated and gain enough energy to ionise the atoms in the background gas, thus releasing more electrons, which will, in turn, ionise another atom and so on. For a

given distance between two electrodes, the minimum applied voltage required to give the electrons enough energy to ionise atoms and thus lead to breakdown is called the *breakdown voltage*. This will also depend on the gas composition and the ambient temperature and pressure. The details of the breakdown process vary slightly among different discharge configurations but many of them overlap with the Townsend discharge mechanism.

1.2.1 *Townsend discharge mechanism*

First described by J.S. Townsend in 1910 [21], The Townsend discharge mechanism is based on the previous description of the initiation of the breakdown process, where an avalanche of electrons grows driven by an applied electric field. For the avalanche to be self-sustaining the mean free path of the electrons must be large enough for the electrons to acquire energy greater than the ionisation energy of the background gas [16]. For a parallel plate geometry where the voltage on one electrode is controlled while the other is grounded, increasing the pressure reduces the mean free path as equation 1.4 suggests, leading to an increase in the required voltage to achieve breakdown. A significant decrease in the pressure will increase the path length but will reduce the probability of collisions between the electrons and the background gas, making breakdown more difficult. This argument suggests the variation of the breakdown voltage as a function of the pressure is non-monotonic, a minimum exists at an intermediate value of the pressure.

This behaviour is manifested experimentally by the Paschen curves, which describe the variation of the breakdown voltage for a parallel plate geometry as a function of the product of the distance between the electrodes and the pressure of the gas [20]. Figure 1.3 shows the Paschen curves for different gases.

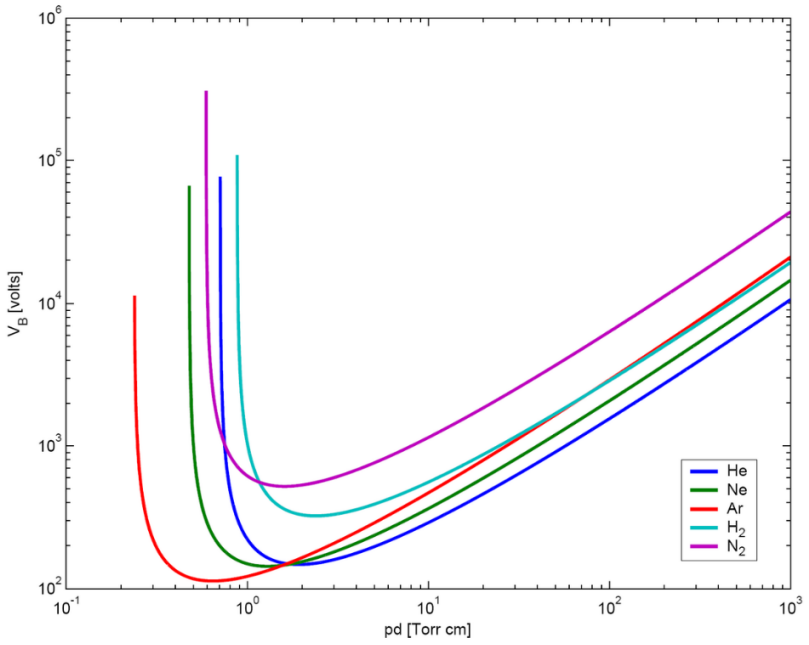

Figure 1.3: Paschen curves (Breakdown voltage against the product of pressure and electrode gap) of helium, argon, neon, hydrogen & nitrogen at room temperature [22].

As the electrons move in the direction of the applied field toward the anode and the ions move toward the cathode, it is expected that charged species will be depleted from the discharge gap as they hit the electrodes they are being attracted to and recombine. However, as the ions bombard the cathode, they release secondary electrons, which will then restart the avalanche process. In order for the process to sustain itself, each seed electron must produce an avalanche that leads to at least one secondary electron being emitted from the cathode. This is referred to as the *Condition for Ignition*.

The Townsend discharge mechanism implies the produced discharge is uniform in the direction perpendicular to the plates. Experimental evidence showed that this is not often the case [23]. For higher values of the product *pd*, discharges tend to have a filamentary structure [24], as can be seen in the case of lightning, which is the most obvious natural occurrence of an electric discharge. Moreover, multiple discharge configurations show a low sensitivity of the breakdown voltage toward the secondary emission coefficient of the cathode [25], suggesting alternative discharge mechanisms are possible.

1.2.2 *Streamers formation and the Meek criterion*

Although the Townsend discharge mechanism explained in section 1.2.1 seem to be applicable over a wide range of gas pressures and electrodes separation distances, it was experimentally observed that at higher pressure or larger discharge gaps the discharge ignites at times shorter than required for the ions to cross the discharge gap and sit secondary emission in effect [16]. The generated plasma in this case appears as an ensemble of linearly propagating charged species known as *streamers* [26].

Similar to the Townsend discharge mechanism, streamers start with an avalanche that grows exponentially in the discharge gap. Unlike the Townsend discharge, however, the growth of the avalanche becomes large enough to generate a significant charge density that alters the background electric field, causing a region of intense electric field to form at the head of the streamer, which occurs once the Meek criterion [28] is satisfied. Considering that ionisation is driven by strong electric fields, ionisation is enhanced in the streamer's head, leading to elongation of the plasma region. The charges concentrated in the streamer head drift in the applied electric field, thus causing the streamer's head to move. The continuous occurrence of the motion of the streamer's head and the formation of the plasma in that region causes a plasma channel to grow in the discharge gap, eventually connecting the anode and the cathode of the discharge. Depending on the polarity of the charge in the streamer's head, streamers can be categorised into anode-directed and cathode-directed streamers. In anode-directed streamers, the dominant charge in the streamer head is negative and, as a result, the streamer propagates from the cathode to the anode. In cathode-directed streamers, the dominant charge in the streamer head is positive and the streamer propagates from the anode to the cathode, as shown in figure 1.4.

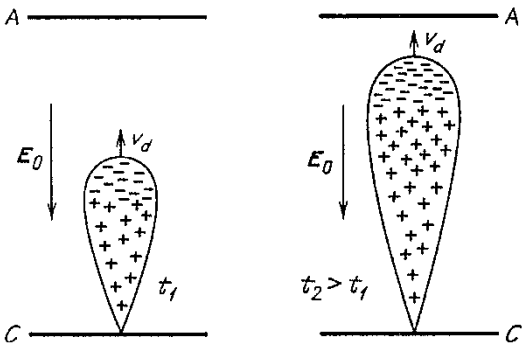

Figure 1.4: Schematic of an electron avalanche at two consecutive instances [27].

1.3 Electrical discharge devices

Over the years, many discharge configurations have been developed and characterised in the literature. Considering that the focus of this work is on low temperature plasma operating at atmospheric pressure, only devices under that category will be discussed here.

1.3.1 *Glow discharges*

Glow discharges devices are devices where the ignited plasma provides a conductive channel connecting the anode and the cathode of the device. The plasma is sustained by Ohmic heating of the electrons as current is conducted in the plasma channel. Typical devices falling under this category include pin-plate discharges and pin-pin discharges. Examples of these configurations are shown in figure 1.5.

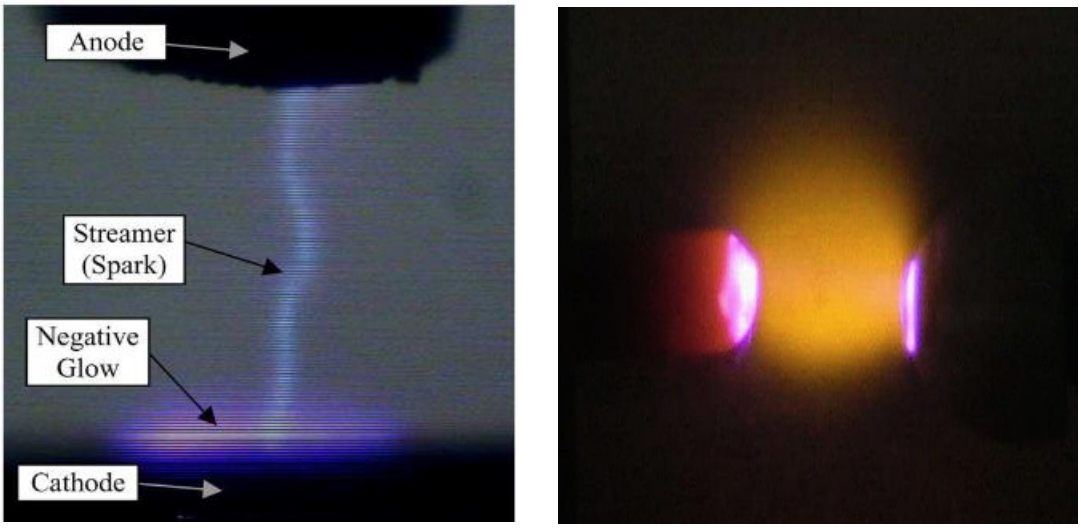

Figure 1.5: Examples of glow discharges at atmospheric pressure, the panel to the left shows a plasma channel in a pin-to-plate discharge [29]. The panel to the right shows a pin-pin discharge [30].

A common feature of glow discharges is their ability to draw large discharge currents. As a result, the discharges heat the background gas significantly causing a substantial increase in its temperature. When the discharge current increases beyond a certain limit the discharge transitions into arcing mode, which causes further heating of the gas and the electrodes. This may cause damage to the power supply if it is not capable of handling high currents. The background gas heating induces many instabilities which cause the plasma channel to branch into 'trees' of streamers [31]. Due to the elevated gas temperature and the instability of the plasma in this type of discharge, they are avoided when a thermally sensitive target is to be treated, or when a large surface requires a uniform treatment by the plasma.

1.3.2 *Dielectric barrier discharges*

In this category of devices, one or both electrodes are covered with a dielectric material, which affects the discharge in two ways. First, it suppresses arcing by allowing for a surface charge to

accumulate on the dielectric surface, which suppresses the delivery of current to a single point on the surface. Second, due to surface charge accumulation, the discharge strikes at a slightly different point every time it is ignited, which means that the plasma effectively spreads over a larger surface area. It also means that the plasma power dissipated by background gas heating is spread over a larger volume, leading to smaller increases in the background gas temperature. The surface charge build-up on the dielectric surface quickly creates a sufficient electric field opposing that produced by the electrodes that a discharge cannot be sustained. However, with an AC supply the electric field direction continually changes, so that the surface charge will support the applied field immediately after the change of direction. This effect lowers the breakdown voltage, making Dielectric Barrier Discharges (DBDs) more efficient than many other discharge devices.

In the last decade, the most commonly researched DBD, based on the number of papers published, was the plasma jet. Examples of this configuration are shown in figure 1.6. A noble gas is flowed through a hollow dielectric capillary typically made of quartz. One or two electrodes are mounted as shown in figure 1.6. When they are driven by a voltage source operating in the kHz range a long stable plasma plume is generated in the jet. Its length can extend up to 11 cm [32]. The gas temperature of this device is close to room temperature when helium is used as the operating gas [33]. Having these properties, plasma jets found many applications, particularly where high precision treatment is required such as in cell-level metastasis for cancer treatment [34]. For larger targets where uniform treatment is required, many attempts focused on scaling up plasma jets by creating an array of closely spaced jets. However, due to the mutual interaction among the jets the plasma seems to diverge, defeating the purpose of the plasma jet array [35].

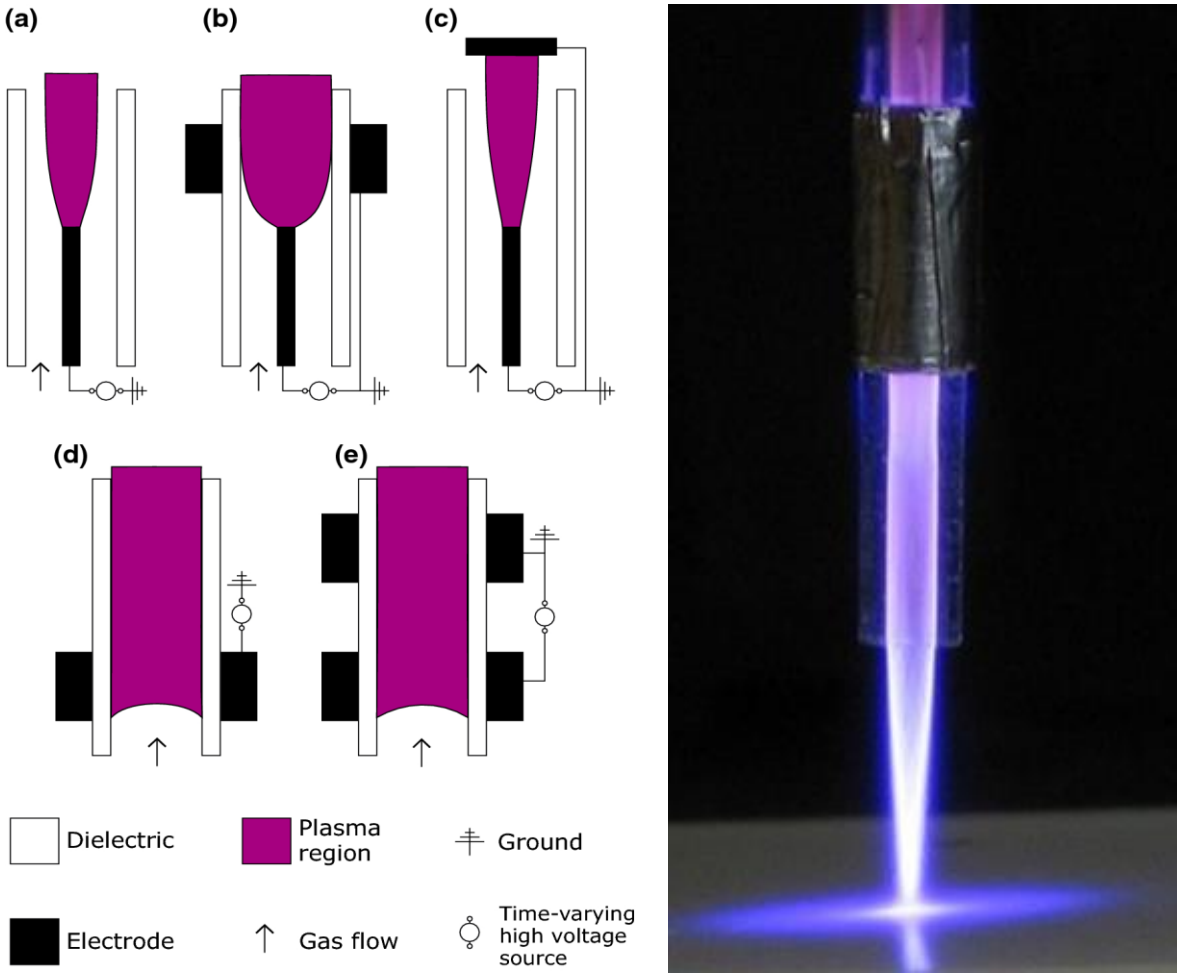

Figure 1.6: Examples of atmospheric plasma jet configurations, the panel to the left shows different electrode configurations for plasma jets [36]. The panel to the right shows an image of a plasma jet during operation [37].

Another common DBD device is the Surface Barrier Discharge (SBD). In this configuration, a dielectric is sandwiched between two electrodes. Next to one or more of the electrodes, gaps are left for the plasma to form, known as discharge gaps. The discharge gap can take many different shapes, they can be long strips [38], hexagonal [39], or circular [40, 41, 42]. Figure 1.7 shows the SBD configuration and images of different shapes of SBDs in operation.

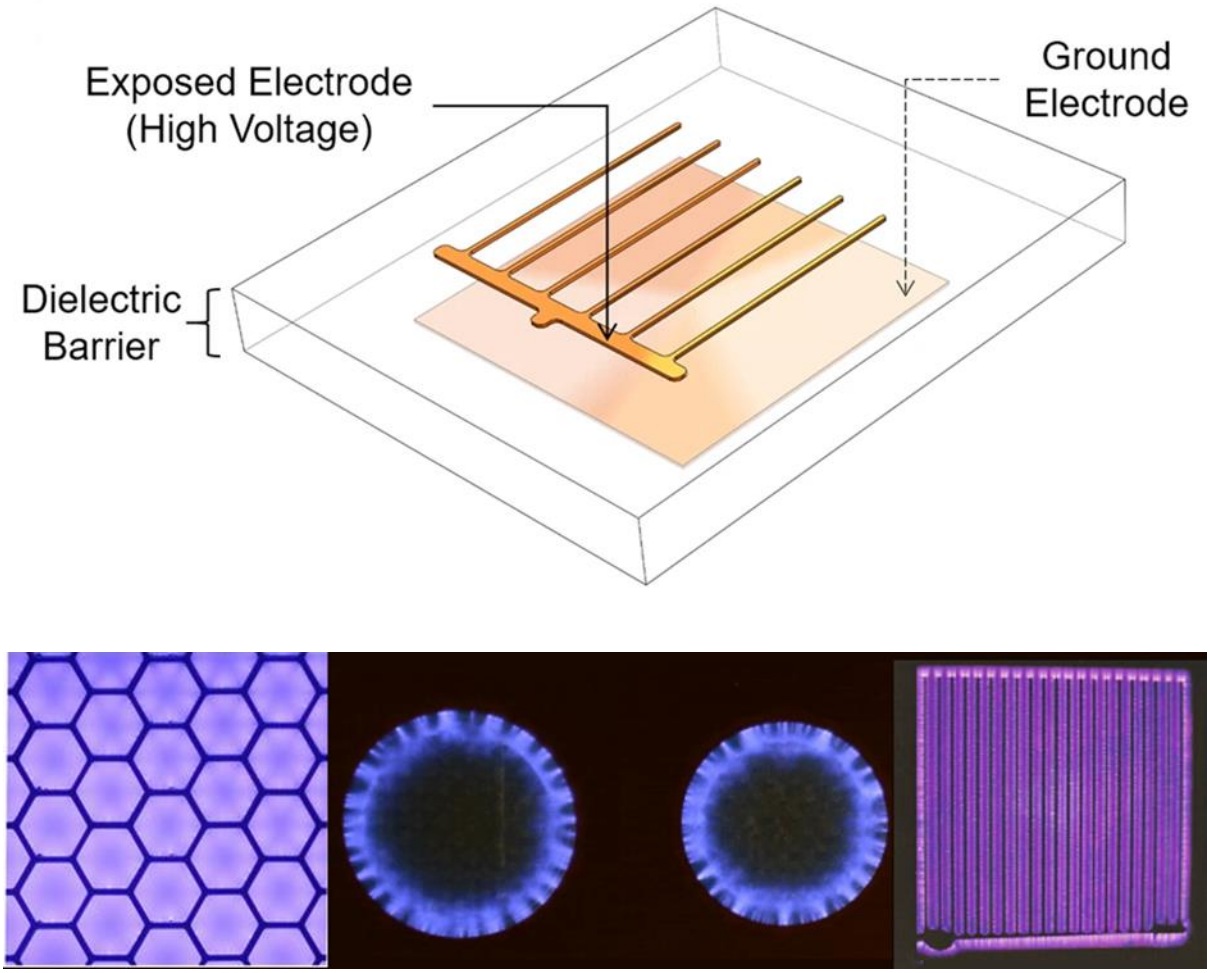

Figure 1.7: The top panel is a schematic of a typical Surface Barrier Discharge configuration [43]. The bottom panel shows plasma generated in discharge gaps with different shapes (left panel from [41], middle panel from our own observations and right panel from [42]).

SBDs operate typically with a few kVs as peak voltage, discharge power of tens of Watts and are typically driven by sources operating in the kHz range. In comparison to many other DBD configurations, SBDs are highly scalable and stable. Extending the treatable surface area can easily be achieved by increasing the surface area of the SBD. Unlike plasma jets, SBDs are a non-contact plasma source, which means that the plasma has no direct contact with the target to be treated. Reactive species generated in the discharge gaps are carried away to the target placed downstream by a combination of convection and diffusion as will be explained in this work. While SBDs can operate in any gas, they are primarily used with air as the working gas because the primary reason for their use is as a source of reactive species. When operating in air, the

temperature of the electrodes and the dielectric increases over extended periods of operation. The temperature of the surrounding gas however does not get as high as the electrodes. This means that SBDs can be used for thermally sensitive materials, though careful consideration of the operating power and the distance between the SBD and the target to be treated is still required.

1.3.3 *Other sources*

The sources covered in the previous subsections focused on sources that operate with DC or kHz power supplies. A number of other devices exist that operate in different frequency ranges including RF pencil discharges [44] and microwave discharges [45]. Other sources can operate in different discharge modes, for example, corona discharges [46] and gliding arc discharges [47], which operate when the discharge is in arc mode. In all these sources, the discharge dynamics are noticeably different from those of SBDs. Considering that the main focus of this work is on SBDs, details of the sources mentioned in this subsection will not be discussed any further.

1.4 Research motivation

Surface Barrier Discharges (SBDs) were heavily investigated in the 90s as they were used as sources of ozone, creating devices named 'ozonators' [48, 49, 50]. In the first decade of the 21st century, the focus of SBDs shifted toward their use as actuators, where they were used to alter the flow around a body to reduce drag and delay or prevent flow detachment [51]. In the last decade, the focus of SBD research has become their use as sources of reactive species. This focus was driven by many emerging technologies that relied heavily on SBDs, primarily in the field of plasma medicine [52, 53]. The conclusion arrived at in every emerging application is the need to establish correlations between the discharge parameters, such as the discharge power, and the resultant mixture of reactive species.

In this work, the aim was to develop a plasma model for SBDs to investigate many engineering aspects encountered in optimising SBDs for particular applications, which were not investigated before. Firstly, establishing a connection between the drawn power and the generated heat in the discharge configuration. This includes how this influences the chemistry of the discharge and the construction and optimisation of numerical models aiming to capture that. Secondly, this work investigates the effect of reducing the distance between electrodes in SBDs, and how that affects the resultant downstream flow field and the delivery of reactive species to a sample placed downstream. The conclusions presented in this work provide insight into how to design an SBD such that it operates at minimal gas temperatures and how to maximise the uniformity and the dose of reactive species flux to a sample downstream.

The thesis presents a thorough literature review on research into SBDs in chapter 2; a complete description of the construction of a numerical model and how it was adapted for my research in chapter 3. Chapters 4, 5 & 6 all present separate investigations performed using this model. The numerical findings in these chapters are supported by experimental results. All experiments presented in this thesis were performed by Dr. Aaron Dickenson on my behalf but all the modelling and analysis was my own work.

2. Literature review of surface barrier discharges

This chapter provides a review of developments in Surface Barrier Discharge (SBD) research. An overview of some of the applications for SBD devices is provided, before going on to summarise the key theoretical developments in the subject. These insights are divided into three sections: applications of SBDs, experimental SBD studies (diagnostics), and numerical SBD studies. In addition, open questions in the field are identified, justifying the choice of questions studied in the thesis.

SBDs are one of the most widely used low-temperature plasma sources, as can be seen by the number of research papers that describe using them. They are easily scalable, simple to construct and provide a wide range of reactive species. The basic premise is the same as when Siemens first used them to generate ozone in 1857 [1]. The geometry of a simple SBD is shown in Figure 2.1, consisting of a powered electrode sitting above a layer of dielectric material, which shields the grounded electrode. When the potential difference applied between the electrodes exceeds the breakdown voltage, a discharge is generated above the dielectric surface. This discharge is a weakly ionised low-temperature plasma with a typical ionisation degree of 10^{-6}. While this is a relatively small degree, it is enough to generate significant reactive species densities. Such reactive species are categorised into Reactive Oxygen Species (ROS) such as O, $O_2(^1\Delta)$, OH, H_2O_2, O_3 and Reactive Nitrogen Species (RNS) such as NO, NO_2 and HNO_3 [4].

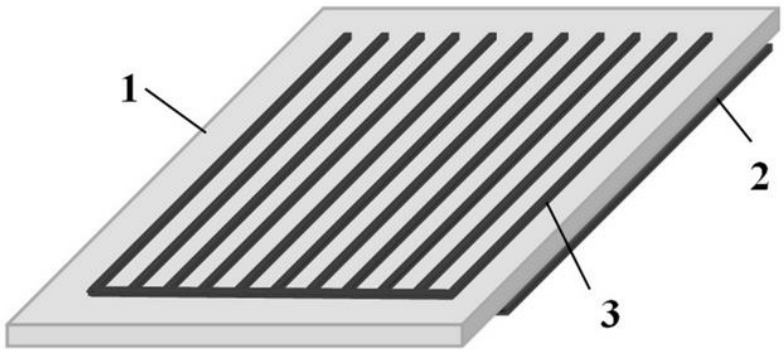

Figure 2.1: A schematic showing different parts of SBDs, 1. Dielectric, 2. Driven electrode, 3. Grounded electrode [7].

2.1 Applications of SBDs

The majority of the applications of SBDs stem from either their ability to produce RONS or their aerodynamic characteristics. The former is more common due to the wide range of applications for the different species generated in SBDs. The following subsections focus on different uses of SBDs.

2.1.1 *Biofilm treatment using SBDs*

SBDs are extremely effective in decontaminating biofilms, which are a thin layer of micro-organisms, consisting of connected biological cells that develop on many surfaces. Bacteria in biofilms are contained in extracellular polymeric substances, such as proteins, phospholipids and polysaccharides. Biofilms are much more resilient to unfavourable conditions than isolated bacteria, due to the strength with which they are bonded to each other and the host surface and their ability to store and share nutrients within the extracellular fluid encapsulating them [54]. It has been shown that the organisms within a biofilm communicate with each other, in order to react to their environment in a coordinated manner, through a mechanism known as quorum sensing [55]. Biofilms are believed to be the single most common cause of bacterial infections in humans and one of the most common contaminants in industrial settings [54]. However, due to their resilient qualities described above, many biofilms are extremely difficult to remove by conventional cleaning methods, due to their complex structures [55], cell adhesion mechanisms [56] and anti-biotic resistance [57]. As such, the well-documented success of cold atmospheric-pressure plasmas in destroying or de-activating them [56, 57, 58] has led to enormous development of their application in decontamination. The exact process by which cold plasmas destroy biofilms is still not fully understood, but it is known that many of the reactive species present in the plasma are bactericidal [57]. Species including ozone, atomic oxygen, hydroxyl radicals and peroxide are known to be involved in the deactivation of the biofilm. Moreover, reactive species generated by the plasma may diffuse in the extra-cellular matrix and interfere with quorum sensing within the biofilm [54]. This can prevent the biofilm from being able to

sustain itself. While this could potentially help destroy a biofilm, it is more likely this could be used to prevent the formation of a biofilm in the first place, as quorum sensing is essential for the biofilm to properly structure itself.

Examples of using SBDs to decontaminate biofilms include the work of Maisch et. al. [58], who reported that SBDs can cause 3-5 log reductions of *Candida albicans* biofilms after 10 minutes of exposure to the plasma. Matthes et. al. reported the treatment of *Pseudomonas aeruginosa* SG81 and *Staphylococcus epidermidis* biofilms [59], both of which typically grow on human wounds and hinder their healing. They reported high antimicrobial efficacy on biofilms of SBDs in comparison to CHX treatment. Salgado et. al. attempted to explain how SBDs destroy *Escherichia coli* biofilms [60], they reported that long-lived reactive species created by the plasma are not solely responsible for the observed microbial inactivation and that a synergistic effect between the generated UV by the discharge and the long-lived species is responsible for the decontamination effect of the SBD.

2.1.2 *Food processing using SBDs*

As a scalable and cheap source of cold plasma, SBDs have been used as a means of decontamination of food [61], which aims to elongate the shelf-life of food to minimise food waste [8]. SBDs are particularly appropriate for this task as they operate using atmospheric air, rather than a feed gas, such as argon, which is used by other cold plasma sources such as many plasma jets. They can also easily be made to cover a wide area by arranging them into an array of many discharges. In addition to biofilm deactivation, plasma treatment can also remove pesticide residue; deactivate enzymes; remove toxins and kill airborne pathogens. Studies have shown that plasma treatment not only ensures the safety of the food to eat but may prolong its subsequent shelf life as well [8]. Due to the minimal amount of heat produced by cold plasmas, this treatment has far less impact on the taste and texture of the treated food than other available sterilisation techniques. It is critical in such applications that the discharge transfers a uniform dosage of reactive species over a wide area while maintaining a low operating

temperature, so that a large volume of food can be sterilised up to the required standard. SBDs have been shown for example to extend the shelf life of chicken breast fillets to up to 13 days in comparison to conventional methods. Plasma treatment has also shown its ability to extend the shelf-life of Strawberries [62], tomatoes [63], and apples [64]. The underlying mechanism behind the shelf-elongation is by deactivating the bacteria that cause the decay of the different food products such as *Zygosaccharomyces rouxii* for apples [65], *Escherichia coli* for tomatoes, oranges and apples [63] and *Listeria innocua* for meat [66].

2.1.3 *Plasma medicine*

Alongside its use for food sterilisation, SBDs are regularly used for biomedical sterilisation, both of surgical equipment [67] and directly on human tissue, which are two of the primary focuses of the field of plasma medicine [68]. Plasma treatment can be split into direct treatment, where the plasma itself comes into contact with biological tissue and indirect treatment (SBDs fall under this category), where only the effluent (the gas and reactive species ejected from the active discharge region) of the discharge reaches the target surface. The use of SBDs for medical equipment is also sometimes split between bacterial decontamination, for which plasma has been used for a relatively long time now, and active treatment, where the generated species can assist the healing process through blood coagulation for example [69].

One of the key applications in this category is wound therapy, where it has been shown that direct application of a cold plasma to wounds in humans and animals can significantly improve average healing times[70, 71]. Garcia-Alcantara et. al. [72] showed that the reduction in healing duration is mainly due to the presence of reactive NO species, while Fridman [73] found that plasma treatment almost completely eliminated further infection of those wounds. The exact process which leads to the faster healing of wounds is still unknown, but it is likely that the absence of infections allows the body to heal the wound faster.

Atmospheric pressure plasmas, in general, have also been envisaged as a potential cancer therapy [74]. In addition to the effect of the reactive species, here the electric field produced by the discharge is the key. This may destroy tumour cells either due to the heat provided by the radiation they absorb, killing them via hyperthermia; or by making them permeable to toxic drugs [75]. However, other studies such as [76], suggest that reactive species do play a major role in cancer cell destruction through apoptosis or necrosis. Regardless of the process, the treatment must affect the malignant cells much more strongly than the normal ones, something which Zhang et. al. have shown to be the case [76], though the reasons for this are not fully understood. This is a technology that is still in the early stages of development, but, given how few side effects early studies have shown [77], it is a very promising one. Further advancements in Plasma medicine include dental care [78], anti-fungal treatment [79], high precision surgical scalpels using plasma cutting technology [80], tissue re-structuring through plasma etching [81] and sterilisation of anti-biotic resistant bacteria (such as MRSA) [82].

2.1.4 *Flow actuators*

One of the fields where SBDs are the main discharge configuration used is flow control. The physical mechanism behind this application is known as the electrohydrodynamic (EHD) force [83]. Considering that ions drift in the electric field instead of accelerating, as was explained in chapter 1, the momentum lost by the ions drifting in the direction of the electric field is gained by the background gas, creating the so-called 'ionic wind'. This wind can then influence the flow of air (or fluids) surrounding the discharge. Devices exploiting this effect are called plasma actuators [84]. One of their most common applications is improving the performance of aerofoils, particularly aircraft wings. In aerofoil flow, vortices and turbulence are created behind the aerofoil once the air flow is separated, which create drag. Actuators can be strategically placed to reattach the airflow, reducing the drag. In some cases, they are deliberately placed to produce lifting vortices on the upper surface of the aerofoil, increasing the lift produced [85]. Other groups have considered the ionic wind as a potential source of propulsion [86],

potentially leading to the development of electric aeroplanes [87]. Further applications of SBD flow control could see it used to pump fluids through pipes more efficiently [88]; reduce CO_2 emissions from cars and trains [84] and as active noise control [89].

2.1.5 *Other applications*

SBDs are also capable of generating heat, the mechanics of which are explored in detail later in chapter 5. A few groups have found applications for this, most notably in de-icing aircraft wings [90]. They are also sometimes used to produce lighting [10], process fluids (such as to create plasma-activated water [9]) and remove pollutants from the air. With such an enormous array of applications, it is no surprise that SBDs are a very heavily researched area. The above review makes it clear that to develop applications, two aspects are most crucial. Understanding the chemistry of the discharge, including how it will change in different environments, and understanding how changing control parameters will alter the discharge.

2.2 Experimental studies of SBDs

While a large proportion of research into SBDs has focused squarely on their applications, knowledge of their behaviour in the laboratory is crucial so that they can be optimised for a specific application. This section provides an overview of some key experimental findings in recent years, highlighting how operating parameters can be used to control the discharge, how chemical regimes can change and where open questions remain.

In the past, experimental studies of atmospheric pressure discharges relied primarily on chemical analysis (through optical emission spectroscopy [91], Raman scattering [44] and mass spectrometry [92]) and measurements of the current, voltage and dissipated power in the discharge gap [14]. In the last 20 years, advanced diagnostic techniques became widely available for research groups. While the older techniques were sufficient to provide some insight into the chemical makeup and general dynamics of the discharge; they were not capable of providing accurate values of key plasma parameters such as species densities and reduced

electric field strength, or induced background gas flow. The following subsections review the most used diagnostic techniques and discuss their findings when applied to SBDs.

2.2.1 *ICCD cameras*

ICCD stands for Intensified Charge-Coupled Devices, which consist of an array of small capacitors allowing for a charge to be transferred to other circuits in the circuit based on the driving electric circuit [93]. Without going into further details about how ICCD cameras operate, their main feature is their ability to take images on timescales as small as picoseconds [93].

Examining SBDs with ICCD cameras revealed that the plasma consists of multiple filaments rather than a singular volume discharge being created. The filaments are typically generated on both the surface of the dielectric and in the gap between the electrodes. The nature, development and interaction of these filaments are the subjects of a large proportion of the research in this field. Streamers form in the gap and propagate along a channel, leaving behind an electrically charged area. This makes it easier for future streamers to propagate along the same path, even if the discharge has not been active for several seconds. This is known as the *memory effect*. The number of filaments created has been shown to be proportional to the amplitude of the applied voltage between the electrodes, but the charge transfer involved in each microdischarge remains unchanged [94]. Individual filaments are seen to exhibit particle-like behaviour: they can move, collide with other particles and boundaries, interact and disappear [95]. Filaments have been seen to self-organise into stripe, spiral and hexagonal patterns, reflecting structures seen in other cases of reaction-diffusion systems. The structure of the filaments depends on discharge parameters including the transverse diffusion coefficient, the inter-pulse decay rate of the discharge particles and the particle production rate. The parameters are sensitively dependent on the control parameters of an SBD such as pressure, temperature, electrode separation and the applied voltage waveform. As such, the structure can be controlled and predicted, but only a small error in the setup can produce a change in

structure, due to the sensitivity of the dependence. Such difficulties are typical in the field of non-linear dynamics.

It has been shown [95] that different discharge regimes can co-exist. For example, a diffuse (Townsend) volume discharge can often surround a filamentary (glow) discharge. This is likely to be due to the different strengths of current in different regions of the discharge and at different times during a half-cycle. A Townsend discharge typically requires less current, while a glow discharge requires more. This co-existence of different discharge regimes makes them even harder to predict and model. While this co-existence has been observed, no group has yet attempted to determine if there is any interaction between the two regimes.

2.2.2 *Spectroscopic techniques*

To quantify the chemical species generated in SBDs, many spectroscopic techniques have been used. The most widely used is Fourier Transform Infrared Spectroscopy FTIR [96], where the absorbance of the gas media is determined as a function of the wavelength in the infra-red region of the electromagnetic spectrum, then the peaks of absorbance are correlated with vibrational frequencies of specific species in the gaseous sample. Using the Beer-Lambert law it is possible to quantify the presence of a given species in the gaseous cell. Another spectroscopic technique commonly used in SBDs is Ultraviolet Absorption, which also depends on the absorption of the gas sample but in the Ultraviolet region instead of the infrared region [97].

Both techniques were extensively used to study the reactive species generated in SBDs as functions of the discharge parameters. For example, Pavlovich et. al. conducted a characterisation study focusing on how NOx species evolve in an SBD discharge as functions of discharge power density and time [97]. An example showing the evolution of 4 species is depicted in figure 2.2.

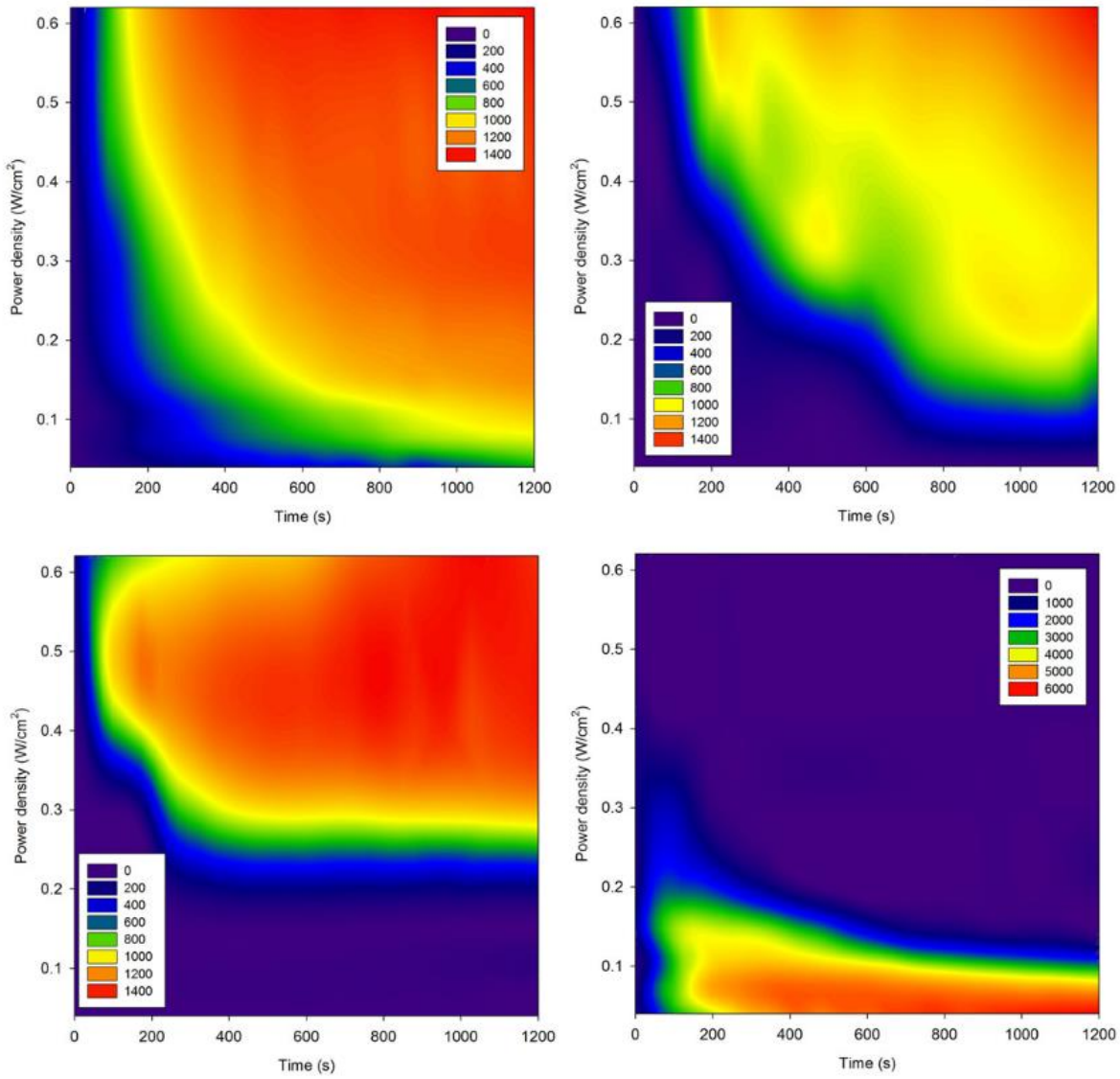

Figure 2.2: A plot showing the evolution of densities in a sealed SBD reactor as a function of discharge power density and time. Species shown are N_2O (top left), NO (top right), NO_2 (bottom left), and O_3 (bottom right). All figures show the density in ppm and were measured using FTIR. The figure is taken from [97].

The previous study identified two chemical modes of operation in SBDs, namely the ROS mode, where O_3 is the dominant species, and the RNS mode, where the dominant species is NO_2. It was reported that at power densities lower than 0.02 $W \cdot m^{-2}$, the discharge operates in ROS mode. For higher power densities, the discharge starts in ROS mode, then gradually transitions to the RNS mode, which is marked by the disappearance of O_3 from the discharge chamber and the

increase in NO_2 density. This transition became known as ozone quenching. Its exact mechanics are not fully understood.

To identify the mechanism behind ozone quenching, Bansemer et. al. documented the mode transition as either temperature or pressure were changed [98]. They reported that temperature has a major effect as it controls the rates of chemical reactions involved. They also found that the power of the discharge did not influence this transition. Furthermore, they determined that known reactions underestimate the generation of NO and proposed an effective rate coefficient to account for the underestimated NO necessary to capture the transition.

Numerous other studies have documented the chemical makeup of surface barrier discharges and their dependence on applied voltage, ambient conditions and electrode geometry. The humidity of the background gas has been shown to induce higher conductivity and increase the pulse amplitude required for the ignition of the discharge [99, 100]. Mericam-Bourdet et. al. [101] showed that the applied voltage waveform shape does not influence the ozone production rate, but that increasing its amplitude does increase ozone production, due to the extra energy put into the system. The use of UV spectroscopic techniques is less common as they can only measure a few species such as OH and O_3, in comparison to FTIR which can measure a wide range of species. For example, Nupangatha et. al. used UV absorption to measure the density of OH in SBDs to be of the order of 10^{19} m^{-3} [102]. A thorough review of the chemical processes involved in barrier discharges can be found in [103].

It should be noted at the end of this subsection that spectroscopic techniques provide limited information on the spatial distribution of the reactive species. In that sense, most of the densities given in the context of spectroscopic studies are spatially averaged. Obtaining information on the spatial distribution of species requires laser diagnostic techniques.

2.2.3 *Laser-Induced Fluorescence (LIF)*

Laser-Induced Fluorescence (LIF) is a technique that allows for quantifications of species in a volume, where the distribution of the species can be obtained as a 2D map in the region of the measurement. It works by shining a very short laser pulse with a chosen wavelength on a region of species to induce a specific excitation state of the species to be measured. Then by measuring the emission intensity of photons resulting from the radiative decay of the excited state, it is possible to convert the measured intensity to a density of the species to be measured [14]. Thus, providing a 2-dimensional map of species density at a given time.

This technique has been used to measure different species in SBDs, for example, it was used to measure NO in a single discharge gap [104], where it was reported that the density of NO in SBDs is in the range of 100 – 200 ppm at up to 10 mm downstream. Vorac et. al. used LIF to measure the density of OH emerging from an SBD near water operating in argon gas [105], where they reported the density to be of the order of 10^{21} m^{-3}. Ambrico et. al. used LIF to measure metastable nitrogen N2(A) in SBDs operating in nitrogen gas [106]. They reported the density to be in the order of 10^{17} m^{-3} 1 mm downstream from the surface, while in the discharge gap it is in the order of 10^{18} m^{-3}. Teramoto et. al. measured the density of OH over an SBD operating in air at atmospheric pressure [107], where they reported that the density of OH was highest in the streamer channels, where it was of the order of 10^{21} m^{-3}. Li et. al. measured OH over an SBD operating in helium or argon gas mixed with water admixture [108], where they reported densities of the order of 10^{21} m^{-3} for argon case in comparison to 10^{19} m^{-3} for helium case under similar conditions.

As is clear from the previous discussion, works using LIF seem to focus on either NO or OH. The reason is that LIF requires the radiative decays transition to have a lifetime long enough to be captured by an ICCD camera to be analysed. This condition severely limits the species which can be measured using this technique.

2.2.4 *Flow measurements*

For applications where SBDs are used as flow actuators, analysing the resultant flow is of paramount interest. Techniques for studying the induced flow experimentally include Schlieren imaging and Particle-Image Velocimetry (PIV) [109]. In Schlieren imaging, the flow creates density gradients which in turn cause variation in the refractive index of air, thus leading to distortion in an incident collimated beam. The setup for this technique is relatively simple and provides flow visualisation but provides no quantitative information on the velocity field. For example, Cristofolini et. al. used Schlieren imaging to analyse the evolution of the flow upon the ignition of the plasma [110], where they reported a relationship between the flow velocity distribution in the boundary layer and the gas density distribution. Neretti et. al. use Schlieren imaging to demonstrate the use of a vectorised SBD to control the direction of the resultant jet flow [111]. Gao et. al. combined Schlieren imaging with Pitot tubes to measure the flow velocity induced by an SBD [112]; they reported the existence of an optimal electrode gap that corresponds to a maximum induced flow velocity.

A superior technique in this context is PIV, as it shows the structure of the flow field in addition to the amplitude of the flow velocity. In PIV, the gas is nebulised with a tracing element, such as micro droplets of drop oil. When PIV measurement is in operation, two laser sheets are shined on the discharge with controllable time delay. The scattered light from the tracing element is recorded by a high-speed camera. The images are then processed with image processing software which identifies how much every tracing element moved between the times the two laser sheets were shined. By dividing the displacement by the time delay, an estimate of the velocity of the droplets can be obtained, which closely follows the velocity of the background gas. Thus, providing a 2D map of the velocity field.

Do et. al. were one of the first groups to use PIV to analyse the flow induced by SBDs [113], where they compared the alternation of an external flow between an AC-driven SBD and a pulsed-driven SBD. They reported that AC-driven discharges showed greater alteration of the background flow than pulsed-driven discharges. Moreau et. al. used PIV to analyse the

difference in the resultant flow between the standard 2-electrode SBD configuration and a 3-electrode configuration [114], where the third electrode is driven by a DC signal. Larger airflow alteration is induced by the 3-electrode configuration, where the two AC electrodes serve as ionisers while the third DC electrode served as a control electrode for the EHD-induced flow. Zito et. al. focused on scaling down SBDs to micron size and investigated the resultant induced flow [115]. They showed that the micro-discharge had a 31% greater energy conversion efficiency than the macro-sized discharge. Dickenson et. al. used PIV to develop a method to steer the flow by applying a phase shift to the voltage waveforms driving the SBDs [116]. Xie et. al. investigated the effect of rise time on induced flow in pulsed SBDs using PIV [117]. They reported that short rise times lead to higher energy deposition in the discharge and a stronger tangential acceleration ability. Sato et. al. did an extensive analysis of surface charging in SBDs and how the surface charge profile affects the induced flow [118], deriving a relation between the EHD forces and the potential profile over the dielectric surface. They reported that surface charge relaxation on the dielectric surface takes hundreds of milliseconds for frequency of operation in the kHz regime. Comprehensive reviews on the use of SBDS in combination with PIV can be found in [119, 120].

2.2.5 *Temperature and heat transfer in SBDs*

Few studies have focused on heating in SBDs. For example, Nudnova et. al. [23] reported that in an atmospheric pressure air system operating under 1000 Td, up to 54% of the discharge power goes into heating, the temperature distribution in an SBD was characterized using Infrared Thermography (IRT) measurements. In the work of Tirumula and colleagues [24] it was suggested that heat transfer to the downstream region is predominately through convection, but that the near electrode region may be heated by ion bombardment. Using the same technique, it was reported that surface temperature increases linearly with frequency and quadratically with voltage amplitude in an SBD [121]. IRT was also used to experimentally identify a positive correlation between the applied voltage and the dielectric surface

temperature. This showed that different dielectric materials produce different thermal responses [121], which can either be due to different dielectric heating properties or different plasma properties. It has also been reported using IRT that a hotter dielectric surface produced higher flow velocities but also consumed more power [90].

2.2.6 *SBD array diagnostics*

Experimental studies of SBD arrays have focused on multiple aspects such as the induced flow, the impact on selected RONS and the plasma's behaviour in the discharge gaps. For example, Wang *et. al.* [122] studied the impact of the electrode's shape when using an array of SBDs on the induced flow. They reported that complex shapes such as triangles, serpentine shapes and square electrodes produced stronger mixing downstream in comparison to linear arrays. Moreau *et. al.* [27] experimentally reported that the addition of a DC-biased electrode to the standard SBD configuration for flow actuators increased the maximum velocity by up to 150% and the flow rate by up to 100%. Takaki *et. al.* [123] studied the impact of electrode geometry on the efficiency of NO_x removal from diesel engine exhaust. They compared plane, trench and multipoint-pyramid electrode geometries and reported that multipoint-pyramid shaped electrodes performed notably better in removing NO_x from the flowing gas for a constant input power.

2.3 Numerical simulations of SBDs

Despite the large range of experimental techniques utilised to probe SBDs dynamics, a major factor hindering our understanding of how they work is that not all temporal and spatial scales are experimentally accessible. For example, PIV in its standard configuration cannot detect motion on micrometre scale or time scales below milliseconds. LIF is only applicable for a few species that have long enough metastable state lifetimes and can only be used in configurations where enough space exists between the laser and any scattering surface (an electrode for example). FTIR has no spatial resolution and is limited timewise to the seconds timescale. Hence, experimentally validated numerical modelling provides insight into dynamics that

cannot be captured easily in experimental techniques, thus 'filling the gaps' in experimental findings.

Considering that at atmospheric pressure 1 m^3 volume of gas contains over 10^{25} molecules, accounting for kinetic effects using particle-based methods such as PIC is not feasible even when using 'super-particles' [13]. Consequently, the vast majority of SBD modelling is done by considering the discharge as a fluid [14]. This approach is accurate at atmospheric pressure considering the high collision frequency with the background gas. However, even with this simplification, large difficulties remain. The equations of the fluid model are non-linear, making computation more resource consuming and more prone to numerical instabilities. Furthermore, important aspects of plasma dynamics happen on a wide range of spatial and temporal scales. A plasma streamer's head is just 50 μm wide and the resolution of its dynamics requires timesteps of 10^{-12} seconds or less [15]. Meanwhile, ozone quenching discussed in subsection 2.2.2 occurs in tens of seconds. Bridging this difference in timescales is another aspect of uncertainty in numerical models.

The earliest numerical models of SBDs date back to the 90s [124]. Since then, with the increase of computer power at cheaper prices, the number of numerical models has grown significantly. In general models of SBDs can be categorised based on their dimensionality into 0D (global), 1D and 2D models. Every category is reviewed in the next subsections.

2.3.1 *Zero-dimensional models (global models)*

Global models are considered to be the simplest computational models, where the discharge volume is treated as a single volume over which all species densities are uniform. While Such models lose information on spatial dependence, they have the advantage of running over very long times. For example, Sakiyama developed a comprehensive 0D model for humid air plasma [125]. The model can solve up to 100 seconds and is applicable for power densities below the ozone quenching threshold. They reported that the dominant long-lived species in the afterglow volume of the discharge were O_3, N_2O_5, N_2O, HNO_3, H_2, NO_3, H_2O_2, HNO_2 and NO_2. In a follow-up work, Sakiyama et. al. reported that long-lived species can be decoupled from other species

when solving the equations with minimal impact on the results [126], providing a valuable tip for efficient modelling of such multiscale discharges. The reaction set developed by Sakiyama was later extended by Shimizu et. al. [127], to include reactions involving excited nitrogen and their conversion into NO, allowing ozone quenching process to be captured in the model. Yi et. al. extended Sakilyama's model to include gas heating effects [128]. they reported that ohmic heating in the discharge layer considerably affects the rate constants of the temperature-dependent chemical reactions. Bansemer et. al. developed a simplified chemical model which contains only reactions with the highest reaction rates from Sakiyama's model to describe SBDs behaviour at different temperatures and pressures [129]. They reported that the chemical route of metastable nitrogen is vital for the production of NO, which leads to ozone quenching, as is reported experimentally.

2.3.2 *One-dimensional models*

1D models provide a further realistic step from 0D models. As they capture part of the spatial dependence with a manageable increase in computational resources. In the vast majority of 1D models, the spatial dimension is taken to be perpendicular to the dielectric surface, as that is the direction where species get transported by the EHD-induced flow. For example, Liu et. al. adopted Sakiyama's model and converted it into a 1D version and added a liquid layer downstream from the SBD [130]. They reported that species with the highest concentrations in the liquid phase of aqueous HO_{2aq}, HO_{3aq}, OH_{aq} and O^{-}_{2aq} as well as NO_{2aq} and NO_{3aq} are all generated locally at the interface between the afterglow region and the liquid. Further work by Liu et. al. using the same model [131], showed that changing the gap between the plasma and the liquid interface has a profound impact on the produced liquid phase chemistry, identifying the critical limit of 0.5 cm as the transition point. Hasan et. al, developed a 1D model of Sakiyama's set [132]. They showed that non-long-lived species can be further split into short-lived and intermediate-lived species when the spatial distribution is taken into consideration. While short-lived species such as ions are generated and consumed in every pulse, intermediate-lived species such as NO experience accumulation of the density over consecutive

pulses, while long-lived species such as O_3 barely change over consecutive pulses. In a follow-up work, Hasan et. al. used their 1D model to investigate the effect of high gas flow rates on the induced chemistry of an SBD [133]. They reported that having a high flow rate (flow velocity greater than 2 $m \cdot s^{-1}$) increased the lifetime of unstable reactive species such as OH at the expense of more stable reactive species such as NO_2. Other 1D models of SBDs assumed the resolved spatial dimension is parallel to the dielectric surface instead of perpendicular as in the previous studies. For example, Akishev et. al. developed a 1D model describing streamer evolution as a nonlinear diffusion process in order to reduce the computational costs of modelling SBDs [134]. Considering that the main reason for modelling the direction parallel to the dielectric is computing EHD forces, most works done on that topic were 2D models.

2.3.3 *Two-dimensional models*

The vast majority of 2D models of SBD focused on analysing the EHD forces and the consequences to the induced flow. For example, Solovev et. al. implemented a 2D numerical model to analyse the effect of the polarity of the driving voltage of an SBD discharge [135]. They reported that the discharge zone above the dielectric surface is five times thicker for positive polarity in comparison to negative polarity. Enloe et. al. who studied the impact of geometrical effects on the induced thrust in SBDs [136]. They reported that the thrust produced by the discharge depends directly on the thickness of the exposed electrode even when the bulk discharge properties of the plasma remain unchanged. Boeuf et. al. investigated the contributions of positive and negative ions to the EHD force in a typical SBD [137]. They reported that positive ions exert the EHD force during the positive half of the waveform cycle and negative ions exert the EHD force during the negative half of the cycle. They also reported that negative ions tend to contribute more to the EHD forces at low frequencies and high voltage amplitudes. Jayaraman et. al. further investigated the dynamics of SBD discharges and how it affects the EHD forces using a 2D model [138]. Based on their results they proposed that introducing asymmetry in the applied waveform can increase the EHD force generated and thus the induced flow. Starikovskii et. al. investigated the heat generated in pulsed-operated SBDs

and how it influences the induced flow [139]. They reported that for high amplitude voltages, in the order of tens of kVs, a temperature increase of 400 K can induce a shockwave that brings the induced flow velocity to almost zero. Zhu et. al. developed a 2D model for SBDs and conducted parametric studies investigating the effect of different dielectric permittivity and dielectric thickness on the flow [140]. For applied potentials in the order of 20 kV, they reported that the maximum induced velocity is obtained for the lowest dielectric permittivity and that a reduction in the thickness of the dielectric causes an increase in the induced velocity. Kourtzanidis et. al. implemented a 2D model for SBDs [141]. They reported that the plasma channel generated in the positive cycle serves as both a positive and negative charge generator and acts as a virtual anode. They also reported that most surface charging of the dielectric occurs after the plasma channel reached its peak length.

Most recent research on SBDs focuses on their performance as sources of reactive species. However, 2D models taking chemistry into account remain scarce. Examples of 2D models for SBD chemistry include the work of Y Zhu [142], who implemented a 2D model of an SBD taking into account only charged and short-lived excited neutral species. Their model was solved for 30 ns and was focused on analysing the ion fractions and how they contribute to emission spectra from the discharge. Dickenson et. al. developed an SBD model which they used to evaluate the influence of altering the flow on the delivery of a reactive species (O_3 for example) to a downstream position [116]. They reported that altering the direction of the flow by applying phase shifts to the electrodes has no impact on the magnitude of the flux of reactive species, demonstrating independent control of the flow and the chemistry of the discharge. In a subsequent work, the same group developed the 2D model to run over a seconds timescale [104], including all species included in Sakiyama's model. They used the model to analyse the chemical pathways and behaviour of reactive nitrogen species in SBDs, where they reported that NO is generated in the discharge gap while NO_2 is generated as it is transported by the induced gas flow downstream.

2.3.4 *Other types of models*

The previous sections provided a systematic review of previous numerical modelling work done on SBDs, while most works fall under those categories, a few works had different approaches. For example, Nishida et. al. implemented a 3D SBD model to investigate the influence of the non-uniformity of the EHD force in SBD [143]. Their model showed that a significant component of EHD forces exists in the third dimension which is usually ignored in 2D models. Figure 2.3 shows an example of streamers captured using their model.

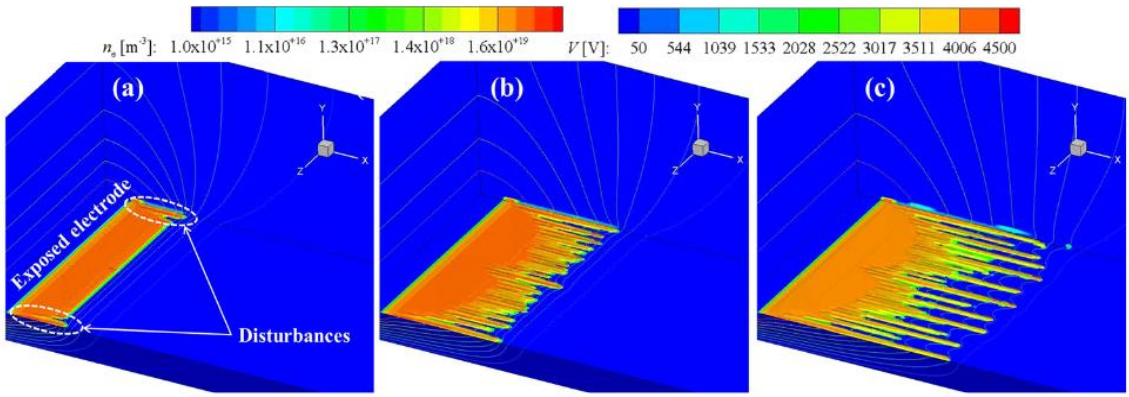

Figure 2.3: A plot showing the evolution of the plasma potential and electron density as a function of time in a 3D model of SBD. The figure is taken from [143].

All the models discussed in this chapter so far were fluid models. Babaeva et. al. implemented a hybrid SBD model [144], where ions and cold electrons are treated as fluids while secondary emitted electrons are treated using Monte Carlo (MC) algorithms. They reported thermalisation modelling using MC methods was equivalent to standard fluid modelling and that standard fluid modelling is adequate. While all previously discussed models assumed laminar flow is induced by the plasma, Gaitonde et. al. used a semi-empirical model to study the flow induced by pulsed SBDs using Large Eddy Simulations (LES) [145]. They reported that the heat shockwave induced by the discharge can be captured correctly from a fluid dynamics perspective by assuming a volumetric heat deposition in the plasma.

2.3.5 *Models of SBD arrays*

Considering that the dynamics of SBDs occur on temporal and spatial scales difficult to observe with widely-used experimental techniques, numerical models can provide considerable additional insight into their operation. Zhang *et. al.* [146] implemented a 2D fluid model to investigate streamer evolution in SBD arrays. They reported that streamer length and discharge uniformity are dependent on electrode spacing, where there is an optimal electrode spacing that produces the most uniform discharge. Wang *et. al.* [147] studied a micro-DBD array using a 2D fluid model with a Monte-Carlo simulation to follow secondary electron production. They reported that the interaction of three adjacent discharges causes bending of the outer discharge plumes away from the central discharge due to the remaining charge density from previous pulses. It was shown that electron density and surface potential depended strongly on discharge spacing, but no matter how closely spaced the discharges were, the plumes never completely merged. Kourtzanidis *et. al.* [141] implemented a numerical model to examine the influence of adding a third electrode to the standard two-electrode configuration of SBDs for flow control actuators. They reported that under certain bias conditions the streamers in the gap can merge forming a large area of plasma that covers the entire inter-electrode space, thus increasing the effective energy release region.

2.4 Summary

Based on the previous review, it is possible to identify the main gaps in the literature in the field of SBDs. The main noticeable gap is the limited number of studies where the behaviour of species downstream from an SBD is analysed in depth. Specifically, since SBDs were shown to get hot during operation, how does that affect the species generated? Another question is: when adjusting the geometry of the SBD, particularly when setup in an array, how is the downstream chemistry affected? Both questions are crucial when producing any industrial process based on SBDs. Answering these questions will be the focus of this thesis.

3. Numerical model

This chapter reviews the numerical model used to obtain the results discussed in the subsequent chapters. A baseline model existed prior to commencing this work. The baseline mode was the starting point of this work, where it was modified to account for the effects studied in this thesis. All models presented here were implemented using the COMSOL multi-physics software package [148].

3.1 Baseline model

The baseline model was reported for the first time in [104]. It describes a 2D reactive flow generated in a single SBD discharge gap. It consists of three sub-models, which will be referred to as modules for the rest of this work. Every module describes one aspect of the physics or chemistry of the discharge on specific spatial and temporal scales. The modules are the plasma module, the chemical module, and the reactive flow module.

3.1.1 *The plasma module*

The plasma module is a time-dependent multi-fluid model following the evolution of 6 species which are: e^-, O_2, O_2^+, O_2^-, N_2, N_2^+, in addition to the electron mean energy and the electric potential. Those 6 species were chosen as they represent each category of species (electrons, positive ions and negative ions) and are the dominant species typically encountered in SBDs [132]. Mathematically, for every species followed by the plasma module, the continuity equation is solved as given by equation 3.1.

$$\frac{\partial n_k}{\partial t} + \nabla \cdot \left(-\mu_k n_k \vec{E} - D_k \nabla n_k\right) = R_k \qquad (3.1)$$

In equation (3.1), n_k represents the density of the k^{th} species (m^{-3}), t is time (s) and μ_k is the mobility ($m^2 \cdot V^{-1} \cdot s^{-1}$) of the k^{th} species. The mobility of neutral species was set to 0, for electrons it was computed using BOLSIG+ [149] and tabulated as a function of the electron mean energy. BOLSIG+ is an open-source Boltzmann equation solver programme. It is designed for weakly ionised gases, taking the Electron Energy Distribution Function (EEDF) and cross-section data

as inputs and returning transport coefficients including the electron mobility and various collision rates. The EEDF may be non-Maxwellian but the system must be spatially uniform. Only electron-neutral collisions are considered. The system is reduced to a convection-diffusion problem and solved through numerical matrix inversion techniques.

For ions it is computed using Einstein's relation from the diffusion coefficient [4], which appeared as D_k in equation 3.1, representing the diffusion coefficient of the k^{th} species ($m^2 \cdot s^{-1}$). Diffusion coefficients of all species, excluding electrons, are listed in table 3.1. The diffusion coefficient of electrons is computed using BOLSIG+. $\vec{E}$ is the electric field ($V \cdot m^{-1}$) and lastly R_k is the rate expression of the k^{th} species ($m^{-3} \cdot s^{-1}$), which is given by equation 3.2.

$$R_k = k_a n_A n_B - k_b n_k n_c + \cdots \tag{3.2}$$

Species	Diffusion coefficient ($m^2 \cdot s^{-1}$)
N_2	2.1×10^{-5}
O_2	2.1×10^{-5}
N_2^+	5.9×10^{-5}
O_2^+	5.6×10^{-5}
O_2^-	5.6×10^{-5}

Table 3.1: Diffusion coefficients used in the baseline model [125].

In equation 3.2, k_a and k_b represent rate coefficients of reactions A and B explained by equations 3.3 and 3.4, n_A, n_B, and n_C are the densities of species A, B and C respectively. Equation 3.2 will have one term per reaction in which the k^{th} species is involved. If it is a gain reaction for the k^{th} species, it will have a positive sign. If it is a loss reaction for the k^{th} species, it will have a negative sign. A total of 13 elementary reactions are included in the plasma modules, which are listed in table 3.2.

$$A + B \rightarrow K \tag{3.3}$$

$$K + C \rightarrow D \tag{3.4}$$

As mentioned earlier, the plasma module also solves for the electron energy density as given by equation 3.5.

$$\frac{\partial n_\varepsilon}{\partial t} + \nabla \cdot \left(-\mu_\varepsilon n_\varepsilon \vec{E} - D_\varepsilon \nabla n_\varepsilon\right) = S_e - \vec{E} \cdot \vec{\Gamma_e} \quad (3.5)$$

In equation 3.5, n_ε is the electron energy density (eV·m^{-3}), S_e is the electron collisional energy loss (eV·m^{-3}·s^{-1}); $\vec{\Gamma_e}$ is the electron flux (m^{-2}·s^{-1}), μ_ε is the electron mobility (m^2·V^{-1}·s^{-1}) and D_ε is the electron energy density diffusion coefficient (m^2·s^{-1}), with the last two both obtained from BOLSIG+ [149]. The electron collisional energy loss can be further expanded as shown in equation 3.6.

Rxn No.	Reaction formula	Reaction coefficient	Energy cost (eV)
R1	$e + N_2 \rightarrow e + N_2$	$f(e_{avg})^b$	$0.3(T_e\text{-}T_g)$
R2	$e + O_2 \rightarrow e + O_2$	$f(e_{avg})^b$	$0.26(T_e\text{-}T_g)$
R3	$e + N_2 \rightarrow 2e + N_2^+$	$1\times10^{-16}\, e_{avg}^{\ 1.9} \exp(-14.6/ e_{avg})$	15.58
R4	$e + O_2 \rightarrow 2e + O_2^+$	$9.54\times10^{-12}\, e_{avg}^{\ -1.05} \exp(-55.6/ e_{avg})$	12.07
R5	$e + O_2 \rightarrow O_2^-$	$9.72\times10^{-15}\, e_{ve}^{\ -1.62} \exp(-14.2/ e_{avg})$ $e_{avg} > 1.13$ $2.78\times10^{-20}\, e_{avg} < 1.13$	
R6	$e + N_2 + O_2 \rightarrow N_2 + O_2^-$	$1.1\times10^{-43} (T_g/T_e)^2 \exp(-70/T_g) \exp(1500(T_e\text{-}T_g)/(T_eT_g))$	
R7	$e + 2O_2 \rightarrow O_2 + O_2^-$	$1.4\times10^{-41} (T_g/T_e) \exp(-600/ T_g) \exp(700(T_e\text{-}T_g)/(T_eT_g))$	
R8	$M + e + N_2^+ \rightarrow M + N_2$	$3.12\times10^{-35}/T_e$	
R9	$N_2 + O_2^- \rightarrow e + O_2 + N_2$	$1.9\times10^{-18}(T_g/300)^{0.5} \exp(-4990/ T_g)$	
R10	$O_2 + O_2^- \rightarrow e + O_2 + O_2$	$2.7\times10^{-16}(T_g/300)^{0.5} \exp(-5590/ T_g)$	
R11	$O_2 + N_2^+ \rightarrow O_2^+ + N_2$	5×10^{-17}	
R12	$O_2^- + N_2^+ \rightarrow O_2 + N_2$	$2\times10^{-13}(300/T_g)^{0.5}$	
R13	$O_2^- + O_2^+ \rightarrow 2O_2$	$2\times10^{-13}(300/T_g)^{0.5}$	

Table 3.2: A list of reactions included in the plasma module. All reaction coefficients were taken from [125], e_{avg} is the mean electron energy (eV), calculated by dividing the electron energy density by the electron density, T_g is the gas temperature (K), and T_e is the electron temperature (eV), defined as $2e_{avg}/3$.

$$S_e = S_{e,elastic} + S_{e,inelastic} = \sum_j \epsilon_j k_j n_e n_{N_2} + \sum_k \epsilon_k k_k n_e n_{O_2} \quad (3.6)$$

In equation 3.6, the electron collisional energy loss is split into its elastic component and its inelastic component. The nature of these terms is indistinguishable as the right-hand side of equation 3.6 shows. The main difference between them is that elastic loss terms are represented by reactions R1 and R2 in table 3.2, where ϵ is the energy cost associated with the reaction (eV) as given in table 3.2. For inelastic losses, ϵ represents the sum of all energy losses due to rotational and vibrational excitations of N_2 and O_2 molecules respectively, which were obtained from the LXCat database [150].

The plasma module also solves for the electric potential, computed by the Poisson equation as equation 3.7 shows.

$$\nabla^2 V = \frac{q_e}{\varepsilon_r \varepsilon_0}\left(n_{N_2}^+ + n_{O_2}^+ - n_{O_2}^- - n_e\right) \quad (3.7)$$

In equation 3.7, V is the electric potential (V), which is used to determine the electric field using $\vec{E} = -\nabla V$, ε_r is the relative permittivity of the media, which was set to 1 for air and 9.8 for the dielectric, which was alumina for most experiments, ε_r is the free space permittivity (F·m^{-1}), and q_e is the elementary charge (C).

To model the accumulation of the surface charge on the dielectric surface. An ordinary differential equation is solved on the dielectric surface to follow the evolution of the surface charge density as given by equation 3.8.

$$\frac{\partial \rho_s}{\partial t} = q_e \hat{n} \cdot \left((1+\gamma_{N_2^+})\overrightarrow{\Gamma_{N_2^+}} + (1+\gamma_{O_2^+})\overrightarrow{\Gamma_{O_2^+}} + \overrightarrow{\Gamma_{O_2^-}} + \overrightarrow{\Gamma_e}\right) \quad (3.8)$$

Where $\hat{n}$ is the normal vector to the dielectric surface, Γ represents the flux of the denoted species, and γ_i is the electron secondary emission coefficients of the i^{th} species. This calculation assumes that the charges of all particles incident to the surface are +/-1 and that all species arriving to the surface are neutralised rather than reflected. The fluxes are computed in equation 3.1.

The computational domain for the plasma module is shown in figure 3.1. For every partial differential equation listed earlier, a boundary condition is needed in order to solve the equation. A list of boundary conditions implemented in the plasma module is given in table 3.3. The numbers assigned to the boundaries are indicated in figure 3.1.

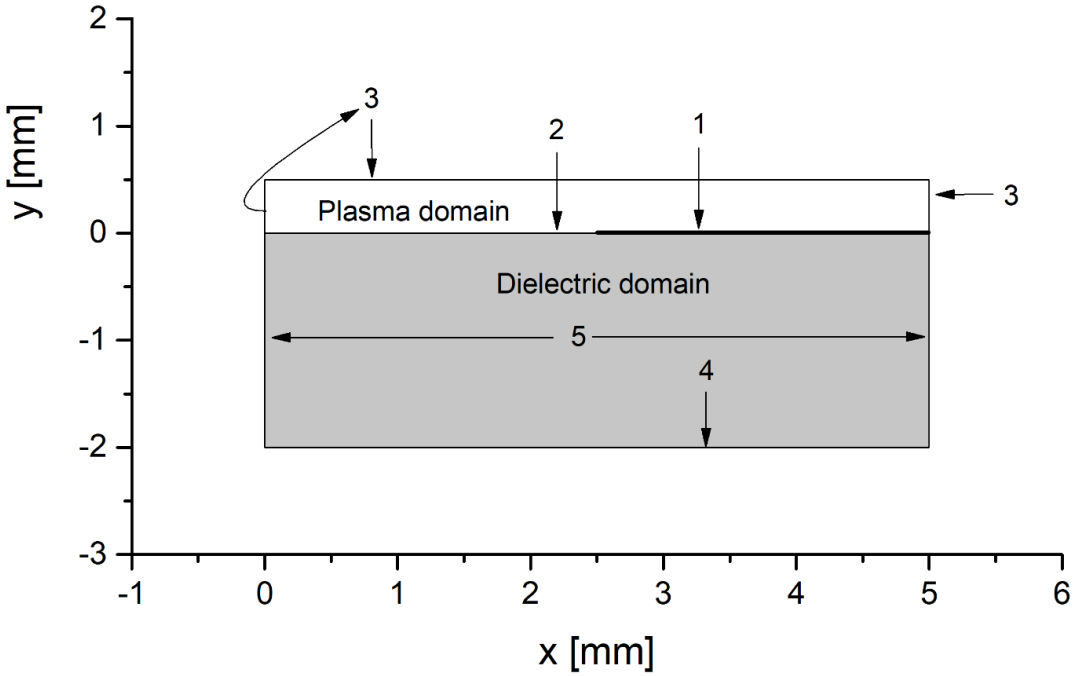

Figure 3.1: The computational domain used in the plasma module. The electrode is shown by the thick black line. The numbers are used to explain the boundary conditions given in table 3.3.

Boundary	Electric potential	Continuity equations
1	$V = V_{applied}$	$\hat{n} \cdot \vec{\Gamma}_i = \frac{1}{4} n_i v_{th,i} - \mu_i n_i \nabla V (-\nabla V \cdot \hat{n} > 0)$
2	$-\varepsilon \nabla V = \rho_s$	$\hat{n} \cdot \vec{\Gamma}_i = \frac{1}{4} n_i v_{th,i} - \mu_i n_i \nabla V (-\nabla V \cdot \hat{n} > 0)$
3	$-\hat{n} \cdot \nabla V = 0$	$\hat{n} \cdot \vec{\Gamma}_i = 0$
4	$V = 0$	N/A
5	$-\hat{n} \cdot \nabla V = 0$	N/A

Table 3.3: Boundary conditions used in the plasma module. A boundary equation is imposed per species included in the module, $V_{applied}$ is the applied voltage waveform, $n_{th,i}$ is the thermal speed of the *ith* species. The condition in parenthesis for the continuity equation on boundaries 1 and 2 is non-zero only if the flux driven by the electric field is directed outward from the plane of the computational domain.

Boundary 1 represents the driven electrode. Boundary 2 represents the interface between the plasma and the dielectric, where the flux of the charged species creates a surface charge. Boundaries 3 and 5 represent symmetry boundaries implying that the outer side of the boundary is a mirrored version of the domain, and boundary 4 represents the grounded electrode.

The input to the plasma module is the applied voltage waveform, in addition to the geometric parameters of the discharge such as the discharge gap width and the dielectric thickness. While the plasma module is solved, two auxiliary variables are evaluated at each time step and integrated in time. These are the instantaneous EHD forces, given by equation 3.9, in addition to the electron energy density, which is used to compute an extrapolation parameter *S*. Both variables are then divided by the period of the waveform to obtain the time-averaged quantities. The time-averaged EHD force is used as input to the reactive flow module, which is described in section 3.1.3, while the extrapolation parameter S is used as input to the chemistry module, discussed in section 3.1.2.

$$F_{EHD} = q_e\left(n_{N_2}^{+} + n_{O_2}^{+} - n_{O_2}^{-} - n_e\right)\vec{E} \tag{3.9}$$

3.1.2 *The chemistry module*

In principle, the plasma module can be extended to account for a larger set of reactive species and a more comprehensive chemical reaction set. However, every species added adds a degree of freedom to every node in the domain, meaning the computational cost of the plasma module grows rapidly. Moreover, considering that many of the species generated in SBDS are long-lived species, which evolve over seconds of operation, capturing the dynamics of these species using the plasma module is both impractical and unnecessary. Therefore, the domain of validity for the plasma module is restricted to tens of microseconds in time and a few millimetres in space.

To overcome the computational limitations of the plasma module, the chemistry module is defined. It is a hybrid 0D-2D model, the 0D component consists of a system of coupled ordinary differential equations, which are solved for the densities of 52 species, listed in table 3.4, and 625 reactions associated with them. For every species, the continuity equation is solved as given in equation 3.10.

$$\frac{\partial n_i}{\partial t} = R_i - \frac{n_i\vec{u}}{d} \tag{3.10}$$

In equation 3.10, n_i is the density of the *ith* species (m^{-3}), R_i is the rate expression of the *ith* species, which is similar to that described in equation 3.2, $\vec{u}$ is the velocity field at the point where the chemistry module is evaluated ($m \cdot s^{-1}$), which is calculated from the reactive flow module, and d is a characteristic length of the area where the reactions take place (m).

Species type	Species list	Classification
Positively Charged	N^+, N_2^+, N_3^+, N_4^+, O^+, O_2^+, O_4^+, H^+, H_2^+, H_3^+, OH^+, H_2O^+, H_3O^+, NO^+, N_2O^+, NO_2^+	Short-lived
Negatively Charged	e, O^-, O_2^-, O_3^-, O_4^-, NO^-, N_2O^-, NO_2^-, NO_3^-, H^-, OH^-	Short-lived
Excited	$N(^2D)$, $N_2(A^3\sum)$, $N_2(B^3\Pi)$, $O(^1D)$, $O_2(a^1\Delta)$	Short-lived except $O_2(a^1\Delta)$ which is long-lived
Neutral	H, N, O, NO, NO_2, NO_3, N_2O, N_2O_3, N_2O_4, N_2O_5, O_3, HNO, HNO_2, HNO_3, OH, H_2O_2, HO_2, H_2, N_2, O_2, H_2O	Long-lived except for H which is short-lived

Table 3.4: Species included in the chemistry module.

In table 3.4, the species are categorised based on their decay times into both short-lived species, which are created and consumed within every period of the waveform and long-lived species, which accumulate over multiple periods. This categorisation has been used in many previous works [125, 132].

Considering that electrons drive the chemistry of the discharge; electron impact reactions must be accounted for. This is done by using the extrapolation parameter *S,* as computed by the plasma module. A typical plot of the extrapolation parameter is shown in figure 3.2. By definition, S = 1 at the point where the time-averaged electron energy density is highest, which was shown to be the region where most of the species generated by electron-impact reactions are created. The characteristic length of this region is used as the characteristic length (d) parameter in equation 3.10. The use of the extrapolation parameter allows the chemistry module to account for some spatial effects such as convection, therefore the module was defined as a 0D-2D hybrid.

In addition to species densities, the chemistry module also solves for the electron temperature, given by equation 3.11.

$$\frac{\partial}{\partial t}\left(\frac{3}{2}n_e T_e\right) = P_{dep} - S_{en} \tag{3.11}$$

In equation 3.11, P_{dep} is the power deposition obtained from the plasma module at the centre of the shaded region in figure 3.2, and S_{en} is the collisional energy loss computed by the chemistry module.

The chemistry module is solved for 10 periods of the applied waveform, which is enough for the short-lived species to display periodic behaviour. In the last period, all the chemical reactions leading to the generation of long-lived species, such as N_2O, from short-lived species are grouped and averaged over the waveform period. This produces an effective generation term g_{N_2O}, which represents the generation rate of N_2O from short-lived species. The same procedure is followed where N_2O is consumed in reactions involving short-lived species, giving an effective loss term l_{N2O}, which represents the loss rate of N_2O from reactions with short-lived species. Considering that loss reactions of N_2O include it as a reactant, the loss term l_{N_2O} is normalised by the density of N_2O. Two terms, g and l, are obtained for every long-lived species listed in table 3.4. These terms are then used as an input to the reactive flow module.

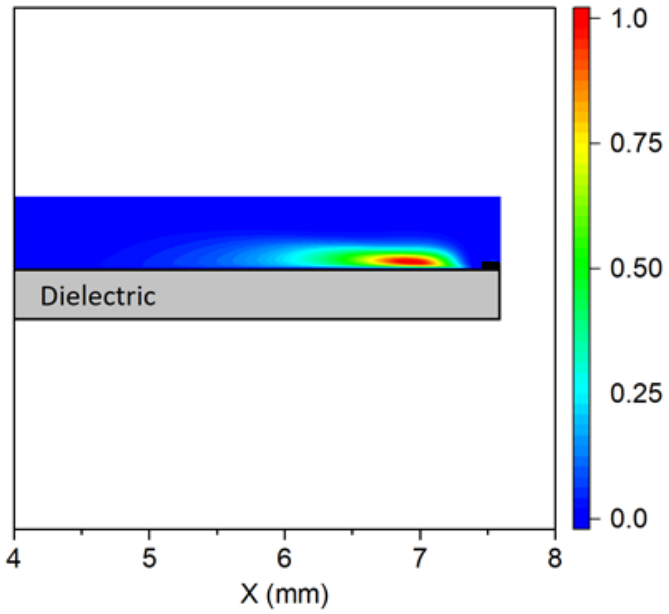

Figure 3.2: A typical plot of the extrapolation parameter S which represents the intensity of electron-impact reactions.

3.1.3 *The reactive flow module*

The reactive flow module predicts the behaviour of long-lived species downstream from the discharge. Its inputs are the EHD forces computed by the plasma module, in addition to the gain and loss terms for every species as computed by the chemistry module. The continuity equation, given by equation 3.12, is solved for all 21 long-lived species listed in table 3.4, as these species may live long enough to experience convection.

$$\frac{\partial n_i}{\partial t} + \nabla \cdot (-D_i \nabla n_i + n_i \vec{u}) = R_i + G_i - L_i n_i \tag{3.12}$$

In equation 3.12, n_i is the density of the *ith* species (m^{-3}); D_i is the diffusion coefficient of the *ith* species ($m^2 s^{-1}$), obtained from [125] and R_i is the rate expression of the *ith* species ($m^{-3} s^{-1}$), which is similar to that in equation 3.2. The term R_i accounts for reactions among the long-lived species only, while the effect of reactions involving short-lived species is implicitly included in equation 3.12 through the terms G_i and L_i, which describe the generation and loss rates of the *ith* species due to short-lived species. These two parameters are defined by equation 3.13.

$$G_i = g_i S \tag{3.13}$$

In equation 3.13, g_i is the effective generation rate calculated earlier. Since it is a scalar and needs to be converted to a 2D variable to be solved by equation 3.12, it is multiplied by the extrapolation parameter S, shown in figure 3.2. The same procedure is followed to obtain L_i from l_i, as well. It should be noted that the generation parameter G_i and the loss parameter L_i are defined in the plasma region only and are equal to zero elsewhere. The last term in equation 3.12 that was not defined until this point is the convection velocity u, which is computed by solving the Navier-Stokes equations. They consist of a continuity equation and a momentum conservation equation, both applied to the gas mixture, as given by equations 3.14 and 3.15.

$$\frac{\partial \rho}{\partial t} + \nabla(\rho \vec{u}) = 0 \tag{3.14}$$

$$\rho \frac{\partial \vec{u}}{\partial t} + \rho \vec{u} \cdot \nabla \vec{u} = -\nabla P + \varsigma \nabla^2 \vec{u} + F_{EHD} \tag{3.15}$$

Where ρ is the mixture's density (kg·m^{-3}), assumed to consist of 71% N_2, 20% O_2, and 1% H_2O, P is the pressure (Pa); ς is the viscosity of air (Pa·s) and F_{EHD} is the time-averaged electrohydrodynamic force (N·m^{-3}).

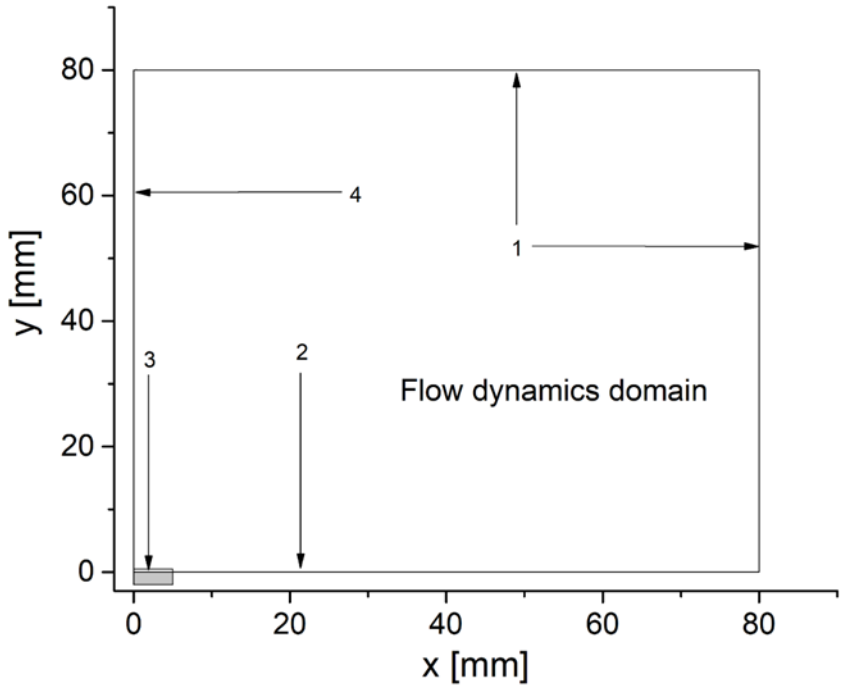

Figure 3.3: The computational domain used in the reactive flow module. The plasma region is above the grey rectangle shown in the corner of the plot. The numbers indicate the location of the boundary conditions given in table 3.5.

A typical computational domain of the reactive flow module is shown in figure 3.3. The boundary conditions used to solve the partial differential equations making this module are listed in table 3.5.

Boundary	Navier-Stokes equations	Convection-diffusion-reaction equations
1	$\hat{n} \cdot \bar{\bar{\tau}} = 0$ $\bar{\bar{\tau}} = -pI + \zeta(\nabla\vec{u} + \nabla\vec{u}^T) - \frac{2}{3}\zeta(\nabla \cdot \vec{u})I$	$-\hat{n} \cdot (D_i \nabla n_i) = 0$
2	$\vec{u} = 0$	$-\hat{n} \cdot (D_i \nabla n_i + n_i \vec{u}) = 0$
3	$\vec{u} = 0$	$-\hat{n} \cdot (D_i \nabla n_i + n_i \vec{u}) = 0$
4	$\hat{n} \cdot \vec{u} = 0$ $\bar{\bar{\tau}}_{tangent} = 0$	$-\hat{n} \cdot (D_i \nabla n_i + n_i \vec{u}) = 0$

Table 3.5: Boundary conditions used in the reactive flow module. A boundary equation is imposed per species included in the module. In table 3.5, $\bar{\bar{\tau}}$ is the viscous stress tensor (Pa), $\bar{\bar{\tau}}_{\text{tangent}}$ is the tangential component of the viscous stress tensor.

The boundary conditions on boundary 1 describe an open boundary, which implies that the other side of the boundary is a continuation of the domain and allows free flow into the surroundings. Boundary conditions on boundaries 2 and 3 describe walls, where the flow velocity is zero due to friction and the flux of the reactive species is zero. Boundary 4 describes a symmetry condition that is effectively equivalent to a wall as it prevents any transport of the species across the symmetry axis.

3.1.4 *Summary of assumptions of the baseline model*

Considering the complexity of the discharge dynamics, which extends from electron dynamics occurring on the nanosecond time scale to fluid dynamics occurring on the millisecond time scale, many simplifying assumptions needed to be made to facilitate solving the model. First, the model assumed that the evolution of the long-lived species chemistry does not influence the plasma dynamics. This assumption is translated into the model as the unidirectional coupling between the plasma module and the reactive flow module (no information is fed from the reactive flow module into the plasma module). As a result, the model is only valid for SBDs that operate in an open environment, where the flow of fresh air into the discharge region means the discharge has no memory of how long it has been operating. A second assumption was the gas

temperature. It was assumed in the baseline model that the operating temperature Is room temperature. Experimentally it is known that SBDs get hot when they operate for extended periods of time [151]. The consequence of this assumption is that the baseline model described up to the first 60 seconds of operation, minimising the effect of discharge heating. The impact of this assumption is explored further in chapter 5. Third, it was assumed in the formulation of the model that the flow induced by the plasma is laminar, and therefore no turbulence models were implemented. This assumption is well justified as the flow velocities typically induced by SBDs comparable to this work are in the range of a few $m \cdot s^{-1}$ [152]. Assuming the characteristic length of the flow is that of the discharge gap (approximately 1-10 mm), the Reynold number is in the range of 80-800, which is below the critical 2000 necessary for a transition into turbulence. The fourth assumption was using constant electron secondary emission coefficients for all species. This assumption was made out of necessity, as it is knowns that the electron secondary emission coefficients are functions of the incident ions; the material of the surface; its roughness and grain structure. Considering that specific surface information such as the roughness and the grain structure is not available, a secondary emission coefficient of 0.05 was assumed on the dielectric surface. This value has been shown to be a typical value for slow ions incident on a dielectric surface [153].

3.2 Heat transfer module

As explained in section 3.1.4, the temperature of the discharge was assumed to be room temperature despite the experimental evidence showing that SBDs heat significantly when operating for extended periods of time. Accounting for this effect is important as a significant number of reaction coefficients depend on the gas temperature. Thus, it is important to quantify the variation in the chemistry due to gas heating. As part of this project, the baseline model was upgraded with a heat transfer module, for which details of implementation are given here, while the analysis of its results is presented in chapter 5.

From the plasma module, two additional quantities are time-integrated as the module is solved. These are the inelastic electron energy loss, as given by equation 3.6; in addition to the kinetic energy carried by the ions bombarding the dielectric surface. The instantaneous kinetic energy of bombarding ions is given by equation 3.16.

$$\Gamma_{heat} = \hat{n} \cdot \left(E_{N_2^+} \overrightarrow{\Gamma_{N_2^+}} + E_{O_2^+} \overrightarrow{\Gamma_{O_2^+}} + E_{O_2^-} \overrightarrow{\Gamma_{O_2^-}} \right) \tag{3.16}$$

In equation 3.16, E represents the kinetic energy of the ions written as a subscript, which is given by equation 3.17.

$$E_i = \frac{1}{2} m_i \left(\mu_i \vec{E} \right)^2 \tag{3.17}$$

Where the energy given in equation 3.17 represents the kinetic energy of the i^{th} species due to the drift in the electric field.

As soon as the plasma module is solved, the time-integrated quantities are used as an input to the heat equation, which is solved in the dielectric and the gas region. The heat equation is given by equation 3.18.

$$\rho C_p \frac{\partial T}{\partial t} = -\nabla \cdot (k \nabla \cdot T) + \bar{S}_{e,inelastic} \tag{3.18}$$

In equation 3.18, ρ is the mass density (kg·m^{-3}), taken from equation 3.14 (as solved in the gas) and is set to 3900 in the dielectric, which is the density of alumina. C_p is the heat capacity at constant pressure (J· kg^{-1}· K^{-1}), set equal to 1005 in air and 880 for the dielectric. k is the thermal conductivity coefficient (W·m^{-1}·K^{-1}), set to 0.03 in air and 30 for the dielectric. T is the temperature in the gas and the dielectric (K) and the last term is the time-averaged inelastic electron loss term computed by the plasma module. This term is only defined in the gas and it implies that all the inelastic collisional losses by the electrons are eventually dissipated as heat to the background gas.

The boundary conditions used for this module are given in table 3.6, where the order follows the numbers of the boundaries given in figure 3.3. The time-averaged kinetic energy carried by

the ions and imparted to the dielectric surface is assumed to be lost entirely as heat. Therefore, it is treated as heat flux directed toward the dielectric from the gas. This is justified by the experimental evidence that air plasmas in contact with an alumina surface show no evidence of sputtering despite extended periods of operation time [154]. Thus, both mechanisms were deemed unlikely to be significant. Data on energy reflection coefficients are scarce. Nevertheless, most available data indicates that the energy reflection coefficient for incident ions is low for normal incidence and is further reduced as the energy of the ions increases [155].

Boundary	Heat equation
1	T = 293 K
2	$-\hat{n} \cdot (\kappa \nabla T) = 0$
3	$-\hat{n} \cdot (\kappa \nabla T) = \bar{\Gamma}_{heat} + h(T - T_{dielectric})$
4	$-\hat{n} \cdot (\kappa \nabla T) = 0$

Table 3.6: Boundary conditions used in the heat transfer module. The location of each boundary is indicated in figure 3.3. *h* is the convective heat transfer coefficient which was set to 200 based on reported values in the literature.

The heat transfer module is then coupled to the chemistry module and the reactive flow module, where the gas temperature as a function of space and time is used to compute the rate coefficients of reactions depending on the gas temperature. It should be noted that solving self-consistently for temperature in the reactive flow module introduces density variations which may set buoyancy forces in action. However, for the range of parameters investigated in this work, it was found that the buoyant forces are negligible in comparison to the EHD forces. Combining that with the potential for numerical instabilities to appear as a result of adding buoyancy, it was ignored in this work. This is supported by many experimental observations that the induced flow in SBDs is directed down when the SBD is turned upside down, indicating that all other forces consistently dominate over buoyancy.

3.3 A multi-gap discharge configuration

Up until this point, all the model details discussed were applicable to a single discharge gap configuration. That is, a geometry with one grounded electrode and one driven electrode. In real-life settings, an SBD usually consists of multiple adjacent discharge gaps, which opens the door to the possibility of mutual interactions among the discharge gaps. To capture such interactions the model was upgraded in this work to have 6 adjacent discharge gaps instead of 1. While the upgrade did not involve major changes to the equations being solved, a practical challenge was encountered in relation to the symmetry of the discharge configurations, where small differences in the computational mesh used led to large differences in the computed solution. This problem was handled by imposing constraints on the mesh used, where the domain was split into smaller 'mesh sub-domains'. A fine mesh was generated in only one of the mesh sub-domains, then using the translational invariant method, the mesh was mapped in all other subdomains. This procedure resulted in a mesh with the highest possible symmetry to be constructed in the overall computational domain.

The computational domain for the multi-gap discharge configuration is shown in figure 3.4, which shows a zoomed-in view of the computational domain used by the plasma module, in addition to the larger domain of the reactive flow module. The boundary conditions used are numerated in the figure and are explained in table 3.7. The conditions used are almost identical to those used in table 3.5. The main difference is boundary 2, which in this case represents a sample placed downstream. From the flow's perspective this means that no flow can penetrate this surface and thus the flow velocity was set to 0. From the species' perspective, it is assumed that all reactive species arriving at the sample downstream react with it and get consumed in the reaction.

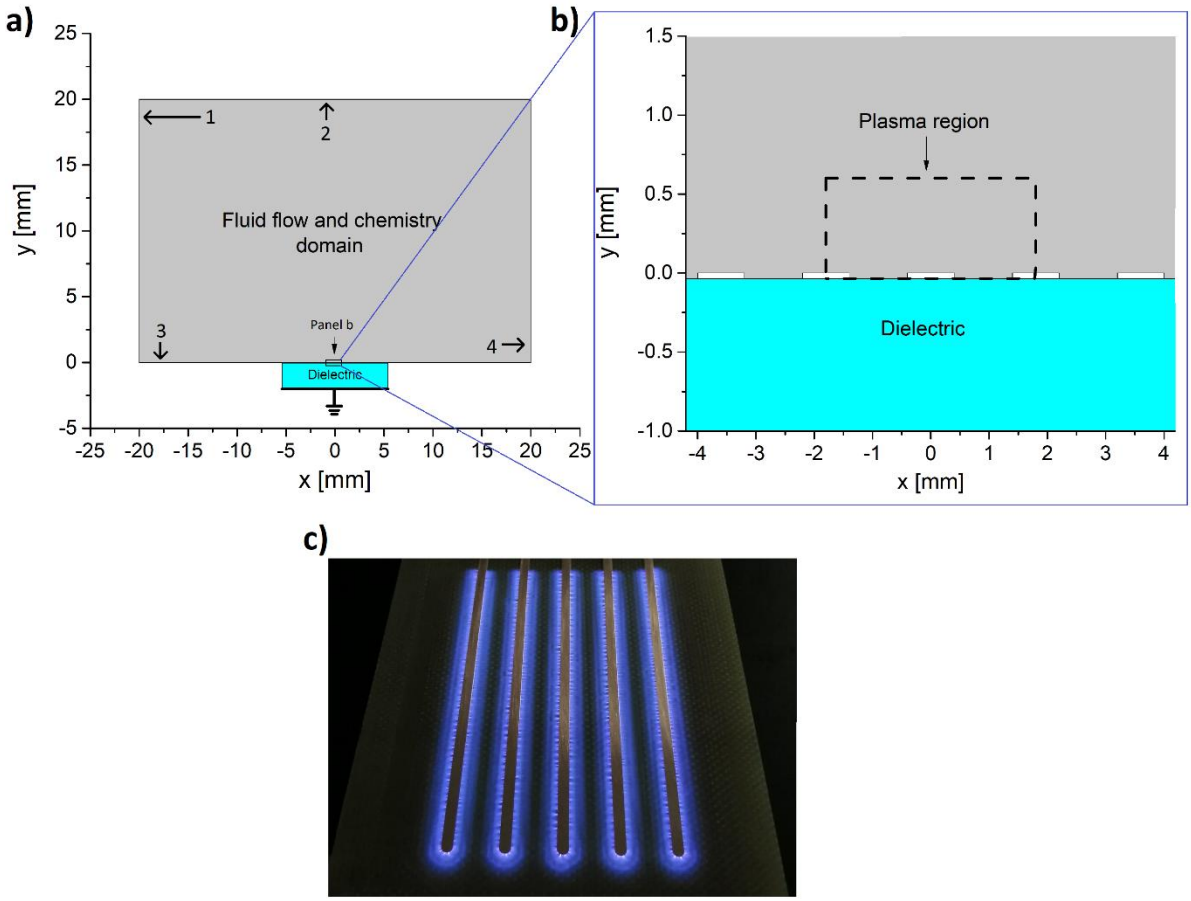

Figure 3.4: a) A diagram of the geometry used in the multi-gap discharge configuration model for an electrode width of 0.8 mm, numbers at the boundaries are used to indicate the boundary condition imposed in the model at each side of the computational domain; b) a zoomed-in view of the geometry showing the plasma region. The white rectangles represent driven electrodes, and c) a photograph of the plasma in discharge gaps.

Boundary	Boundary condition for the flow	Boundary condition for the species
1	$[-\nabla p + \nabla \cdot \tau] \cdot \hat{n} = 0$	$-\nabla c_i = 0$
2	$\vec{u} = 0$	$\vec{\Gamma}_i = \frac{-1}{4} c_i v_{th}$
3	$\vec{u} = 0$	$\nabla \cdot \vec{\Gamma}_i = 0$
4	$[-\nabla p + \nabla \cdot \tau] \cdot \hat{n} = 0$	$-\nabla c_i = 0$

Table 3.7: Boundary conditions used for the reactive flow module in the multi-gap discharge configuration. The numbers of the boundaries are indicated in figure 3.4.

3.4 Convergence criteria

In order to find the optimal balance between model accuracy and efficiency, modellers must follow a process called convergence testing. Here model parameters are varied, most commonly

the number of mesh elements, and the runtime and accuracy of the results are recorded. By plotting the error against runtime, the optimal value for that parameter is found, which has the minimum runtime while keeping the result within an acceptable error. As fluid models have many initial parameters, an ideal convergence test would be run across all of these parameters. However, minimizing a multi-dimensional function such as this is a very complex problem and the time this would take is not justifiable. Instead, each parameter is optimised individually. This approach assumes the ideal value of each parameter is not dependent on the values of the other parameters. This may not be entirely true but is unlikely to make a large difference. It is possible that this procedure leads us to a local minimum in efficiency that is not the global minimum. However, while improved efficiency is always desired, it is not essential that the model is the most efficient possible, rather that it is sufficiently accurate whilst running within a convenient timeframe.

Convergence testing was extensively performed throughout the model setup and repeated for each new investigation described in chapters 4, 5 & 6. There is far too much data to show in full here but as an example, below is the convergence testing carried out for the flow dynamics module prior to the investigation detailed in chapter 6 to determine the optimal mesh size. The number of mesh elements was varied and both the simulation runtimes and the maximum NO_2 density values were recorded. This was chosen as a barometer value to determine when the results are converging. Of course, many different values could have been chosen for this but NO_2 density was chosen as it is one of the key outputs. There are flaws in picking a single value to determine convergence of a two-dimensional many-element system but it is simplest to track a single value. The flow module was run to simulate just 1 second in order to save time.

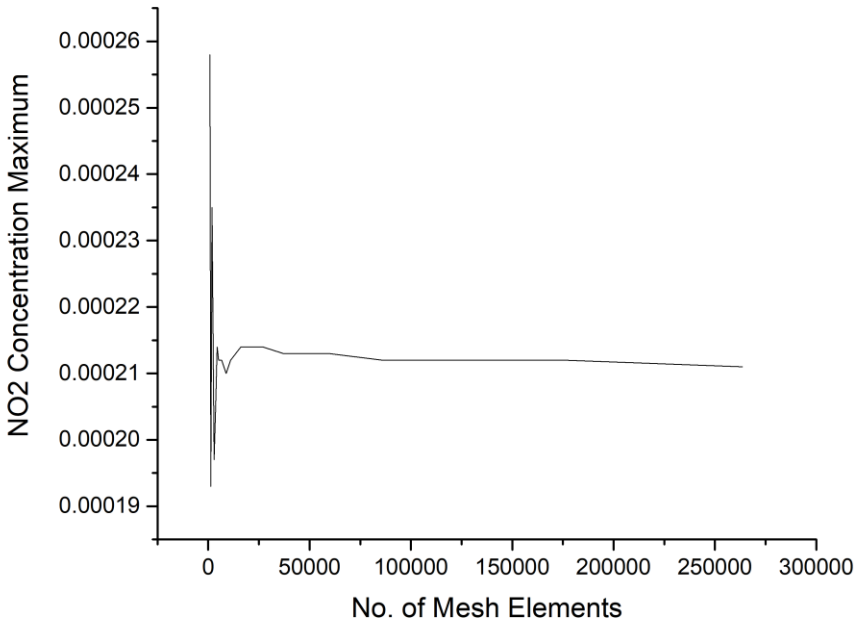

Figure 3.5: Variation of maximum NO_2 Concentration against the number of mesh elements used in the simulation.

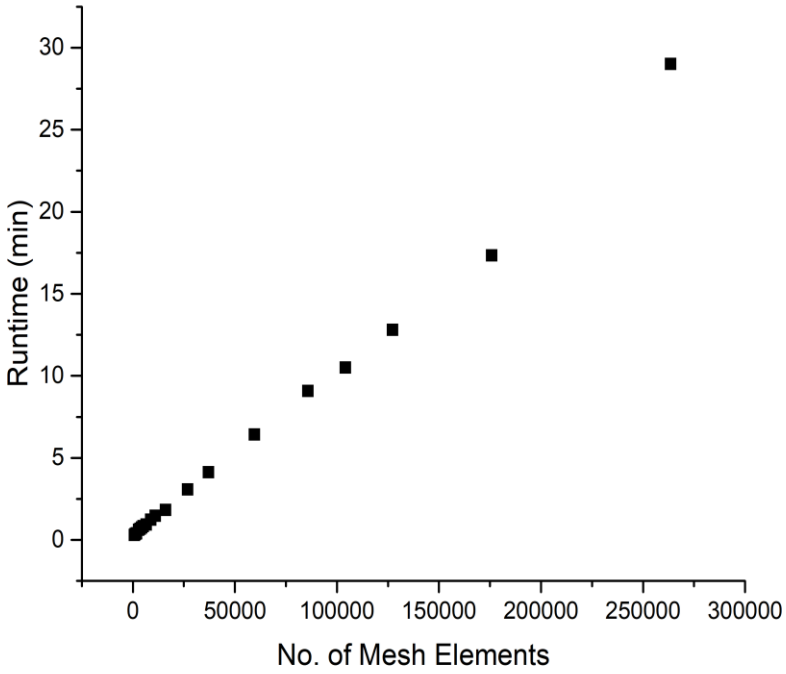

Figure 3.6: Simulation time required against the number of mesh elements used.

Figure 3.6 shows that the simulation time increases almost exactly linearly with the number of mesh elements, unsurprising as the total number of calculations that the programme needs to make depends on the number of mesh elements. However, this will not always be the case as a coarser mesh can lead to smaller timesteps being needed to resolve the system. The test case here was a very simple one so this was not an issue.

Figure 3.5 shows how the calculated maximum NO_2 density changed with mesh density. Below 2000 mesh points the value calculated varied a lot but by 5000 elements it had converged to within an error of 1% which is sufficient. This would suggest a mesh of 5000 elements would be sufficient and while in a simple case for a quick calculation it might be, there are several reasons why a much finer mesh was used in our research. Firstly, the test case above is much simpler than those used in our research and is, therefore, more stable. So, while convergence is reached for 5000 elements here it would likely not do so until a much finer mesh in other cases. A mesh this coarse is much more susceptible to crashes and singularities, which would cost a lot more time to the researcher than would be gained through the quicker runtimes. 5000 is a relatively small number of elements and limits the precision that can be given in spatial distributions produced by the simulation. It is possible at this precision level that some of the physics is happening on a smaller scale than this and would be entirely missed by the simulation. Finally, the advantage of a simulation that runs for $\sim$ 5 minutes is not that great over one that takes $\sim$ 1 hour. It is useful in the test phase but an hour is not a long time to wait to produce results of a publishable standard, so there is no need to compromise on precision to this degree.

3.5 Comparisons of simulations and experiments

The model and its variants described above must be validated through comparison with experiments to ensure that their predictions can be trusted, as it is very easy for models which have not been properly calibrated to produce unreasonable results. Such validations are

provided in chapters 5 and 6. However, it is worth commenting on some general principles of comparisons between simulations and experiments.

In both modelling and experiment, some magnitude of error is always expected. In experiments, this can be due to the precision of measuring apparatus, background noise and environmental influence, human error or a flawed measurement methodology. In modelling, measurement errors are removed. Computers do make small random errors all the time, but they rarely produce significant errors. Human error is removed from much of the process but it is still possible for input values to be wrong or analysis to be performed incorrectly on the model outputs. Far more of the emphasis is left on the methodology, where flaws are often not obvious. The other difference is that models are describing an ideal system, which they may do very accurately but this may not match experimental results where large environmental influences are present that the model has not considered.

Another important consideration when comparing simulation and experiment is whether the same quantity is actually being considered. For example, in SBDs it is often desirable to measure the plasma power. In the laboratory, the instantaneous power is measured via an oscilloscope. This instantaneous power includes a reactive component, which is stored in the circuit. The model can only predict the power dissipated by the discharge, which has no reactive component. Hence the model and the experiment are considering two different variables and would not be expected to produce the same value. In all comparisons between simulation and experiment, how comparable the predicted and measured values are must be carefully considered.

In the field of discharge modelling, errors vary quite considerably but modelling errors of ~10-20% are typical. This is higher than seen in some areas of physics, due to the highly chaotic system and the lack of protection from environmental interference. While reducing these errors is important, in my applications what is most important is that the model can predict how the

system will change under certain conditions. This is useful when considering new configurations and shows that the model correctly describes the physics of the system.

4. Influence of humidity on the chemistry of surface barrier discharges

The first step in this work was getting used to the baseline model. As an exercise, the baseline model was used to investigate the effect of humidity on the chemistry induced in SBDs. The findings of this investigation are reported in this chapter. This analysis has not been reported in the literature.

For most practical applications it is desired to use ambient air as the working gas as it reduces the cost of operation and simultaneously reduces the complexity of the machine where SBD is mounted.

Considering that relative humidity changes on daily basis, it is important to quantify its influence on the resultant chemistry in the discharge to ensure the consistency of the treatment using an SBD. In particular, it has been shown experimentally that humidity decreases the generation of O_3 and N_2O while increasing the production of NO_2 when the discharge operates in a closed environment [156, 157]. The intention of this research was to find how changing humidity changes the production of all the dominant long-lived species in SBDs.

4.1 Methods

The details of the numerical model used to generate results in this chapter were given in chapter 3. They will be not repeated here. This section provides the input to the model used in this study.

The geometry used in the model had a single discharge gap of width 15 mm. The discharge consisted of two 35 μm copper-tape strips that functioned as the driven electrodes. They were assumed to be driven by a sinusoidal signal with an adjustable amplitude of around 13 kV peak to peak and a frequency of operation of 18 kHz. The grounded electrode was also assumed to be a copper-taped electrode that was mounted on the other side of the dielectric. The dielectric

was assumed to be made of 2 mm thick quartz. The discharge operated at atmospheric pressure in air at room temperature, which was set as 298 K.

To analyse the effect of the humidity, a parametric study was conducted, where the mole fraction of H_2O in the gas was varied by 5 steps. The steps were 0, 25%, 50%, 75% and 100% of the saturation point of water vapour at 298 K and atmospheric pressure, which corresponded to a mole fraction of 0.023. To account for the varying water vapour content. The mole fractions of O_2 and N_2 were given by equations 4.1 and 4.2 respectively. All the simulations were run in a constant power mode, where the voltage was adjusted to keep the power deposited in the discharge constant. The model assumed that the discharge operated in an open-air environment, allowing for fresh air to flow into the discharge region and for the generated species to be transported without a chance of a return to the plasma region. There was no gas flow in the model other than that induced by the plasma. Thus, no accumulation of species occurred. This assumption was made as most of the applications where SBDS are utilised, on production lines, for example, operate in open air.

$$x_{O_2} = 0.21\left(1 - x_{H_2O}\right) \tag{4.1}$$

$$x_{N_2} = 0.79\left(1 - x_{H_2O}\right) \tag{4.2}$$

In these equations, x_{N2}, x_{O2}, and x_{H2O} are the mole fractions of N_2, O_2 and H_2O respectively.

4.2 Results & discussion

The analysis of the results was based on the species behaviour as computed by the reactive flow module. First, species solved for in the module were classified based on their general behaviour. Then species were classified based on how their densities changed in response to varying the water content of the gas.

4.2.1 *Short-lived vs long-lived species*

All species solved for in the reactive flow module exhibited one of two behaviours, the first is typical of a short-lived species, where the density of the species is confined to the discharge

region. An example of this behaviour is shown in figure 4.1 panel a) which shows the density of atomic oxygen. As can be clearly seen, the concentration only has non-zero values in the spots where the electron impact chemistry is maximal. The reason for this is that atomic oxygen is rapidly converted into another more stable species. This conversion takes place on a timescale much shorter than that of diffusion or convection. Other species that fall into this category are N, O_2 ($a^1\Delta$), OH, NO_3, HNO and HO_2.

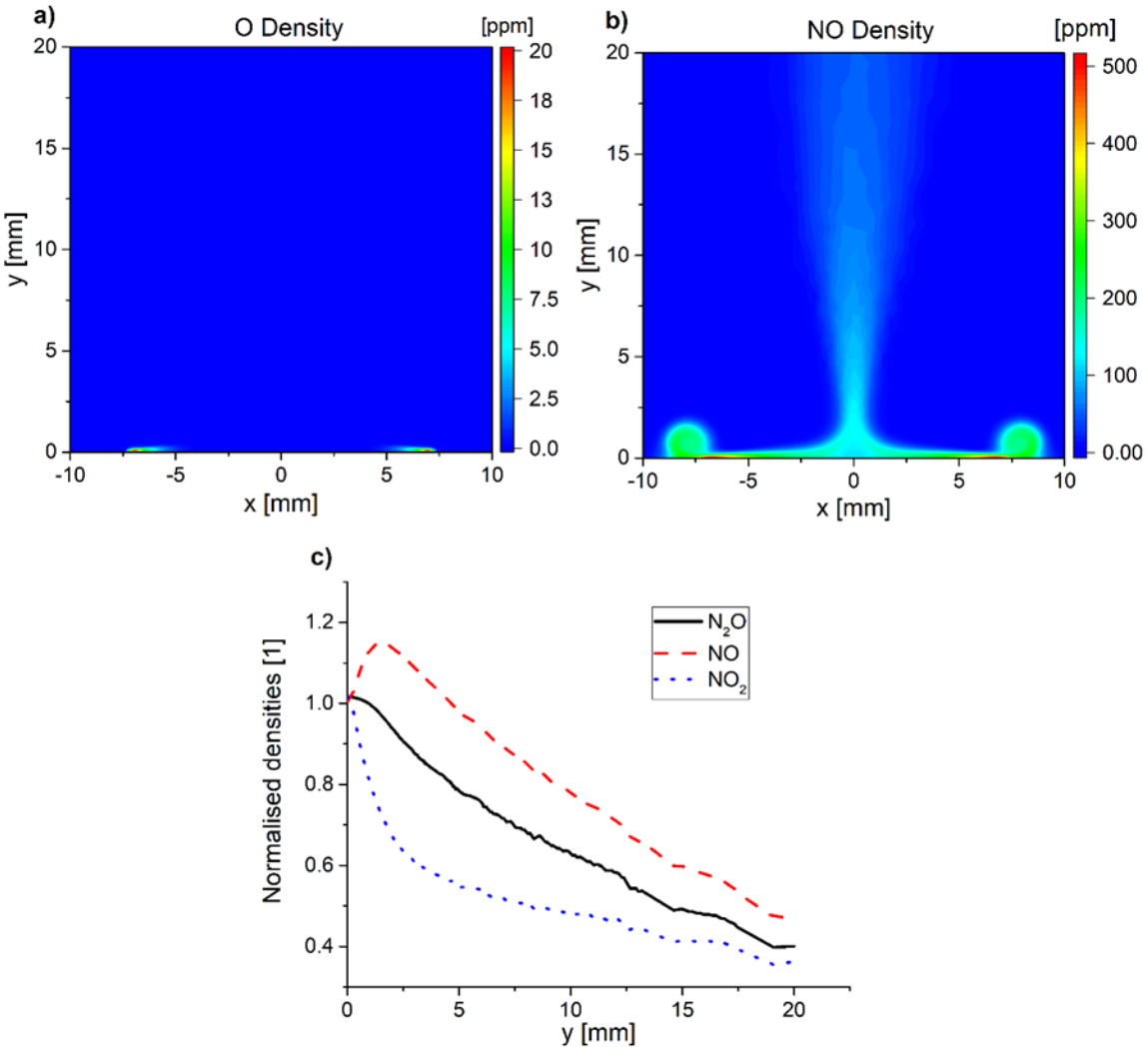

Figure 4.1: a) The 2D density distribution of atomic oxygen, which shows typical behaviour for a short-lived species; b) The 2D density distribution of NO, which shows typical behaviour for a long-lived species; c) the densities of N_2O, NO and NO_2 along the axis of the perpendicular jet flow from the SBD in steady-state.

The other category is the long-lived species, where the lifetime of the species is long enough for them to experience transport processes such as convection or diffusion. As a result, their 2D distribution follows the flow pattern of the background gas. An example of this behaviour is shown for NO in figure 4.1 panel b). This category encompasses all other species in the reactive flow module which are not in the short-lived species category, thus it includes O_3, N_2O, NO_2, N_2O_3, N_2O_4, N_2O_5, HNO_2, HNO_3, N_2O_5, H_2O_2, and H_2.

It should be noted here that while all long-lived species have similar spatial distribution, they differ significantly in other aspects. For example, the densities of N_2O_3, N_2O_4 and H_2O_2 are typically three orders of magnitude lower than the densities of other species. The same applies to H_2O_2 and H_2 when the water vapour is close to the saturation limit. Another difference is the behaviour of the species in the downstream perpendicular flow/jet as highlighted in figure 4.1 panel b). The density of all species decreases along the axis of the jet due to the radial spread of the jet. Nevertheless, the decrease rate varies among species. For example, as figure 4.1 panel c) shows, N_2O has a moderate decrease in density from the peak value as one moves downstream. By comparison, NO_2 starts to decline faster than N_2O. Moving further downstream, the decline in NO_2 starts to level off. The behaviour of NO is the opposite of that of NO_2, where its density decreases faster downstream. The reason for that is the reactions take place downstream. NO is consumed by reaction R1 as it is transported downstream, which adds to the density decrease rate.

$$NO + O_3 \rightarrow NO_2 + O_2 \qquad \text{(R1)}$$

N_2O does not experience any reaction while moving downstream, and thus the only reason behind the decline in its density is the widening of the jet. Lastly, NO_2 is being generated in the jet as a result of reaction R1, which partially counteracts the widening jet effect.

4.2.2 *Hydrogen-containing species densities as functions of water vapour*

Considering that H_2O is the only source of hydrogen in any generated reactive species, it is trivial to expect that increasing the water content of the background gas will lead to an increase in the densities of hydrogen-dependent species. However, the rate at which the density increases as a function of water density is non-trivial as it depends on the chemical kinetics of the discharge. To illustrate that, the average density of HNO_2 and HNO_3 in the discharge region is plotted as a function of water content in the background gas in figure 4.2. These two species are chosen as they are the only hydrogen-containing species with densities larger than 1 ppm. While the densities increase with water content as expected, the increase rate is not 1 to 1. Furthermore, the rate of increase in HNO_3 is slower than that of HNO_2.

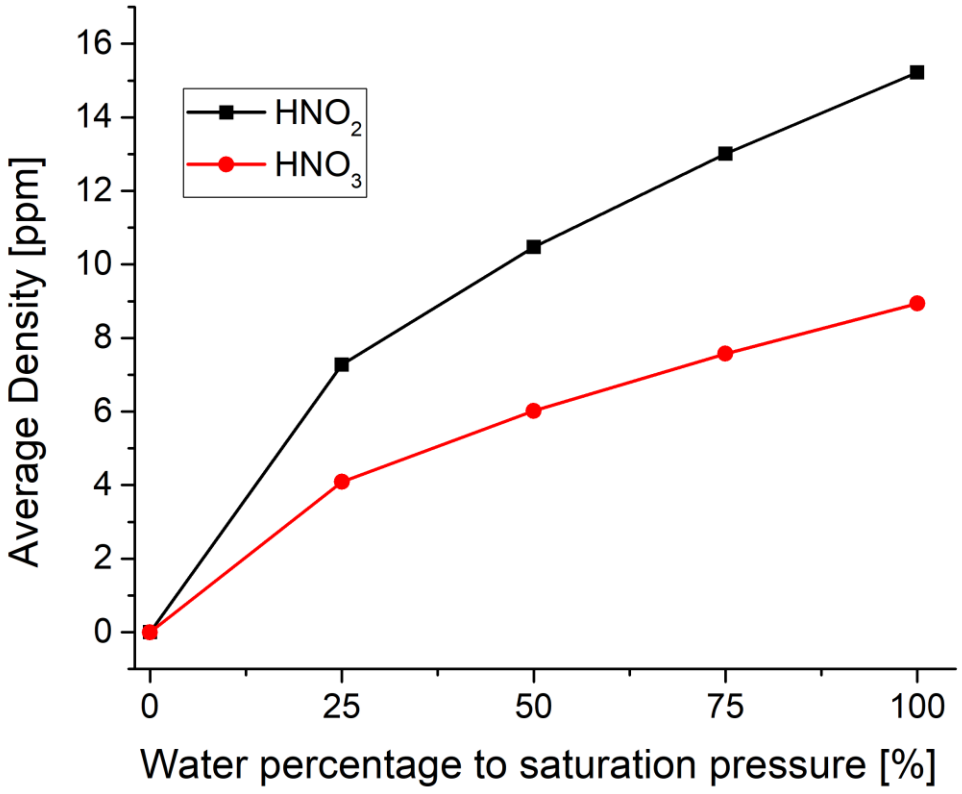

Figure 4.2: The average densities in the discharge region as a function of water vapour concentration, normalised to the water vapour concentration corresponding to the saturation pressure under ambient conditions.

Another observation from figure 4.2 is that the slope of the densities of HNO_2 and HNO_3 seem to change at a concentration of 25%. This behaviour can be understood by examining the dominant chemical pathways for generating the species, as given by reactions R2 and R3.

$$NO + OH + M \rightarrow HNO_2 + M \quad \text{(R2)}$$

$$NO_2 + OH + M \rightarrow HNO_3 + M \quad \text{(R3)}$$

Where M in reactions R2 and R3 is a third body. It is clear from these equations that the generation rates of both species depend on the OH density on one hand and the density of NO and NO_2 on the other hand. Starting with OH density, the maximum OH density is shown in figure 4.3.

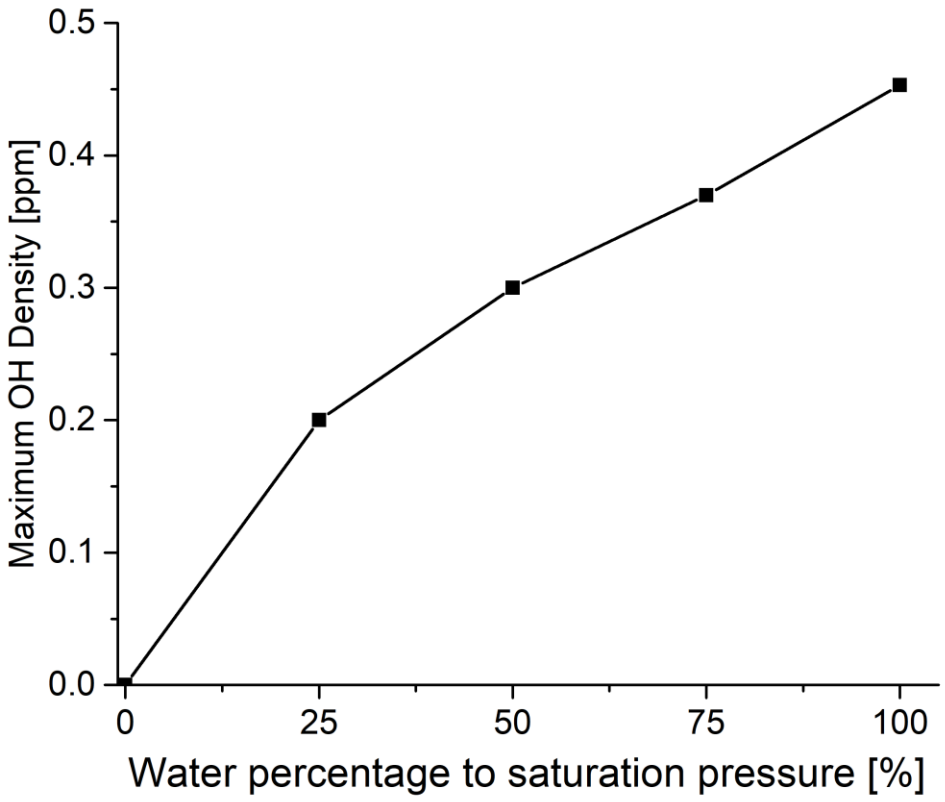

Figure 4.3: The maximum OH density as a function of water concentration, normalised to the water concentration corresponding to the saturation pressure under ambient conditions.

The resemblance between figure 4.2 and figure 4.3 shows that the increase in the density of HNO_2 and HNO_3 is dominated by the behaviour of OH. Since the primary source of OH is the electron impact dissociation of water, when the water percentage is less than 25% the added water behaves as an impurity with lower ionisation energy than nitrogen without affecting the discharge dynamics. Therefore, increasing the water concentration caused a proportional increase in the density of OH. Beyond 25%, the water vapour starts to affect the discharge by requiring an increase in the applied voltage to keep the power constant, which is a result of water molecules being electronegative. This negative impact decelerates the rate at which the increase of OH follows the increase of the water vapour.

Since OH is a common factor between the two species investigated in this section, it cannot explain why the density of HNO_2 increases faster than that of HNO_3. The faster increase is due to the other reactants, which are NO and NO_2 respectively. As discussed in section 4.3.1, NO_2 is generated from NO via reaction R1, which means that NO reacts to generate NO_2 as it is transported downstream. Thus, the density of NO is always larger than that of NO_2 in the discharge region. Considering that OH, the other reactant, is confined to the discharge region, this means that the reaction between NO and OH (R2) will dominate over R3, leading to a higher generation of HNO_2.

4.2.3 *Hydrogen-free species densities as functions of water vapour*

The influence of water vapour on the density of hydrogen-free species was marginal. To emphasise that, figure 4.4 shows the averaged densities in the discharge region of many species normalised to their density at 0 water vapour content. The species affected the most were NO and N_2O_5, which fell by approximately 4%. The loss in NO can be explained by reaction R2, where the presence of water vapour adds a loss channel for NO to be converted into HNO_2. For N_2O_5, the dominant generation reaction is R4.

$$NO_2 + NO_3 + M \rightarrow N_2O_5 + M \qquad \text{(R4)}$$

Since NO_2 is consumed by reaction R3, which depends on the water content, the loss in NO_2 is cascaded in the density of N_2O_5. The loss of NO_2 is less than that of NO as a result of NO_2 being generated downstream (i.e. away from the region where OH attains its peak value). The only species that showed an increase in density is atomic oxygen, which is attributed to the reaction R5. Which is present in the reactive flow module through the term G_O, representing the generation routes of atomic oxygen due to short-lived species.

$$e + H_2O \rightarrow H_2^+ + O + 2e \qquad \text{(R5)}$$

It should be noted that this reaction is a minor source of atomic oxygen and that the main generation rate for atomic oxygen is electron-impact O_2 dissociation. Hence the influence of water vapour on O density is marginal.

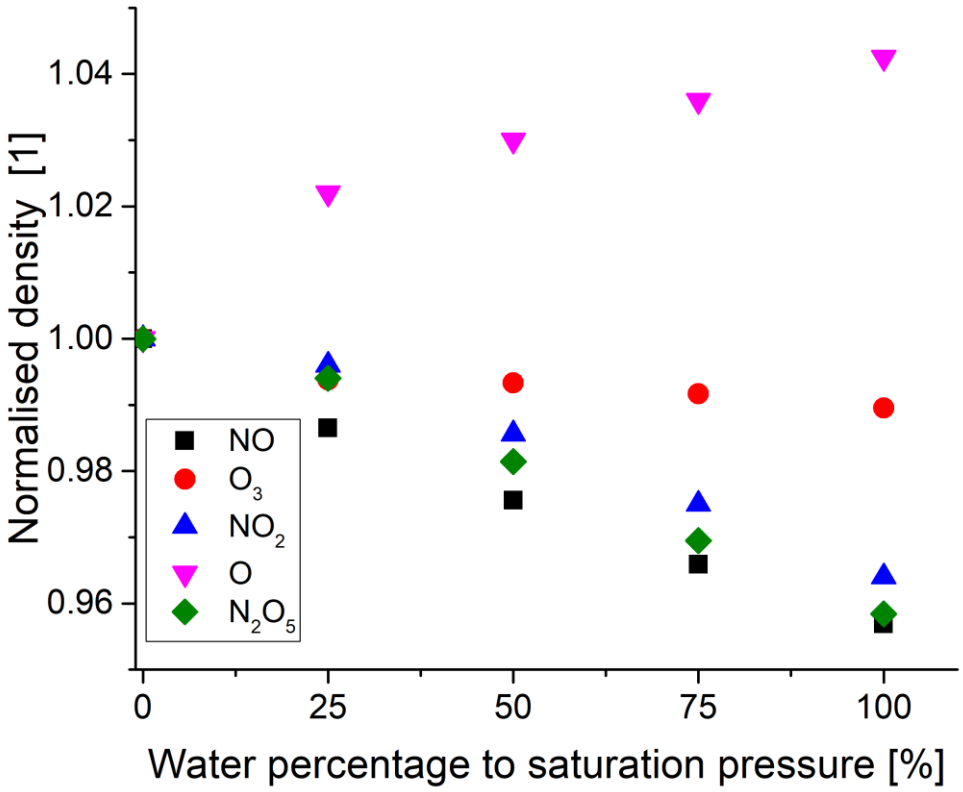

Figure 4.4: The normalised average densities of many species in the discharge region as a function of water vapour concentration in the background gas. The normalisation factor is the density of every species at 0 water vapour concentration in the background gas.

The last species shown in figure 4.4 is O_3, which shows a marginal decrease in density as the water vapour is increased. The density of ozone is affected due to the presence of water in two ways. First, considering that the main loss reaction of O_3 is with NO to generate NO_2 as given by reaction R2. Since the density of NO is decreased by reacting with OH, the loss rate of ozone decreases as there is less NO for O_3 to react with. Second, considering that the main generation mechanism of O_3 is given by reaction R6, an increase in the water vapour will come at the expense of the density of O which is a reactant in forming O_3. The net result is that the reaction rate of reaction R6 decreases due to the smaller O_2 density despite the marginal increase in the density of O.

$$O + O_2 + M \rightarrow O_3 + M \qquad \text{(R6)}$$

It should be noted here that the marginal differences reported here are largely due to the fact that a single discharge gap is operating in open air. The consequence of this is that accumulation does not occur and the discharge arrives at its steady-state behaviour on a timescale of milliseconds. For discharges operating in closed environments, accumulation of reactive species does take place and the chemistry of the discharge continually changes on a timescale of minutes. Thus, we anticipate the differences due to the change in humidity will grow with time when the discharge is operated in a closed environment. Moreover, in a closed environment, ozone quenching occurs which may change some of the behaviour reported here significantly.

4.3 Conclusion

In this chapter, the effect of varying humidity on discharge performance as a source of reactive species was investigated. The investigation focused on the change of the resultant species chemistry as humidity changed. Such an investigation is useful for providing information on the fluctuation of the generated chemistry in an SBD-dependent system from day to day or from one season to another.

It was shown that increasing the humidity of the background gas increased the density of hydrogen-containing species such as HNO_2 and HNO_3 at a rate slower than that of the change in humidity. The increase is driven by the variation in the OH density which is a pre-cursor of both species. The density of OH was shown to increase rapidly for low humidity, then to increase more slowly for higher humidity values. This was attributed to H_2O acting as a 'trace' species in the low humidity range, providing OH density proportional to that of H_2O. While at higher humidity values H_2O started to affect the evolution of the discharge as it is an electronegative species.

With respect to hydrogen-free species, the change in their densities was shown to be marginal. Most species showed a slight decrease in density due to the introduction of chemical pathways (i.e. reactions) which have hydrogen-free species as reactants. The only exception was atomic

oxygen which showed a marginal increase as a result of electron impact dissociation of water into H_2 and atomic oxygen.

The results reported in this chapter are valid under low power and in an open-air environment. It is anticipated that in a closed environment the difference due to the variation in humidity will be amplified due to the accumulation of the species in the closed environment. Furthermore, operating at higher powers will trigger ozone quenching which is expected to have an impact on the behaviour of NO_2.

In conclusion, this chapter shows that the variation in humidity in an open air environment will be unlikely to significantly affect the resultant chemistry of SBD discharges, adding another advantage to using them as sources of reactive species.

Chapter 5: Dominant heating mechanisms in a surface barrier discharge

In this chapter, the model was used to investigate heat transfer in SBDs. The aims of this study were to determine the dominant heating mechanism in SBDs and to quantify the influence of a heated SBD on the resultant chemistry of the discharge. The experiment performed to validate the results in this chapter was performed by Dr. Aaron Dickenson whilst all simulations and results analysis were my own work. The analysis presented in this chapter was published in the Journal of Applied Physics D.

5.1 Introduction and motivation

A common simplifying assumption in many numerical models is that both the discharge and the dielectric have a constant, uniform temperature distribution throughout. Experimentally, atmospheric pressure discharges in air are known to heat up as they operate for an extended period, where they take minutes of operation until arriving at their steady-state operating temperatures. A noticeable change in the gas temperature can influence multiple aspects of the discharge. These include a change in the electron and ion transport properties; chemical reaction rates; maximum streamer velocity; sheath thickness and maximum streamer length [104]. Some reaction coefficients are highly sensitive to temperature. For example, the rate coefficient of the reaction between O_3 and NO that generates NO_2, being one of the dominant reactions for generating NO_2 [132], increases by 32% for an increase of 20 °C from room temperature. Clearly, an accumulation of such factors in large chemistry models could alter the results significantly, ultimately resulting in large errors in the predicted densities of the species involved in those reactions.

Considering that SBDs consist of many streamers with a high power density yet typically short duration of tens of nanoseconds [26], it is possible to identify the potential routes of heat transfer in a typical SBD. When the plasma is first ignited in air it is known to heat the gas at the

point of ignition [11], primarily through electron–gas molecule collisions, which can lead to convective heat transfer to the dielectric surface. This mechanism is referred to as electron heating. Secondly, when streamers propagate on the dielectric surface, ions from the streamer heads bombard the dielectric surface with relatively high energy that may extend up to hundreds of eV [158]. The kinetic energy of the ions then dissipates into the dielectric as heat, causing the dielectric temperature to rise and thus causing a convective heat transfer from the dielectric to the gas. This is referred to as ion-flux heating. A third potential mechanism is dielectric heating. This occurs due to a time-varying electric field in the GHz frequency range, where a peak exists in the imaginary component of the permittivity for most dielectric materials [159]. Physically this means that the dielectric molecules align themselves with the electric field lines. As the field is constantly oscillating, the molecules continually rotate to re-align, dissipating their kinetic energy into heat, causing the dielectric temperature to rise. This causes convective heat transfer from the dielectric to the gas.

5.1 Methods

The model used in this study was discussed in chapter 3. The geometry used in the model describes that of an experimental setup shown in Figure 5.1, which was used to validate the model by comparing the measured dielectric temperature to that predicted by the model under identical operational parameters.

5.2.1 *Experimental setup*

To validate the model, an experiment was set up to measure the average temperature increase in the dielectric of an SBD. The dielectric was a 2 mm thick slab made from alumina (Al_2O_3), while aluminium (Al) was used to form the 4-fingered shape powered electrode around which the discharge formed, as seen operating in Figure 5.1d). The powered electrode measured 35 mm across and 35 mm long, with 4 fingers with widths of 5 mm and lengths of 30 mm, each separated by a 5 mm gap. The ground electrode was formed by a planar aluminium sheet

measuring 40 x 40 mm^2 adhered to the opposing side of the dielectric. A K-type thermocouple was attached to the alumina surface near the powered electrode using thermally conductive epoxy and was used to measure the temperature of the dielectric during discharge operation. The thermocouple was attached to the dielectric at one of its corners. The point of attachment made no difference to the measured temperature.

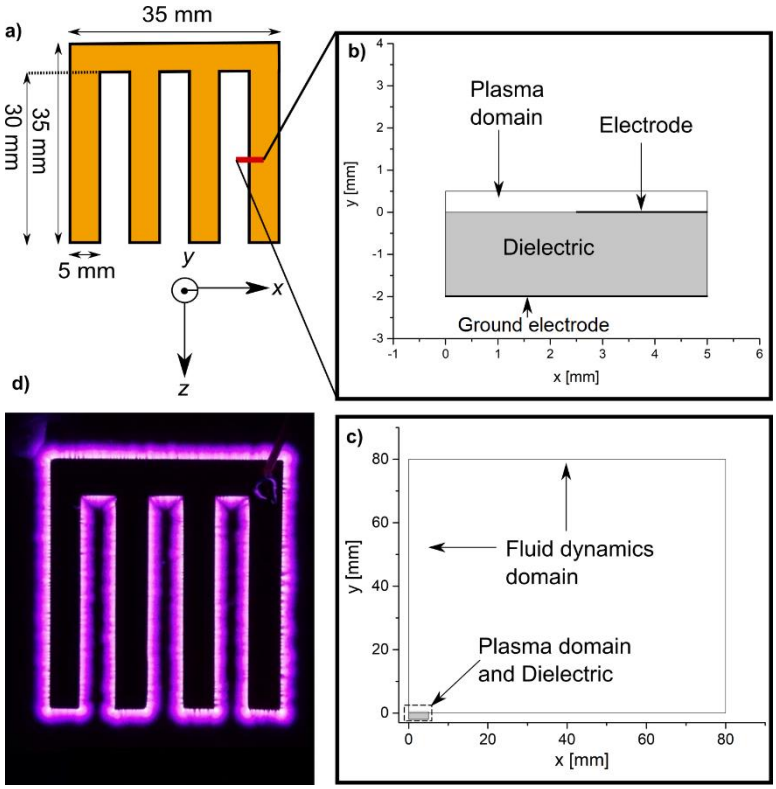

Figure 5.1: a) Schematic of the electrode geometry; b) Close-up of the computational domain of the model; c) Complete computational domain; d) an image of the electrode during discharge operation.

The experiment was carried out at atmospheric pressure with the ambient environment being at a typical room temperature of 299 K. The setup was not insulated in any way, so heat could be freely convected away from the SBD. A homemade power source was used to apply a 25 kHz sinusoidal voltage, with a variable voltage to the powered electrode. Current and Voltage waveforms were recorded on a Tektronix DPO 5054 digital oscilloscope using a Pearson 115617 current probe and a Tektronix P6015A voltage probe. The discharge power was calculated by oscilloscope by multiplying the current and the voltage waveforms and averaging the product over multiple periods. Temperature measurements were taken every 10 seconds

for the first minute of operation, then every 60 seconds after that for discharge powers of 5, 10 and 15 W.

5.2.2 *Approach for modelling streamers*

Typically, plasma created on the surface of an SBD consists of streamers which are thin plasma filaments, with typical widths of 10-100 μm, that propagate at typical speeds of 10^6 m·s^{-1} above the dielectric surface. They have a high current density and a short lifetime of a few to tens of nanoseconds [11]. Figure 5.2 panel a) shows the instantaneous power in two cycles of the discharge, where every point is an average of 100 cycles, processed and calculated using MATLAB [160]. The power spikes both in the positive and negative half-cycle, which are clearly visible in Figure 5.2 panel b), are attributed to streamers forming in the discharge.

As Figure 5.2 panel c) shows, there are multiple localized streamers on the dielectric surface at a given time. This poses a challenge to any 2D model because it does not allow multiple streamers to ignite and propagate independently from one another. Consequently, applying a sinusoidal waveform in the model, despite being more consistent with experiments, will inevitably lead to a non-physical interaction between the streamers as they are forced into forming at the same position. To address this problem, an effective waveform was conceived and implemented to facilitate a direct comparison with the experimentally applied sinusoidal waveform. Both waveforms lead to the same time-averaged plasma power. It should be noted that this approach provides a compromise by partially capturing the filamentary nature of the discharge without the computational complexity of 3D models required to fully resolve the filaments. The approach used does not capture the independent nature of the different filaments igniting at different positions and different times on the electrode.

The effective waveform is a standard pulsed waveform with controllable rise time and fall time. Its use aims to capture the filamentary nature of the discharge driving the discharge into a high-density short lifetime mode, which are the typical characteristics of filamentary or streamer discharges. This effective waveform generates two streamers, one on the rising edge and one on

the falling edge. The time at which these streamers are ignited can be controlled simply by shifting the rise and fall times in the period of the applied waveform. The duration of the discharge can be controlled by controlling the duration of the rise and fall times, longer rise and fall times mean longer discharge or filament lifetimes. Lastly, to control the power in the streamer or the filament, the rate of change of the voltage (in V/s) can be changed. For higher power densities a higher voltage change rate is required.

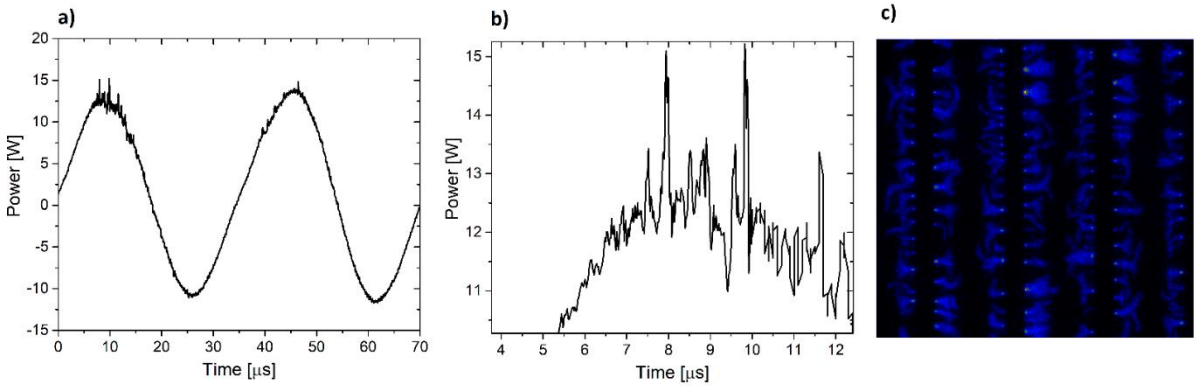

Figure 5.2: a) Plot of the experimentally observed instantaneous power over two periods; b) a zoomed-in view of the instantaneous power in the positive cycle; c) ICCD images showing the streamers on the SBD. The panels shown in this figure are all for the 5 W case.

To analyze the influence of the non-physical interaction between streamers as a result of using a 2D model to describe a 3D phenomenon, the model was run with two different waveforms. The first was a sinusoidal waveform with parameters matching those in the experimental setup. The second was an 'effective' pulsed waveform that is representative of a single streamer, where the rising and the falling edges of the pulse represent streamers in the positive half-cycle and the negative half-cycle of the sinusoidal applied waveform respectively. The rise and fall times of the effective waveform were chosen such that the power deposited in the model agrees with that reported in the experimental setup.

The model was solved using the two waveforms for plasma powers of both 5 & 10 W. All the geometric parameters and the material properties used in the model were set to match the experimental setup. The powers calculated by the model deviated by less than 10% from the corresponding experimental powers.

5.1 Results & discussion

5.3.1 *Sinusoidal versus effective excitation of the model*

Despite the two waveforms resulting in a similar deposited power in the model, the plasma parameters were found to be very different. Figure 5.3 shows the logarithms of the electron density at the time where the peak instantaneous power is reached for 5.3 panel a: the sinusoidal case and 5.3 panel b: the effective pulsed case. It is clear from a comparison of the peak electron densities that the effective pulsed waveform yields an electron density two orders of magnitude higher than that achieved with the sinusoidal waveform. Notably, the densities calculated for the pulsed case are closer to those reported for streamers in an air plasma [161, 162, 163], compared to those calculated for the sinusoidal case.

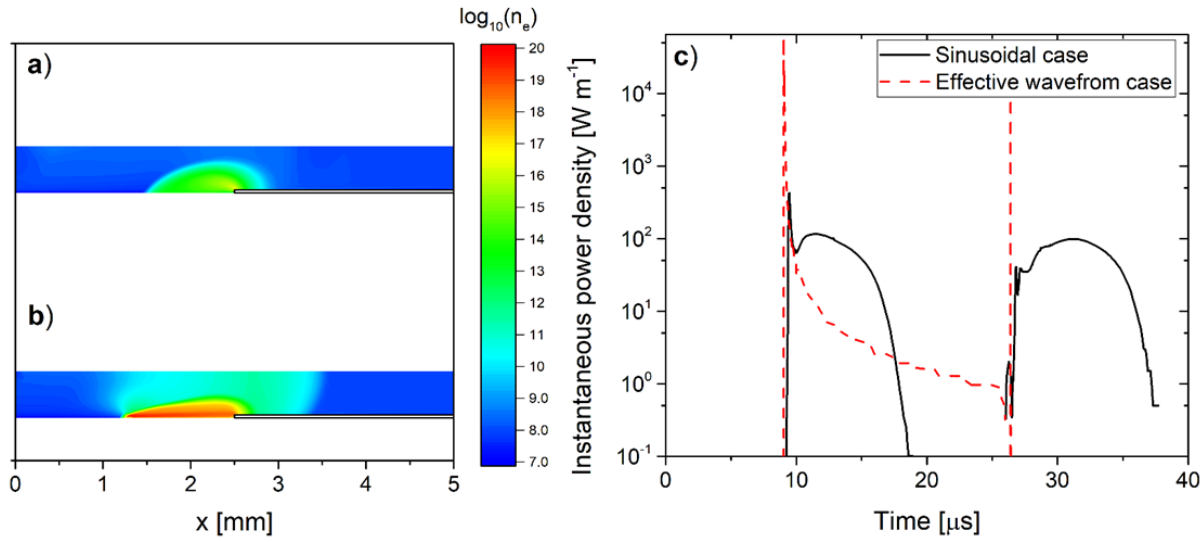

Figure 5.3: The logarithm of the electron density when the instantaneous power is at maximum assuming a) sinusoidal waveform; b) effective waveform; c) a comparison of the instantaneous power density at the electrode between the sinusoidal case and the effective pulsed case. The curve seems discontinuous as the values drop below 0.1, which was chosen as the lower limit to highlight the details of the plotted curve. The instantaneous power at a given time is defined as the product of the voltage at the electrode at that time, multiplied by the surface integral of all charged species fluxes to the electrode at that time, which gives the current and consequently the power at that time.

The changes in the discharge produced by the two waveforms can be explained by Figure 5.3 panel c), which shows the instantaneous power density for both waveforms. The sinusoidal

waveform has a lower instantaneous power density over a long period. On the other hand, the effective pulsed waveform has a higher instantaneous power density over a short period. Having a higher power density leads to having a high electron density. It should be noted here that Figure 5.3 panel c) shows the calculated dissipated power; this is not the same as the experimentally measured instantaneous power, shown in Figure 5.2, which includes a reactive contribution that cannot be removed.

Figure 5.3 panel c) also shows that the instantaneous power in the sinusoidal case, despite being driven by a waveform that matches experiments, shows a significant deviation from the spikes shown in Figure 5.2. While the instantaneous power in the effective waveform closely resembles the high-amplitude, short-duration spike observed in the measured experimental data shown in Figure 5.2 panel b). This implies that the most suitable description of an SBD is determined by whether the phenomena of interest stems from the filamentary nature of the discharge or the average behaviour of all filaments. For example, studies of EHD force-induced flow in sinusoidal SBDs have shown to be captured correctly by models with sinusoidal excitation [164].

5.3.2 *Model validation*

Whether or not heat transfer in an SBD is driven by the filamentary nature of the discharge can be inferred by solving the heat equation for both waveforms. Experimental validation of the model, in addition to providing information on the quantitative agreement between the model and the experimental setup, also enables identification of the most suitable description to follow when modelling heat transfer in SBDs. The time-averaged heat flux to the dielectric surface by both excitations is shown in Figure 5.4 panel a), where it can be observed that the time-averaged heat flux in the effective excitation case is three orders of magnitude higher than that of the sinusoidal excitation case. This is a direct consequence of the difference in the plasma conditions as discussed in section 5.3.1.

Figure 5.4 panel b) shows a comparison between the measured average temperature of the dielectric and those computed by the model for two different powers and the two assumed excitations. The effective excitation is more consistent with experimental data. This indicates

that the heat transfer processes in SBDs are dependent on their filamentary nature. In the rest of this work, the predictions of the model refer exclusively to the effective excitation case.

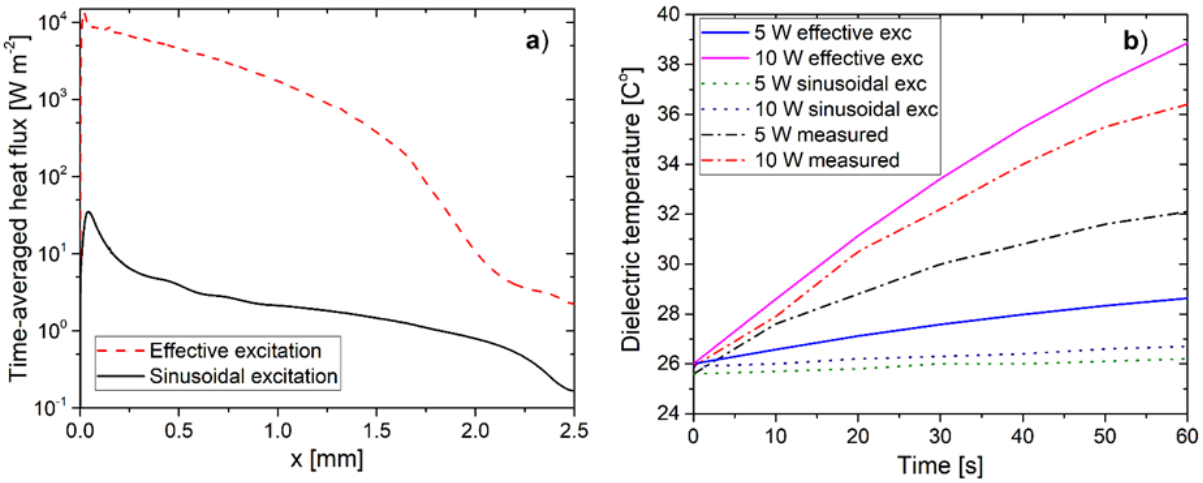

Figure 5.4: a) the time-averaged heat fluxes to the dielectric surface for the sinusoidal and the effective waveforms, b) A comparison of the average temperature of the dielectric between measured values and those calculated by the model.

Comparing the model's results to experimental measurements, Figure 5.4 panel b), shows there is a close agreement between them, with better consistency in the 10 W case. At an operating power of 5 W, the model underestimates the dielectric temperature. Critically, under such conditions the discharge appeared spatially uniform to the naked eye; however, at such low operating powers, previous ICCD imaging has shown that the discharge is likely to be non-uniform across the powered electrode, which will undoubtedly affect the dielectric heating within the experiment and thus explain the discrepancy with the model result.

Figure 5.4 panel b) also shows that at approximately 60 seconds, the temperature increases slowly in comparison to the first 10 seconds. This occurs as the dielectric gets closer to thermal equilibrium with its surroundings.

5.3.3 *Dominant heating mechanisms*

There are many possible mechanisms by which the plasma can heat the electrode and the background gas. In formulating the model, inelastic electron heating and ion flux heating were considered. The third mechanism, namely dielectric heating, was ruled out as the imaginary

permittivity of alumina is very low in the range of frequencies observed in SBDs (0-100 MHz) [22].

Electron heating of the background gas is one possible mechanism that occurs due to inelastic collisions between the electrons and N_2 & O_2 molecules, which leads to vibrational and rotational excitation of these molecules. It is assumed that all the electron energy lost in rotational and vibrational excitations ultimately results in a rise of transitional temperature in the background gas. This assumption is based on the fast quenching of vibrationally excited states at atmospheric pressure, which limits the number of molecules reaching the higher vibrational levels necessary for chemical reactions, which is applicable even at pressures as low as 100 Torr [165]. The second possible heating mechanism is the ionic flux to the dielectric surface. The propagation of a streamer is driven by the strong electric field at its head. When the streamer head propagates on a surface, as is the case in an SBD, the streamer head accelerates the ions and drives them to bombard the dielectric surface. To convert that energy into a heat flux. To investigate the contribution of each mechanism individually, the model was run with only electron heating, calculated by the heat equation. Then, the results were compared to the solution that included both mechanisms. Figure 5.5 shows the increase in the temperature after 60 seconds, where Figure 5.5 panel a) shows the electron heating contribution while Figure 5.5 panel b) shows the total contribution of both included heating mechanisms. Focusing on Figure 5.5 panel a), the strongest effect of electron heating by the plasma is observed at the tip of the electrode, where an increase of 15 °C is observed. This increase becomes significantly weaker further from the electrode, reaching almost ambient temperature approximately 1 mm downstream. This is attributed to the strong electric field at the edge of the electrode, which leads to high mean electron energy in that region. Considering that the flow velocity on the surface is zero due to friction, it becomes clear why the maximum temperature increase occurs on the surface. Moving further from the surface, convection driven by EHD forces causes gas cooling. It should be noted that EHD forces in an SBD cause the gas to flow in the direction of propagation of the streamers. In the SBD configuration considered in this investigation, the

streamers from two opposite electrodes meet in the centre of the gap where the discharge occurs. The flows induced by both streamers coalesce, forming a flow perpendicular to the dielectric surface as shown at x = 0 in Figure 5.5 [47].

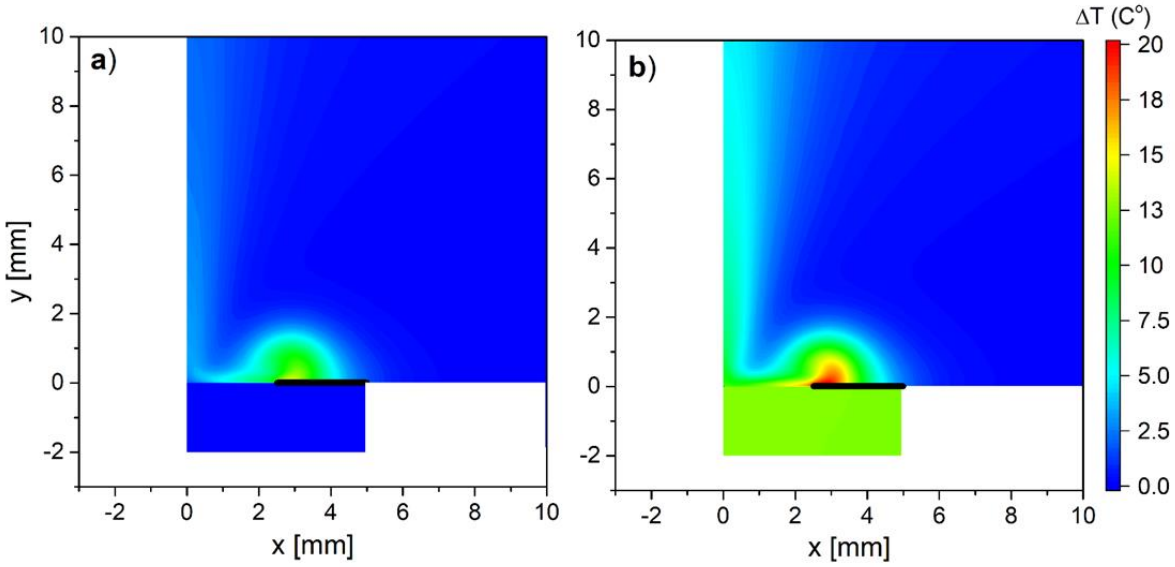

Figure 5.5: A 2D map of the increase in temperature after 60 s of discharge operation, calculated by the model for a power of 10W assuming a) electron heating only is calculated, and b) electron heating and ionic fluxes are calculated.

Figure 5.5 also shows that there is a plume of hot gas at x = 0, which coincides with the perpendicular flow described earlier. Its formation can be explained by the fact that the gas feeding into the perpendicular flow passes the electrode's edge and the dielectric surface, which, due to convective cooling, carries some of the heat away with it. This results in the perpendicular gas flow becoming hotter than the ambient flow, appearing as a plume at the boundary x = 0.

In terms of the heating of the dielectric and the subsequent induced perpendicular flow, electron heating plays a minimal role. This can be understood in terms of the difference in density between air (1.2 kg m^{-3}) and alumina (3.9×10^{3} kg m^{-3}). Considering that alumina's density is three orders of magnitude higher, a very large thermal flux is required to raise its temperature, which will require a very large difference in temperature between air and alumina.

When the ionic heat flux contribution was added, as shown in Figure 5.5 panel b), the temperature at the edge of the electrode increased by 5 °C in comparison to the case of electron heating only. This shows that the gas heating at the edge of the electrode is dominated by electron heating. Figure 5.5 panel b) also shows that the dielectric's temperature increased by 13 °C, indicating that the increase in the dielectric temperature is entirely due to ionic heat fluxes. The induced perpendicular flow at $x = 0$ has a temperature increase of 6 °C when the ionic flux is considered. Based on these results it can be concluded that the dominant heating mechanism of the perpendicular flow is convective heat transfer from the dielectric.

These findings have two important implications for the modelling of the chemical dynamics in an SBD. The first is related to the chemistry generated in the discharge. Considering that electron heating is dominant close to the edge of the electrode, where it has been reported that most of the chemical reactions of short-lived species occur [125], this region has the greatest impact on the discharge chemistry. As chemical reactions between the long-lived species predominantly occur in the perpendicular flow induced by the SBD [132], the dissipated power within the discharge affects the chemistry of the long-lived species indirectly through heating of the dielectric material, which in turn heats the resultant perpendicular gas flow.

Another heating mechanism that was considered but not included in the model was dielectric heating, where it is known that the imaginary part of the permittivity of most dielectrics has a peak in the GHz frequency range. This has the potential to correspond with the characteristic time of the ignition and propagation of streamers in SBD. For Al_2O_3, the dielectric response peaks at 10 GHz [166]. By performing a Fourier transform on the dissipated plasma power, a function representative of the power spectral density was computed and is shown in figure 5.6. The figure shows that a significant portion of the total power lies in the frequency spectrum below 60 MHz. This makes it unlikely that the power in the frequency range corresponding to the peak of the dielectric response is enough to cause any noticeable heating. In addition, the dielectric response of Al_2O_3 is known to be small [167]. Based on this analysis it is unlikely that dielectric heating would have a noticeable impact.

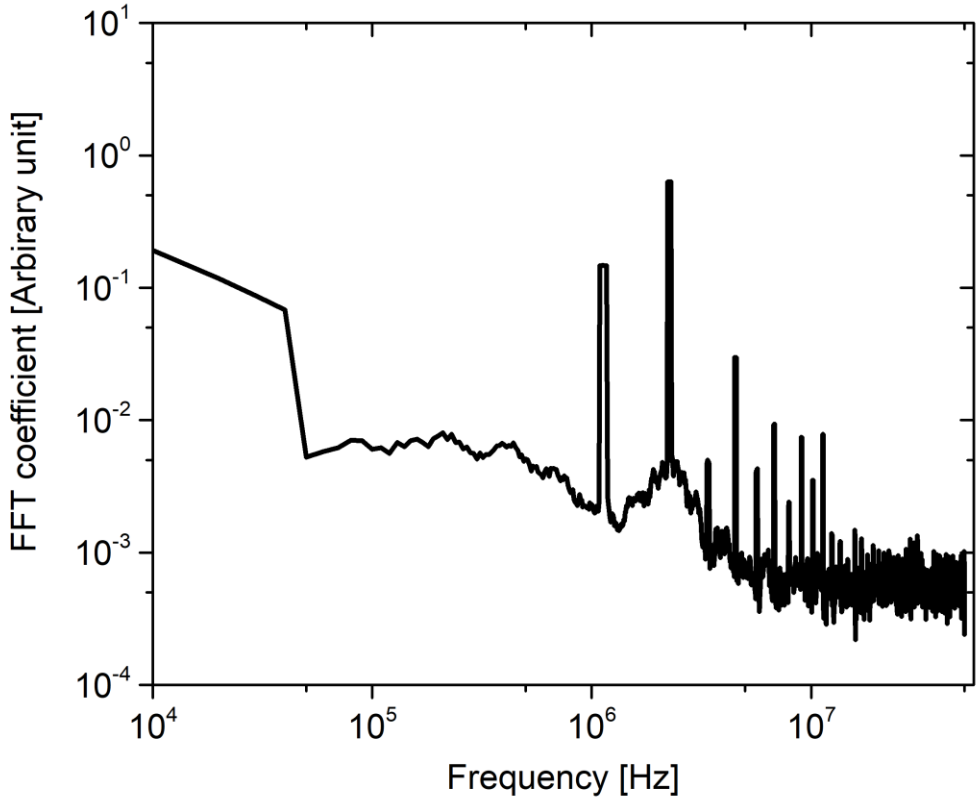

Figure 5.6: The Fourier transform coefficients for the discharge power waveforms shown in figure 5.2. This function is proportional to the power spectral density, which indicates the power distribution in the signal as a function of frequency.

5.3.4 *Impact on chemical kinetics*

To quantify the significance of accounting for the described heating mechanisms when modelling SBDs, Figure 5.7 shows the impact of each heating mechanism on the density of various reactive species. Figure 5.7 panel a) shows the two-dimensional density of O_3 for the 10 W case with the temperature distribution computed by the model. The O_3 concentration is highest at the electrode's edge where most of the short-lived species are generated as reported in [132] and where the velocity is close to zero due to the proximity of the dielectric surface and the electrode, which results in a longer residence time and thus a higher density.

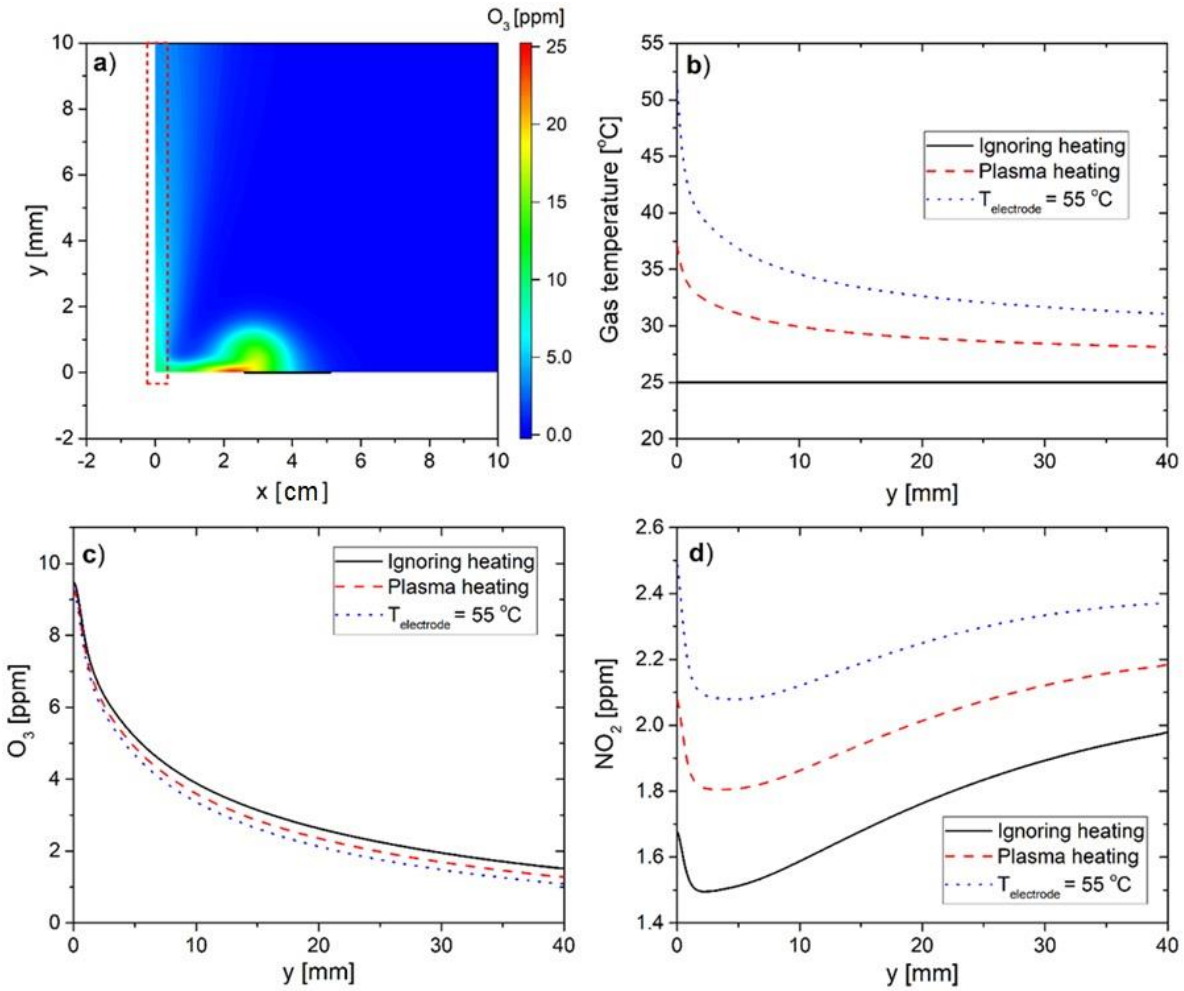

Figure 5.7: a) 2D map of the O_3 density in the discharge in parts per million; b) the gas temperature along the boundary shown in the red box in a) for the three test cases when ignoring plasma heating (black solid line), including plasma heating (red dashed line) and when only the heat from the electrode (blue dotted line); c) O_3 density along the boundary shown in a red box in a); d) A cut-NO_2 density along the same line. The densities of the species were calculated over the entire computational domain but shown here close to the electrode as that is the area of interest in the domain.

Further from the electrode, gas convection transports O_3 into the perpendicular flow, thus reducing its density on the dielectric surface. Figures 5.7 panels b) and c) show the densities of O_3 and NO_2 along the symmetry axis at x = 0, thus showing the densities as a function of distance from the surface of the dielectric. Both O_3 and NO_2 were specifically shown in Figure 5.7 panels b) and c) as they show the least and the most affected species respectively when the temperature is varied. All other species vary in that range. The reactive flow module was solved under a constant plasma power with three test cases in terms of temperature. The first case is assuming that the temperature everywhere in the domain is the room temperature (ignoring

heating completely). This is the approach taken by most SBD models. The second case assumed that the temperature at any point is computed by the model, which represents the self-consistent method for modelling the chemistry (the temperature distribution is shown in figure 5.5b). The third case sets the electrode temperature at 55 °C (30 °C above room temperature), allowing the heat to be convected to the gas. The assumption of this temperature is made to provide an upper limit analysis of the influence of temperature on the chemistry. Such temperatures have been recorded after minutes of SBD operation under high power conditions [168, 24].

Comparing the densities computed for the 3 cases, the difference that temperature alone makes can be observed. The difference in the density of O_3 among the 3 test cases is negligible. Conversely, NO_2 density shows a clear positive correlation with temperature. Therefore, a comprehensive treatment of plasma heating mechanisms noticeably increases the rate of NO_2 production due to the strong dependence of its dominant production mechanism on the temperature. In the simulated case, an increase of 20% is observed in NO_2 density along the perpendicular flow axis.

For the case where a temperature of 55 °C is assumed for the dielectric, the NO_2 density increases by a factor of 40% in comparison to that of having room temperature. Other species densities that are affected include NO, which increases by 14% for the plasma heating assumption and by 27% for the constant dielectric temperature assumption. N_2O also increases by 15% under the plasma heating assumption and by 27% for the constant dielectric temperature assumption. These results indicate that taking the discharge heating into account is of vital importance for the accurate modelling of the discharge chemistry in an SBD. It should be noted here that this reported increase becomes increasingly significant when the residence time is considered. Considering that both the simulation and experiments are done assuming the discharge operates in open air, this means the residence time of the gas in the discharge region is small. In closed systems, however, the residence time is much longer and thus the difference due to plasma heating will amplify significantly over time.

5.4 Conclusion

In this chapter, the model was experimentally validated and used to determine the underlying mechanisms responsible for heat transfer in an SBD. It was shown that many aspects of the filamentary nature of an SBD can be captured using a 2D model through the use of an effective pulsed waveform. The results showed that heating in an SBD occurs primarily due to the filamentary nature of the plasma, rather than being a result of a spatially averaged effect across the entire discharge length.

Three mechanisms of heating were considered: the electron heating of the background gas, ionic heat fluxes, and dielectric heating, where the time-dependent electric field in the streamer heads causes the dipoles in the dielectric to oscillate. The results of the model show that the increase in the dielectric temperature is almost entirely due to ionic fluxes bombarding it. It is also shown that 84% of the temperature increase in the perpendicular gas flow was a result of heat convection from the dielectric surface to the gas. Thus, ionic flux heating is the dominant heating mechanism downstream. Electron heating of the background gas accounted for approximately 75% of the temperature increase of the background gas close to the electrode, but the increases in temperature in the dielectric and the perpendicular flow induced by EHD forces were found to be insignificant. Dielectric heating was ruled out as a significant portion of the plasma power is in a frequency range where there is no overlap with the dielectric response of the dielectric material used.

The model was subsequently used to quantify the impact of accounting for gas heating mechanisms on the generation and loss of chemical species, where it was shown that reactive nitrogen species are strongly affected while reactive oxygen species are not. The species which had the largest variation included NO_2 which increased by a factor of 20 - 40%. Indicating that plasma heating must be considered to adequately describe the discharge chemistry.

6. Mutual interaction among multiple surface barrier discharges

In this chapter, the model was used to investigate how the electrode width of an SBD array affects the deposited power, the induced flow and the spatial distribution of the reactive species delivered to a downstream sample. The supporting experiment shown in this chapter was carried out by Dr. Aaron Dickenson, all other work presented is my own. The analysis presented in this chapter was published as a journal paper in Plasma Processes and Polymers.

6.1 Introduction and motivation

Considering that SBD arrays are the solution to maximising the dose of Reactive Oxygen and Nitrogen Species (RONS) species delivered to a downstream target and its uniformity, understanding the mutual interaction between adjacent SBD discharge gaps is of vital importance. The literature shows limited study of the interaction between adjacent discharge gaps in an SBD array. Some works have illustrated how discharge spacing affects the uniformity, but few have considered how other parameters, such as the variation of the deposited plasma power, the induced flow field, and the RONS density distribution are affected by discharge spacing. In this chapter, numerical modelling focused on emergent phenomena arising when multiple SBDs discharges are forced to interact by reducing the adjacent distance between them. Specifically, the model was used to identify the mechanisms by which discharge spacing affects the previously mentioned processes.

6.2 Methods

The details of the numerical model used to generate results in this chapter were given in chapter 3. They will be not repeated here. This section focuses on the experimental validation of the model. It should be noted here that while heat transfer was shown to be important in affecting the absolute densities of the reactive species generated in an SBD in chapter 5, the

focus of this chapter is the behaviour of the species rather than their absolute densities and therefore the heat transfer module was deactivated in this chapter.

6.2.1 *Input parameters to the model*

The geometry used in the model had 6 discharge gaps with widths of 1 mm each. Every 2 consecutive discharge gaps were separated by a 35 μm thick electrode with a variable width. The discharge gaps and electrodes were placed along the x-axis of the computational domain. The discharge operated at atmospheric pressure in air at room temperature, which was set as 298 K. The electrodes were driven with a sinusoidal applied voltage at a frequency of 22 kHz and an amplitude of 7 kV. The dielectric constant of the dielectric was set to 4.2 and its thickness was set to 1.5 mm. Considering that the calculation of the plasma variables required a very fine mesh, they were calculated over a single electrode and its adjacent gaps. The plasma solution was copied to the other electrodes to reduce computation time. For solving the reactive flow module, a coarser mesh was used, so the solution could be computed everywhere in the computational domain.

Two parametric studies were conducted, the first involved varying the electrode width with the values: 0.1 mm, 0.2 mm, 0.4 mm, 0.8 mm, and 1.6 mm. The study was run in a constant voltage mode, where the applied voltage was held constant. The 0.1 mm and 1.6 mm electrodes were also run in a constant power mode where the applied voltage was varied to maintain a constant deposited power to provide a means of comparison. The second parametric study was conducted by varying the distance to the downstream wall, mimicking the variation of the position of a sample to be treated downstream.

6.2.2 *Experimental setup*

To verify the output of the model, two SBD configurations with variable electrode widths were manufactured and used to quantify the influence of the resultant flow pattern using Particle Image Velocimetry (PIV). The two SBDs were constructed and operated in conditions as close as

possible to those modelled. Each SBD consisted of double-sided copper 1.5 mm thick FR-4 circuit boards, where five parallel strip electrodes of widths 0.4 and 1.6 mm were machined out of one side of each board while the other sides contained a large planar electrode. The frequency of the applied voltage matched that used in the model at 22 kHz.

The only deviation from the modelled conditions was the width of the gap which was set to 6 mm; this was required to overcome the spatial resolution limits associated with the PIV technique. This also meant that a lower amplitude of the waveform was required to deposit the same discharge power, which was 4.2 kV in the experiment giving a discharge power that is 5% different from that predicted in the model. Accordingly, a comparison between the modelled and experimental data provides a qualitative indication of the expected trends, rather than a robust validation. The strip electrodes were driven by a homemade high-voltage (HV) sinusoidal supply under the same conditions modelled while the planar electrodes were grounded, thus operating the discharge in a constant voltage mode. By design, plasma was only generated along the edges of the strip electrodes, over a length of 100 mm each.

PIV was performed to visualize and measure the flow pattern downstream of the plasma discharge area of each SBD. A chamber with dimensions of 1 x 1 x 1.5 m (width x height x length) was sealed and filled with vaporized olive oil droplets, which had a nominal diameter of 1 μm leading to a stokes number of less than 0.1, ensuring the droplets followed the fluid flow closely with tracing errors being <1% [169, 170]. The SBD was inserted & operated in the chamber and the velocity vector fields were recorded in a perpendicular plane to the electrodes, to show the flow from a similar angle as depicted in the model. The PIV system comprised of a Litron (LM2260) double-pulse Nd:YLF laser operating with a pulse duration of 100 ns at 527 nm. The time between adjacent pulses (ΔT) was set to 15 ms for both cases. A Phantom Micro 340 high-speed camera was used to capture a single laser pulse in each frame. A total of 600 frames were taken producing 300 vector maps, while only a fraction was required for comparison to the model.

6.3 Results & discussion

The analysis of the interaction between adjacent electrodes focused on three aspects, namely the power deposited in the discharge; the induced gas flow pattern and the delivery mechanism of reactive species to a treated surface downstream. For all investigated cases in this work, one plasma filament was ignited on every tip of the electrode, leading to two filaments per electrode, as shown in figure 6.1 panel a).

6.3.1 *Power deposition variation with electrode width*

As the width of the electrode is reduced, two effects could potentially occur. The first is an intensification of the electric field at the tips of the electrodes. This can be understood in terms of Gauss's law. The reduction of the electrode width means a reduction of the surface area of the electrode. Under constant voltage conditions, the same electric flux has to pass through a smaller surface, which leads to higher electric flux density and a stronger electric field. Essentially, the geometry of the electrode becomes more similar to a pin-like electrode instead of a plate-like electrode. This increase in the curvature leads to an increase in the electric field. The second effect is due to filament overlap. As the electrode width becomes small enough, the plasma filaments on the two electrode tips start to interact, filling the region on top of the electrode between them. This leads to an increase in the conductivity around the electrode resulting in a higher power deposition. To emphasise this effect figure 6.1 panel b) shows a cut line at a distance of 15 μm above the electrode for different electrodes width. As can be seen, a noticeable overlap is only observed for the 0.1 mm case.

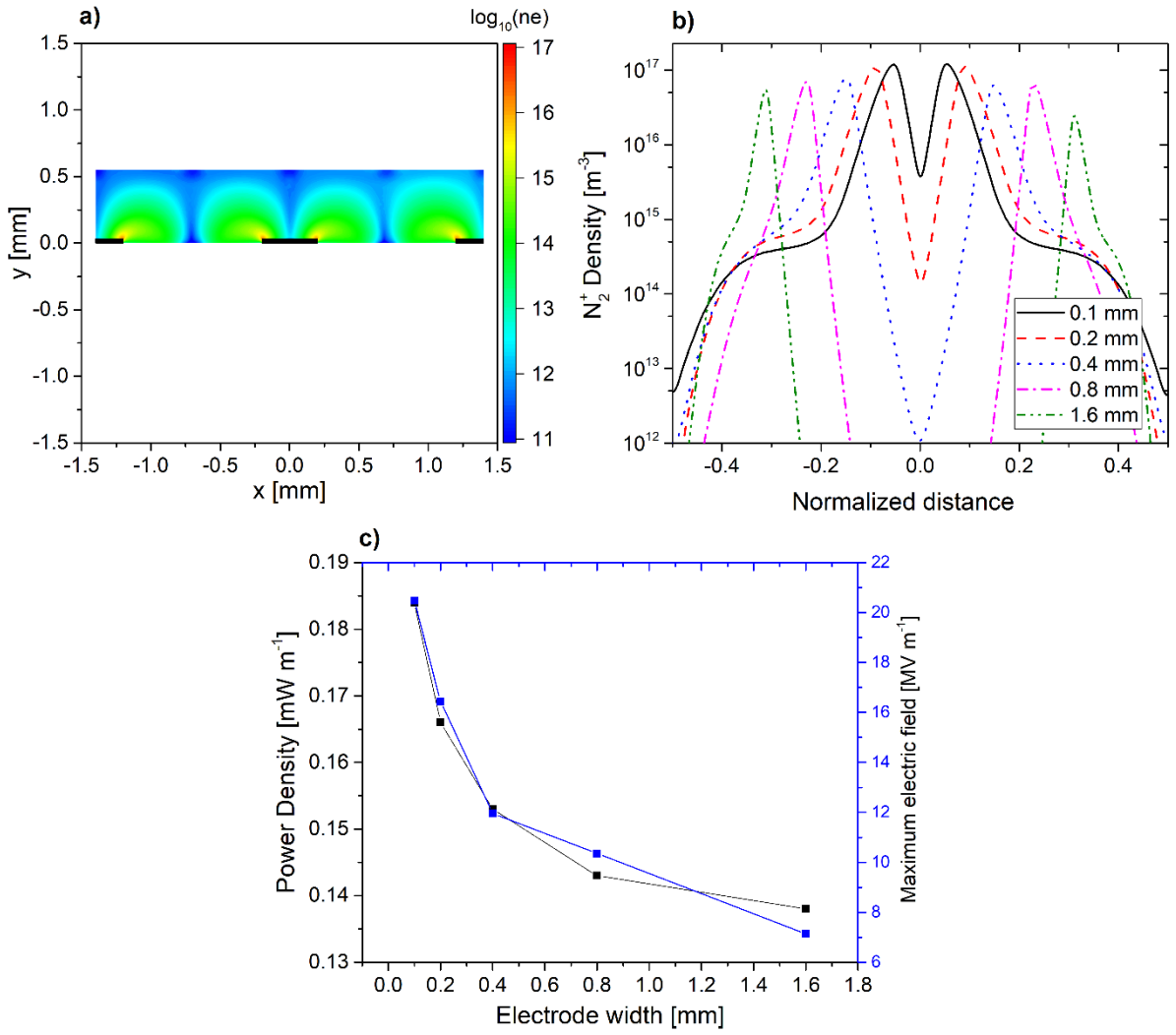

Figure 6.1: a) The 2D logarithm of the electron density for 0.4 mm electrode; b) N_2^+ density along a cut line 15 μm above the electrode, the x-axis is normalized to extend from the centre of the gap to the left and likewise from the centre of the gap to the right. All curves shown in the panel were taken at the same time; c) the variation of the plasma power density and the maximum electric field as functions of the width of the electrodes.

Figure 6.1 panel c) shows the plasma power density as a function of electrode width. As discussed earlier it was observed to increase when the electrode width decreased. To quantify the contribution of the two previously mentioned effects, the trend of plasma power variation was compared to the trend of maximum electric field variation. The maximum electric field was defined as the electric field at the tip of the electrode when the voltage was at its maximum.

Figure 6.1 panel c) shows that the trend is almost identical, therefore the increase in the deposited power is purely a geometrical effect.

These findings support those of a previous work of our group on discharge gap width [24], which showed that decreasing the electrode gap reduced the power deposition. Accordingly, the optimal design of an SBD in terms of power would include a modest discharge gap with a small width electrode, enabling the highest possible plasma power for a given voltage.

6.3.2 *Flow dynamics variation with electrode width*

It is well established experimentally that SBDs induce a background gas flow in the direction of the plasma filament. When two SBDs are separated by a discharge gap, the induced flow from both sides meet in the middle of the gap and coalesce to form a perpendicular flow, which creates a "jet" of reactive species and transports them to a downstream position [90]. When considering an SBD array, there is a possibility that the perpendicular flows emerging from every discharge gap will coalesce as the electrode width is reduced, subsequently leading to an enhancement of reactive species transport from the discharge.

Figure 6.2 shows the steady-state flow velocity for three different electrode widths. A common feature among all the cases shown is the presence of a localized perpendicular flow from each discharge gap. Moving downstream, it is apparent that the overall flow merges into a weak and wide perpendicular flow. To highlight this effect further, figure 6.2 panels b-f shows the y-component in the velocity field (perpendicular component) at different positions downstream. At a distance of 0.1 mm above the electrodes, the perpendicular velocity component shows an oscillatory behaviour, where velocity lobes alternating between the positive and negative directions are observed. This flow structure indicates the formation of stationary vortices at the electrodes' edges, where positive lobes represent the flow pushing towards the ambient air as the perpendicular jets emerge from the individual discharge gaps, while the negative lobes show the flow pulling ambient air into the discharge gaps. It should be noted that negative lobes

are centred on top of the electrodes, while positive lobes (perpendicular jets) are centred on top of the discharge gaps. At a distance of 0.5 mm downstream, the magnitude of the velocity is larger than that at 0.1 mm whether it is in the positive or the negative lobes. Considering that a boundary layer exists close to any surface, it is expected that the flow very close to a surface will be attenuated due to viscous damping. The flow at 0.1 mm is affected by the boundary layer while that at 0.5 mm is less affected, explaining the difference in magnitude between the two flows. Lastly, at a distance of 5 mm downstream, the individual jets emerging from the discharge gap coalesce into a wide positive lobe with relativity low velocity. This is due to the entrainment of the vertical jets into the ambient air, which causes them to widen and subsequently merge into a larger flow.

The influence of changing the width of the electrodes can be seen from the flows at 0.5 mm and 5 mm downstream. The magnitude of the velocity at all distances downstream is larger for the 0.1 mm electrode width, shown in figure 6.2 panel b), in comparison to that of the 0.4 and 1.6 mm electrode widths, shown in figures 6.2 panels d) and f) by factors of 33% to 200% respectively. This was attributed to a combination of the increase in the discharge power reported in figure 6.1 panel c) and the reduced geometry, which forced the vortices at the electrodes' edge to overlap.

The data shown in figure 6.2 was computed under the constant voltage mode of operation. Where the driven voltage was kept the same for all investigated cases. As was explained in section 6.3.1, decreasing the electrode width increased the discharge power for a constant voltage. To isolate the geometrical effect on the flow from the increase in power; a dataset similar to that shown in figure 6.2 was computed under a constant power mode for the two extreme cases in figure 6.4, namely the 0.1 mm and the 1.6 mm widths. Where the voltages applied to the electrodes were adjusted to maintain a constant discharge power density for both cases. The deviation of the discharge power between the two cases shown in figure 6.3 was less than 3%.

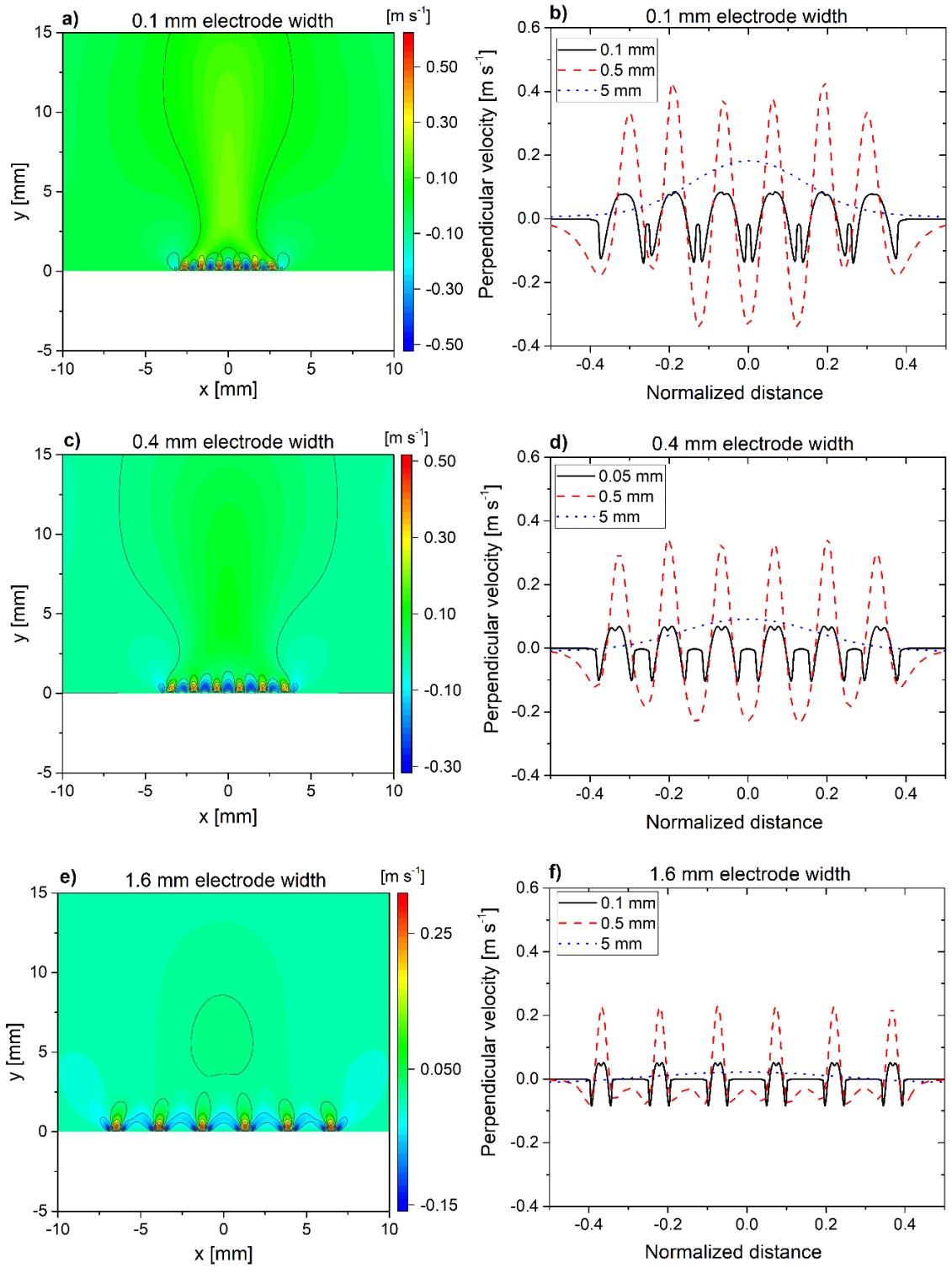

Figure 6.2: a) 2D Velocity Distribution for 0.1 mm electrode width; b) perpendicular velocity at a horizontal cutline at different distances downstream for 0.1 mm electrode width; c) 2D Velocity Distribution for 0.4 mm electrode width; d) perpendicular velocity at a horizontal cutline at different distances for 0.4 mm electrode width; e) 2D Velocity Distribution for 1.6 mm electrode width; f) perpendicular velocity at a horizontal cutline at different distances for 1.6 mm electrode width. Panels b, d, and f have identical scales, panels a, c, and e do not. This data was obtained using constant voltage mode.

It is evident from figure 6.3 that the flow structure is entirely due to the geometry while a significant contribution to the amplitude of the flow is determined by the discharge power. This is particularly evident from the small difference in the perpendicular velocity shown in figure 6.3 panels b-d when contrasted with figure 6.2 panels b-f.

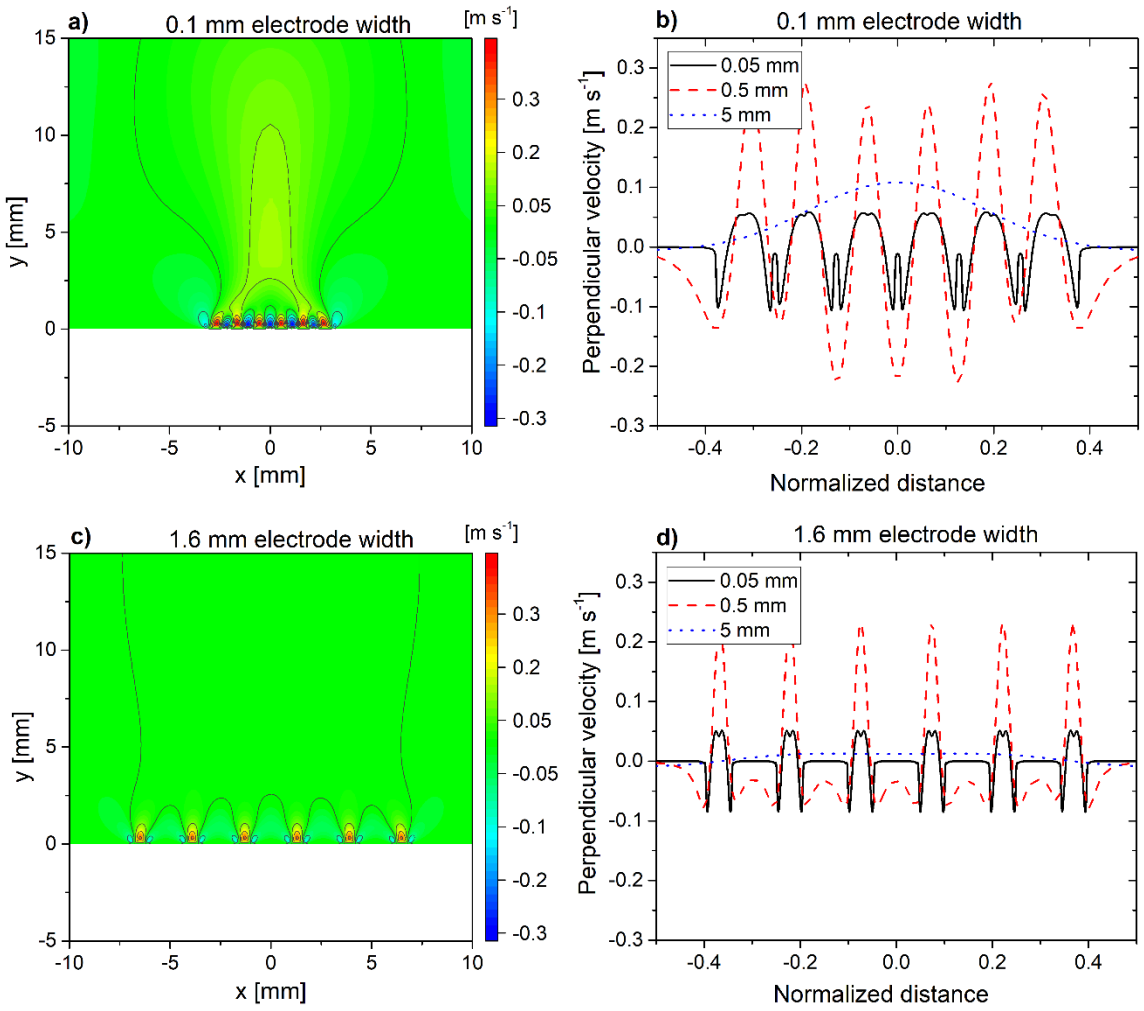

Figure 6.3: a) 2D Velocity Distribution for a 0.1 mm electrode width; b) the perpendicular velocity across a horizontal cutline at different distances downstream for a 0.1 mm electrode width; c) 2D Velocity Distribution for a 1.6 mm electrode width; d) the perpendicular velocity across a horizontal cutline at different distances downstream for a 1.6 mm electrode width. Panels a) and c) have the same legend. Panels b) and d) have the same axes. The data shown in this figure was obtained under constant power conditions, where the applied voltage was varied to maintain a constant power density across the cases shown.

Another noticeable difference in figure 6.3 is that the flow pattern for an electrode width of 1.6 mm seems identical for all gaps whether they are internal or external. While for the 0.1 mm electrode width, shown in figure 6.1 panel b), there is a clear difference between the magnitude

of the velocity on top of the internal discharge gaps and the external ones. The same effect can be observed in figure 6.2 as well, despite the difference in the discharge power. This indicates that for an electrode width of 1.6 mm the vortices at the electrode's edge no longer overlap and that the local flow at every discharge gap is independent of the adjacent gaps. While for electrode widths less than 0.4 mm, the overlap is evidently strong.

The consequences of this overlap in the flow on the functionality of the SBD as a source of reactive species are twofold. On one hand, decreasing the electrode width leads to a higher downstream velocity when the individual perpendicular jets merge, which is desirable as it accelerates the delivery of reactive species to a downstream target. On the other hand, the enhanced velocity in the negative lobes, as shown in figure 6.3 panel b), increases the chances of sucking the reactive species back into one of the discharge gaps, which is an undesired effect as it limits the delivery of reactive species to a downstream target. Critically, a competition arises between convection, which may assist or hinder the delivery of reactive species, and diffusion, which, by definition, is in the downstream direction. The interplay between these two mechanisms of delivery is explored in detail in section 6.3.4.

6.3.3 *Experimental observations*

To evaluate the predictions of the model experimentally, a set of PIV experiments were conducted, where the electrode width was varied and the measured flow velocity was recorded. Critically, preliminary experiments revealed that the flow generated by each SBD was unstable in time and no steady-state flow pattern could be observed. The difference between the model and experiments can be understood by considering the symmetry presented in the model which is not possible to obtain experimentally. Furthermore, the model assumed mirror geometry applies at the axis where x = 0 mm. the model also had a symmetric mesh covering every discharge gap and all computational meshes in the discharge gaps were identical. In that sense, there was no room for any random perturbation that might cause a deviation from the steady-state solution obtained when the model was solved. Experimentally, imperfections in the

fabrication of the electrodes or the dielectric surface are unavoidable and could lead the discharge to favour a certain point on one edge over another, causing an imbalance in the forces that cause asymmetric flow. Another factor that was not accounted for in the model but is inevitable in the real world was the presence of drafts and currents within the measurement chamber. These can be detected by the PIV system in the absence of plasma generation and would undoubtedly perturb the low-velocity flows downstream of the SBD electrode. Despite these differences, the findings of the model remain valid, with the observation merely implying that the findings of the model can be skewed in space and fluctuate over time.

Figure 6.4 shows the experimental velocity profiles at a constant applied voltage for electrode widths of 0.4 mm and 1.6 mm. The computational prediction of the flow-field for similar modelled cases is shown in figures 6.2 panels c) and d). There are several similarities between the model and experiment, including the presence of vortices at the electrodes' edges, and thus the presence of the positive and the negative velocity lobes downstream. Another aspect is the confirmation that the individual flows merge downstream to form a wide and weak jet, as is clearly shown in figure 6.4a). When the electrode width is varied from 0.4 mm to 1.6 mm, the variation in the downstream velocity is not significant, which is consistent with the model's prediction as shown in figure 6.2. A notable difference between the modelled and measured fields is that the amplitude of the velocity is higher in the measurement compared to that predicted by the model. This is a direct consequence of having a wider discharge gap, which led to a higher power deposition at the same operating voltage, causing higher flow velocities [24]. Another difference is that the vertical jets in the discharge gaps were tilted in comparison to the model. This was attributed to imperfections in the fabrication of the electrodes, which made the discharge more intense at some points in comparison to others.

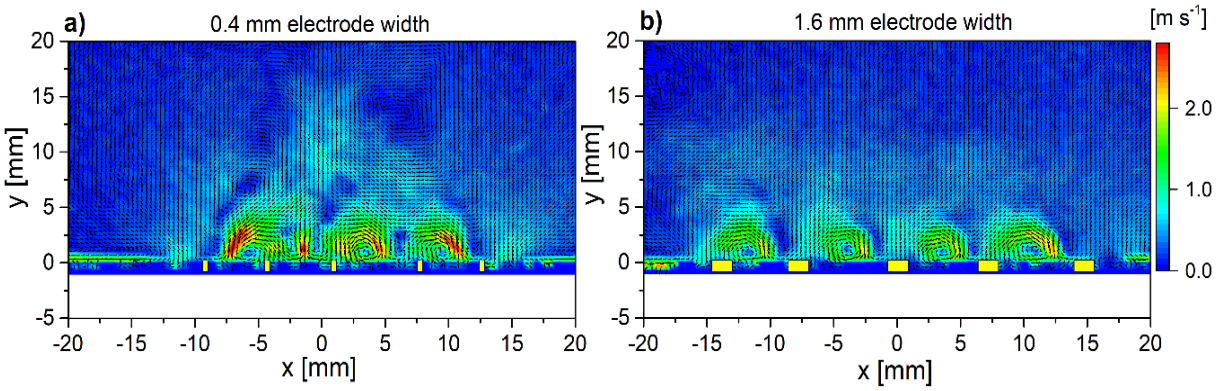

Figure 6.4: PIV measurements of the flow induced by adjacent discharge gaps in an SBD with electrode widths of a) 0.4 mm, and b) 1.6 mm electrode width. Data depicted in the figure are shown for a constant voltage mode. Both panels have the same colour legend. The yellow rectangles represent the approximate locations on the electrodes.

6.3.4 Transition between convection and diffusion dominated transport

Given that reducing the electrode width was shown to have a complex impact on the overall flow pattern, it is important to quantify the influence of the flow on the transport of reactive species. The chemical part of the model was solved for the two extreme cases of electrode width, namely the 0.1 mm case and the 1.6 mm. Figure 6.5 shows the 2D distribution of O_3 and NO_2, chosen as representative species of reactive oxygen and reactive nitrogen species respectively, for constant power mode at steady-state conditions.

From figure 6.5, it is clear that both species have a maximum at the surface of the electrode and spread as a cloud in the region separating the SBD from the downstream target (at y = 20 mm). Close to the target surface, the density of the species decreases to almost 0. This is a result of the outflow boundary condition in the model, which implies that any species arriving at the sample gets consumed by chemical reactions at the surface, making the boundary at y = 20 mm a sink for all species. Another common feature is the consistency of the distribution of the species with the background flow pattern shown in figure 6.3. This indicates that convection is still the dominant mechanism of transport close to the SBD despite its complex oscillatory behaviour. A noticeable difference in figure 6.5 is the densities for the 1.6 mm electrode width case are higher than those in the 0.1 mm case, despite having the same discharge power density. This can be explained by the difference in the downstream velocity in both cases, as shown by the blue

dotted curve in figure 6.3 b-d, where the downstream velocity for the 0.1 mm electrode width is higher than that of the 1.6 mm case. Considering that the generation rate of reactive species is the same in both cases due to the equal discharge power, a higher convection rate means less accumulation of the species at the electrodes and thus lower local densities.

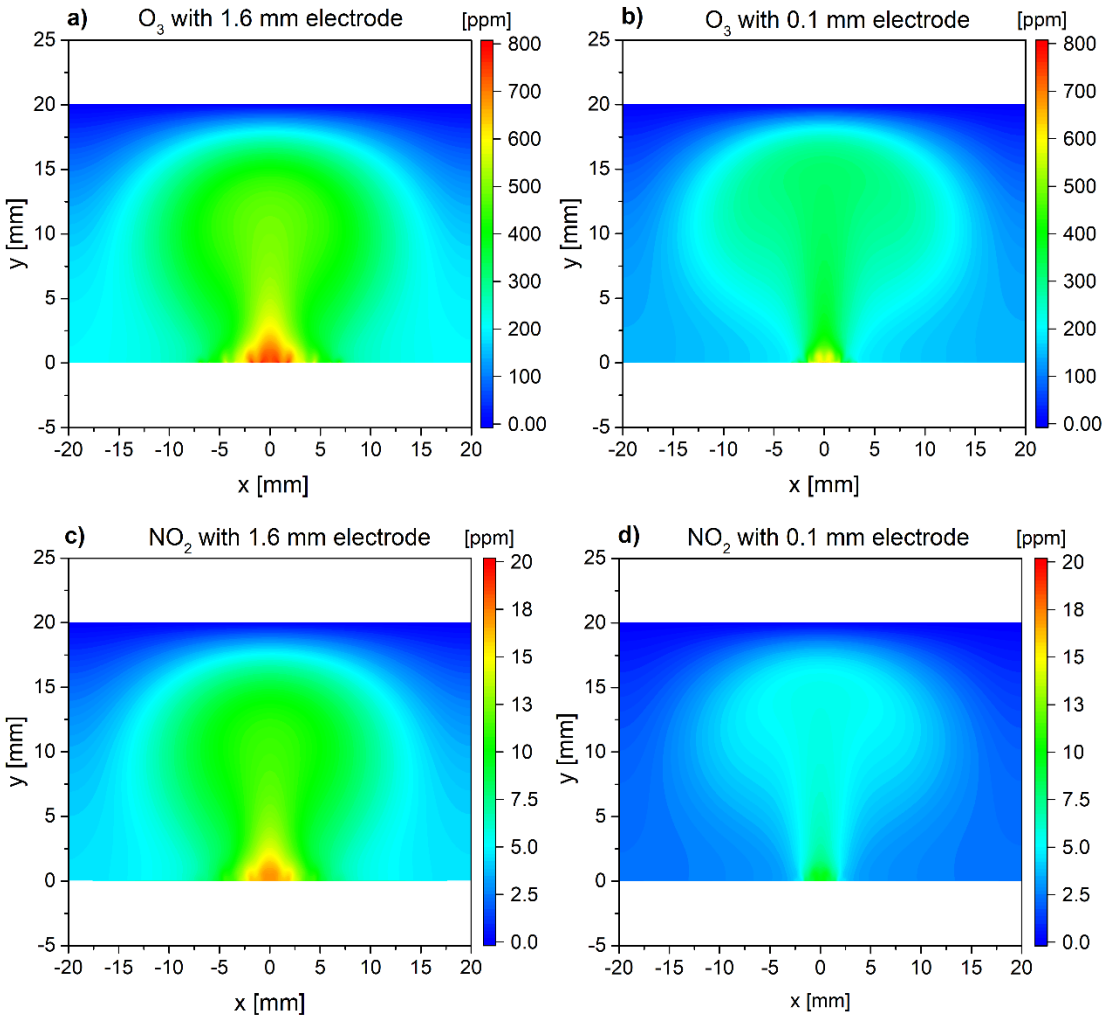

Figure 6.5: The 2D density at steady state for a) O_3 for 1.6 mm electrode width; b) O_3 for 0.1 mm electrode width; c) NO_2 for 1.6 mm electrode width; d) NO_2 for 0.1 mm electrode width. Panels a) and b) have the same legend. Panels c) and d) have the same legend. The data shown in this figure is obtained under constant power conditions, where the applied voltage is varied per case to maintain a constant power density across the cases shown.

While figure 6.5 shows that the density is higher for a 1.6 mm electrode width, the flux of reactive species delivered to the surface at the downstream boundary, shown in figure 6.6 panels a-b, shows the opposite. The figure shows the flux of O_3 for both electrode widths as a function of the location of the treated surface downstream. This is expected as the higher

convection in the 0.1 mm case removes O_3 at a faster rate from the domain to be consumed at the treated surface.

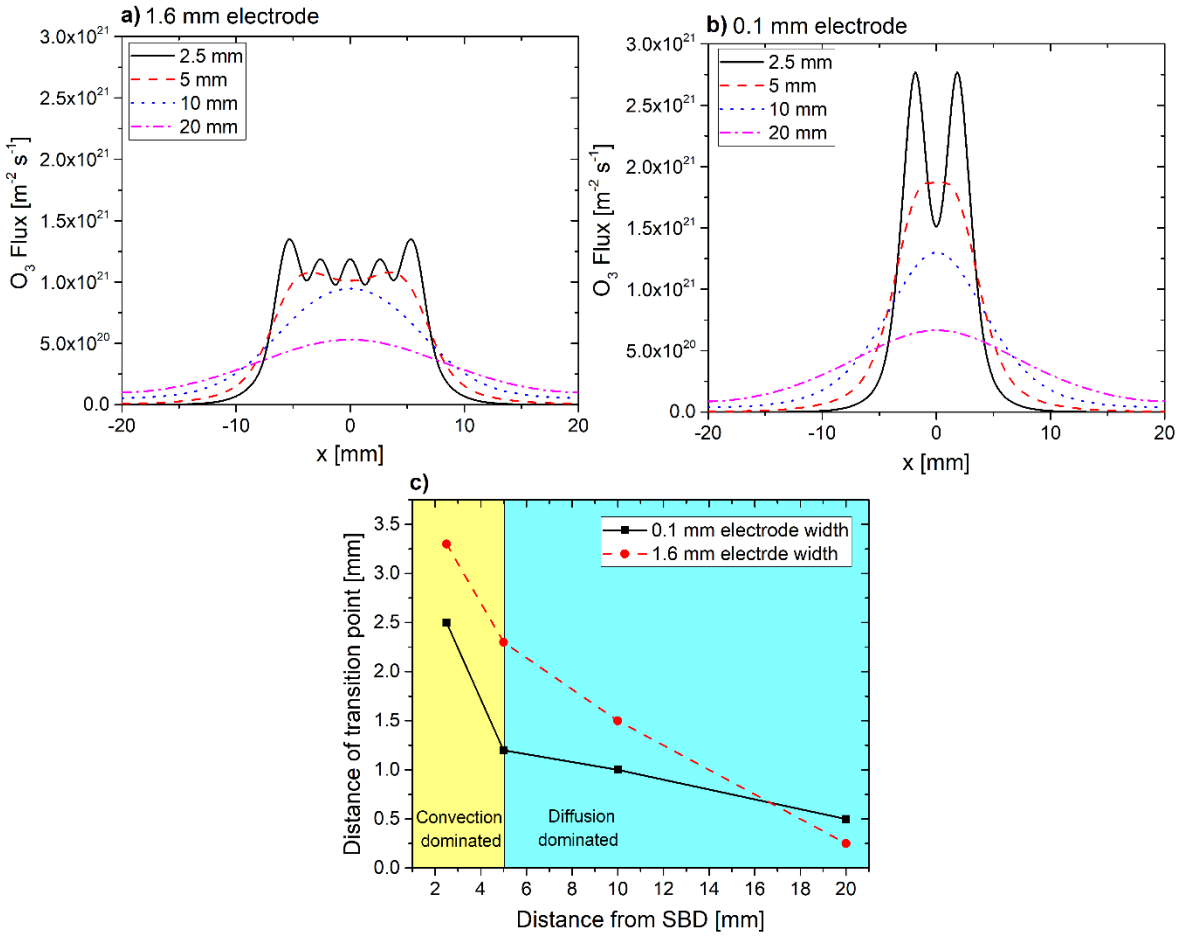

Figure 6.6: The time-averaged flux of O_3 delivered to the surface downstream for a) 1.6 mm electrode width; b) 0.1 mm electrode width. Both panels have the same axes; c) the position of the transition point from convection-dominated to diffusion-dominated transport with respect to the treated surface. The different curves in panels a) and b) correspond to different distances between the treated surface and the SBD. The time-averaging was done by integrating the arriving flux to the surface for 20 seconds, then dividing by that duration. The x-axis of panel c) shows the distance with respect to the surface of the SBD while the y-axis shows the distance with respect to the treated surface.

Moreover, figure 6.6 panels a-b show that when the distance between the treated surface downstream of the SBD is 20 mm, the delivered flux is relatively uniform irrespective of the electrode width. As the distance is decreased, the flux of the 0.1 mm electrode discharge mirrors the flow pattern and loses its uniformity. The maximum non-uniformity is found for a distance of 2.5 mm between the SBD and the target surface, where a 45% deviation from the maximum

flux is found for the 0.1 mm electrode case, and a 19% deviation is found for the 1.6 mm electrode case. This is counterintuitive as it is expected that a wide electrode will lead to a less uniform treatment as the discharge gaps are more widely spaced.

The variation in the flux as the distance between the target surface and the SBD was changed indicates a transition in the dominant transport mechanism. Beyond the discharge gap where charged species experience a significant electric field; both charged and neutral species can be transported either by convection or diffusion. Considering that the target surface served as a wall from a fluid mechanics perspective, where a no-slip boundary condition was imposed, it was expected that convection will be overtaken by diffusion at some point downstream. The distance from the target surface at which this transition occurred determined whether the flux was diffusion-dominated, resulting in a relatively low flux with a wide Gaussian profile, or if it was convection-dominated, resulting in a flux that depends on the flow velocity and a profile with ripples due to the flow lobes shown in figures 6.2 and 6.3.

To identify the transition point, the convective flux in the y-direction of O_3 was compared to the diffusive flux in the same direction at every point in the domain. The transition point was defined as the closest point to the target surface where the convective flux dominated over the diffusive flux. The distance between that point and the treated surface is plotted in figure 6.6 panel c) as a function of the distance between the SBD and the target surface. A change in the slope can be seen at a distance of 5 mm between the SBD and the treated surface. This change in the slope indicates the transition between convection-dominated flux and diffusion-dominated flux. This is consistent with the disappearance of the ripples from the delivered flux profiles shown in figure 6.6 panels a-b) when the distance is increased.

The transition of the dominant transport mechanism can also be used to explain why the flux is less uniform for the 0.1 mm electrode in comparison to the 1.6 mm electrode, despite the larger distances between the discharge gaps in the latter case. At a distance of 2.5 mm, convection dominated the transport, since it was shown in section 6.3.2 that the flow velocity is higher for

the 0.1 mm electrode case in comparison to the 1.6 mm electrode case, meaning that diffusion had less time to affect the distribution of the species. Considering that diffusion is a process that "smooths" density gradients, a shorter transport time between the SBD and the target surface meant less uniformity. This also explained why the transition curve of the 0.1 mm electrode case, shown in figure 6.6 panel c), is below that of the 1.6 mm electrode case.

In summary, reducing the gap between the SBD and a target surface resulted in a higher flux in a similar period of time at the expense of the uniformity of the flux. The uniformity of the flux could be improved by increasing the electrode width. A trade-off must be made between the electrode width and the distance to the target in order to simultaneously maximise the flux and its uniformity.

6.4 Conclusion

In this chapter, the effect of electrode width in an SBD array on the discharge performance as a source of reactive species was investigated. The investigation focused on three aspects: the discharge power, the induced flow, and the rate of transport of reactive species to a downstream target surface. An experimentally validated model was adapted to describe an SBD array consisting of 6 discharge gaps. The findings of the model were supported by experimental measurements of the induced flow velocity obtained using Particle Image Velocimetry.

It was shown that an increase in the electrode width led to lower discharge power for the same applied voltage, with the decrease in power being exponential. This was explained by the influence of the geometry on the electric field driving the discharge, where a wider electrode resulted in a lower electric flux density, and consequently a weaker electric field. Accordingly, it is desirable to design an SBD with a smaller electrode width and thus obtain a higher discharge power at a given voltage.

With respect to the induced flow pattern, it was shown that the spatial dependence of the flow is determined entirely by the geometry of the SBD array, while the amplitude is determined by a

combination of the discharge power and its geometry. In addition, it was shown that static vortices arise at the edges of electrodes surrounding the inner discharge gaps. As the electrode width was reduced, the vortices started to overlap; resulting in an oscillatory flow that manifested in the appearance of positive velocity lobes, which drive the flow from the discharge gaps downstream, and negative lobes, which drive the flow from downstream into the discharge gap. The lobes were observed to merge into one large positive lobe downstream, where the velocity of the lobe increased when the electrode width was decreased at a given discharge power.

Finally, the influence of increasing the electrode width on the delivery of reactive species to a downstream target surface was investigated. It was found that the dominant mechanism of transport in the gap between the SBD array and the target surface was dependent on the distance between them. For short distances, the flux arriving at the surface was convection dominated, resulting in a higher flux with a non-uniform profile. For large distances, diffusion was found to dominate, resulting in lower fluxes with a Gaussian-like profile, providing better uniformity compared to shorter distances. It was shown that increasing the electrode width improved the uniformity on the target surface, at the expense of the flux magnitude. This suggests a trade-off is required to simultaneously obtain the highest flux and the maximum uniformity. Critically, the findings of this work provide guidance to better control the uniformity and efficiency of SBD arrays through manipulation of the array geometry.

7. Conclusions and further research

7.1 Conclusions

The work presented in this thesis focused on modelling surface barrier discharges in ambient air, with a focus on providing a set of recommendations based on performance when designing an SBD for a real-world application. Starting from a two-dimensional fluid model, which consisted of a plasma module, chemistry module and reactive flow module, the model was upgraded and used to investigate multiple practical considerations of SBD operation, namely, the impact of humidity of air on the generated species; the impact of the plasma on the temperature of the dielectric and the gas and how that impacts the generated species, and finally the impact of having multiple closely-spaced SBDs (SBD array) on the fluxes of species delivered to a downstream sample.

Using the baseline model to investigate how humidity level impacts species production, a positive correlation was reported between the humidity value and the density of HNO_x species produced, with the increase rate slowing as the humidity level was increased. OH density was seen to rapidly increase at low humidity but the rate of increase tapered at higher humidity. This is believed to be due to H_2O acting as a 'trace' species at low humidity but at higher values the electronegative quality of H_2O affected the evolution of the discharge Meanwhile, a slight decrease in NO_x species was observed. Hydrogen-free species showed only marginal density changes, most decreasing due to more of their parent species being used in hydrogen-involving reactions. However, atomic oxygen density increased slightly, due to electron impact dissociation of H_2O. This showed that humidity level is a vital factor of consideration when HNO_x species are of interest.

The baseline model was upgraded by coupling the heat equation to its modules. The results of the upgraded model were compared to the experiment and found to be in good agreement. Three potential mechanisms of heat transfer were then compared to identify the dominant

mechanism, namely dielectric heating, electron heating through inelastic losses, and heating via ionic fluxes to the dielectric. Dielectric heating (via orientation alignment of molecules in the dielectric surface) was found to have no significant impact as the power of the discharge is concentrated in a region of the frequency spectra where the imaginary part of the dielectric constant of alumina is negligible. Electron heating through inelastic collisions of electrons with gas molecules was found to have a small effect but heating by ionic fluxes to the dielectric surface was found to be the primary heating mechanism, contributing almost all of the 13 K temperature increase seen in the gas flow. More specifically, electron heating produced 75% of the heating of the background gas, but ion collisions produced 84% of the heating of the perpendicular gas flow, which is the more important consideration in most applications. The increase in temperature of the dielectric surface is then convected through the gas.

The implementation of the heat transfer model also resulted in an improvement to the methodology of modelling SBD, through the introduction of an effective applied voltage waveform. In experiments, a sinusoidal applied waveform was used to drive the discharge. However, due to the filamentary nature of a discharge, the deposited discharge power as a function of time consisted of Gaussian-like short spikes instead of having a smooth power deposition waveform. To mimic this behaviour, an effective waveform was introduced and altered to maximise the resemblance between the deposited power computed by the model and the power spikes observed in experiments. Using the effective waveform, it was possible to partially capture the filamentary nature of the discharge which enabled the model results to follow experimental observation closely.

The investigation of the effect of temperature variation on the gas chemistry found that models which use a fixed electrode temperature tend to underestimate the NO_2 production, possibly due to more reactions occurring close to the electrode if it becomes the hottest region. This under-estimation is $\sim$ 20% of the production of NO_2, showing that accurate modelling of SBD chemistry requires heat transfer to be taken into account.

The model has also been upgraded to capture the effects of mutual interactions between adjacent SBD gaps. It is commonly assumed that the behaviour of a single discharge gap can be extended to represent an entire SBD array (i.e. non-overlapping discharges can be considered entirely independent of each other). By modelling 6 discharges laterally adjacent to each other the limitations of this assumption were shown. It was reported that vortices develop at the edge of each discharge's induced flow pattern, which began to overlap when the discharge separation is small enough, resulting in positive and negative lobes in the flow velocity, driving species downstream or back towards the electrodes where they may be reprocessed by the discharge. The interaction between the discharge gaps predicted by the model was validated by an equivalent experiment where Particle Image Velocimetry showed similar particle velocity values. These findings showed that decreasing the distance between an SBD and a sample downstream makes the discharge operate in a convection-dominated regime which on one hand increases the flux, but on the other hand, reduces the uniformity of the flux due to the presence of velocity lobes, thus a compromise needs to be made between maximising the flux and maintaining its uniformity.

The impact of reducing the distance between adjacent discharge gaps was also analysed from a power deposition perspective. It was shown that increasing the electrode width exponentially decreased the power deposition, which could be understood as a wider electrode producing a lower electric flux density and thus a weaker field. As a result, it is recommended that using smaller electrodes can be a simple way to produce higher power deposition.

7.2 Further research

The first recommendation to come out of the work presented in this thesis is that all of the above improvements to fluid SBD models should be incorporated into future models to maximise their generality. The effective pulsed waveform is substantially more suitable for capturing phenomena dependent on the filamentary nature of the discharge. Heat transfer was

shown to make a substantial difference to species density values. None of these improvements substantially increased computing time or affected model stability.

It is likely that further research into the impact of heat transfer and temperature change would be fruitful. The resulting temperature increases produced under different operating conditions should be quantified. For example: how does the temperature increase depend on the applied voltage or the initial ambient temperature? It would be interesting to see whether the dominant heating mechanism would be different if the dielectric constant of the dielectric surface or the thermal conductivity of the gas were different. Geometric considerations should also be made: would a smaller electrode or a narrower dielectric surface result in less ion-flux heating?

Another important recommendation is that neighbouring discharges should only be considered independent if they have a large gap between them, otherwise models must account for their interaction. Further investigation into this interaction is still required. One line of inquiry is whether species produced in the discharge which are 'recirculated' and re-enter the discharge result in different species being produced. Many models do not calculate a long enough discharge period for recirculated species to enter but they would likely result in different chemical reactions and therefore different species being produced. This may see discharge chemistry change over time. The model of neighbouring discharges used here considered discharges separated only in one dimension. In many SBD arrays, however, discharges are produced on a two-dimensional grid. This may produce different and more complicated induced flow patterns. It is important these flow patterns are understood to fully understand how reactive species are transported to a downstream target.

References

[1] Kostov, K. G. et. al. (2010) *Bacterial sterilization by a dielectric barrier discharge (DBD) in air.* Surface and Coatings Technology, v 204, n 18-19, 2954-2959.

[2] Choi, J. H. et. al. (2006) *Analysis of sterilization effect by pulsed dielectric barrier discharge*. Journal of Electrostatics, v 64, n 1, 17-22.

[3] Langmuir, I. (1927) *Flames of Atomic Hydrogen.* Ind. Eng. Chem. 19, 6, 667-674.

[4] Chen, F. (2016) *Introduction to Plasma Physics and Controlled Fusion.* 3rd ed. Springer, Chapters 3 & 5.

[5] Mason, E. A. McDaniel, E. W. (1988) *Transport Properties of Ions in Gases*. 1st ed. Wiley.

[6] Fan, Z. et. Al. (2019) *A Surface Dielectric Barrier Discharge Plasma for Preparing Cotton-Fabric-Supported Silver Nanoparticles.* Nanomaterials 9, 7, 961.

[7] Karimzadeh, A. (2019) A review of electrodeposited Ni-Co alloy and composite coatings: Microstructure, properties and application. Surface and Coatings Technology, 372, 25, 463-498.

[8] Ganesan, A. R. (2020) *Application of cold plasma on food matrices: A review on current and future prospects.* Journal of Food Processing and Preservation, 45, 15070.

[9] Zhou, R. (2020) *Plasma-activated water: generation, origin of reactive species and biological applications.* J. Phys. D: Appl. Phys. 53, 303001.

[10] Itoh, H. (2006) *Discharge plasmas generated by piezoelectric transformers and their applications.* Plasma Sources Sci. Technol. 15, S51.

[11] Raizer, Y. P. (1991) Gas Discharge Physics. Springer-Verlag, Ch 7.

[12] Keidar, M. Yan, D. Sherman, J. H. (2019) *Cold Plasma Cancer Therapy.* IOP Concise Physics.

[13] Kuzminova, A. et. al. (2017). *Etching of polymers, proteins and bacterial spores by atmospheric pressure DBD plasma in air*. Journal of Physics D: Applied Physics. 50, 135201.

[14] Brandenburg, R. (2017) *Dielectric barrier discharges: progress on plasma sources and on the understanding of regimes and single filaments*. Plasma Sources Sci. Technol. 26 053001.

[15] Moreau, E. et. al. (2008) *Electric wind produced by surface plasma actuators: a new dielectric barrier discharge based on a three-electrode geometry*. Journal of Physics D: Applied Physics, v41, 11.

[16] Fridman, A. (2008) *Plasma Chemistry.* Cambridge University Press, Chapters 1 & 4.

[17] Fatemeh Rezaei, F. Vanraes, P. Nikiforov, A. Morent, R. De Geyter, N. (2019) *Applications of Plasma-Liquid Systems: A Review.* Materials, 12, 2751.

[18] Hamilton, J. A. (1980) *Ratio of sheath thickness to Debye length for a slightly ionized continuum plasma.* Australian Journal of Physics, 33, 39-45.

[19] Lieberman, M. A. Lichtenberg, J. A. (2005) *Principles of Plasma Discharges and Materials Processing, Second Edition.* Wiley & Sons. Print ISBN:9780471720010 |Online ISBN:9780471724254 |DOI:10.1002/0471724254.

[20] SIGLO database, www.lxcat.net, retrieved December 7, 2021.

[21] Townsend, J. S. (1910) *The theory of ionization of gases by collision.* Constable, Limited, 1910.

[22] Tabib-Azar, M. Pai, P. (2017) *Microplasma Field Effects Transistors*. Micromachines, 8(4), 117.

[23] Nudnova, M. M. et. al. (2015) *Fast gas heating in N2/O2 mixtures under nanosecond surface dielectric barrier discharge: the effects of gas pressure and composition.* Phil. Trans. R. Soc. A 373: 20140330.

[24] Tirumula, R. et. al. (2014) *Temperature characterization of dielectric barrier discharge actuators: influence of electrical and geometric parameters.* J. Phys. D: Appl. Phys. 47 255203.

[25] Jorgenson, R. E. Warne, (2003) L. K. Effect of Dielectric Photoemission on Surface Breakdown: An LDRD Report. Sandia National Laboratories, SAND2003-1731.

[26] Erfani, R. (2012) *Thermal Characterization of a DBD Plasma Actuator: Dielectric Temperature Measurements Using Infrared Thermography*. Experimental Thermal and Fluid Science 42 258–264.

[27] Zhang, S. et. al. (2019) *Numerical investigation on the effects of discharge conditions on a nanosecond pulsed surface dielectric barrier discharge.* J. Appl. Phys. 125, 113301.

[28] Chvyreva, A. Pancheshnyi, S. Christen, T. Pemen, A. J. M. (2018) *Raether–Meek criterion for prediction of electrodeless discharge inception on a dielectric surface in different gases.* Journal of Physics D: Applied Physics, 115202.

[29] Staack, D. Farouk, B. Gutsol, A. Fridman, A. (2005) *Characterization of a dc atmospheric pressure normal glow discharge*. Plasma Sources Sci. Technol. 14, 700–711.

[30] Tao, X. et. Al. (2011) *CH4–CO2 reforming by plasma – challenges and opportunities*. Progress in Energy and Combustion Science, 37, 2, 113-124.

[31] Zhao, X. Becerra, M. Yang, Y. et. al. (2021) *Elongation and branching of stem channels produced by positive streamers in long air gaps*. Sci. Rep. 11, 4120.

[32] Lu, XP. et. al. (2008) *An 11cm long atmospheric pressure cold plasma plume for applications of plasma medicine.* Appl. Phys. Lett. 92, 081502.

[33] Chang, Z-S. et. al. (2012) *Diagnosis of gas temperature, electron temperature, and electron density in helium atmospheric pressure plasma jet.* Physics of Plasmas 19, 073513.

[34] Kim, S. J. Chung, T. H. (2016) *Cold atmospheric plasma jet-generated RONS and their selective effects on normal and carcinoma cells.* Scientific Reports, 6, 20332.

[35] M Ghasemi et. al. (2013) *Interaction of multiple plasma plumes in an atmospheric pressure plasma jet array.* J. Phys. D: Appl. Phys. 46, 052001.

[36] Morabit, Y. Hasan, M.I. Whalley, R.D. et. al. (2021) *A review of the gas and liquid phase interactions in low-temperature plasma jets used for biomedical applications*. Eur. Phys. J. D 75, 32.

[37] Nam Kim, K. Min Lee, S. Mishra, A. Young Yeom, G. (2016) *Atmospheric pressure plasmas for surface modification of flexible and printed electronic devices: A review.* Thin Solid Films, 598, 315-334.

[38] Wollny, A. (2011) *Ignition of a Microcavity Plasma Array*. IEEE Transaction on Plasma Science. 39, 11.

[39] Wang, J. -J. et. al. (2013) Recent developments in DBD plasma flow control Prog. Aerosp. Sci. 62, 52.

[40] Liu, Z. C. et. al. (2015) *Physicochemical processes in the indirect interaction between surface air plasma and deionized water.* J. Phys. D: Appl. Phys. 48, 495201.

[41] Guo, Li. et. al. (2018) *Mechanism of Virus Inactivation by Cold Atmospheric-Pressure Plasma and Plasma-Activated Water.* Applied and Environmental Microbiology, 84, 17:AEM.00726-18.

[42] Černáková, L'. Kovacik, D. (2005) *Surface Modification of Polypropylene Non-Woven Fabrics by Atmospheric-Pressure Plasma Activation Followed by Acrylic Acid Grafting.* Plasma Chemistry and Plasma Processing 25, 4, 427-437.

[43] Choudhury, B. et. al. (2018) *Inactivation of Pseudomonas aeruginosa and Methicillin-resistant Staphylococcus aureus in an open water system with ozone generated by a compact, atmospheric DBD plasma reactor.* Scientific Reports, 8, 1.

[44] Slavicek, P. et. al. (2005) *Diagnostics of RF unipolar barrier discharge generated by plasma pencil at atmospheric pressure.* 16th Symposium on Physics of Switching Arc, 8021429313.

[45] Baeva, M. (2001) *Pulsed microwave discharge at atmospheric pressure for NOx decomposition.* Plasma Sources Science and Technology, 11, 1, 1.

[46] Bolotov, O. (2018) *The spatio-temporal structure of radiation from the negative corona discharge at the trichel pulsed mode for the "needle-plane" electrode system.* Problems of Atomic Science and Technology 115, 3, 101-104.

[47] Maiolo, L. et. al. (2006) *Low-temperature electron cyclotron resonance plasma-enhanced chemical-vapor deposition silicon dioxide as gate insulator for polycrystalline silicon thin-film transistors.* Journal of Vacuum Science & Technology A, 24, 280.

[48] Kogelschatz, U. (2007) *Dielectric-Barrier Discharges. Principles and Applications.* Journal de Physique IV Proceedings, EDP Sciences, 1997, 07 (C4), pp.C4-47-C4-66.

[49] Gibalov, V. I. Pietsch, G. J. (2000) *The development of dielectric barrier discharges in gas gaps and on surfaces*. J. Phys. D: Appl. Phys. 33, 2618.

[50] Eliasson, B. Kogelschatz, U. (1991) M*odeling and applications of silent discharge plasmas.* IEEE Transactions on Plasma Science, 19, 2.

[51] Corke, T. C. et. al. (2010) Dielectric Barrier Discharge Plasma Actuators for Flow Control. Annual Review of Fluid Mechanics, 42, 505-529.

[52] Shimizu, T. et. al. (2017) *Surface Microdischarge Plasma for Disinfection.* Plasma Medicine, 7, 2, 175-185.

[53] Shimizu, T. et. al. (2011) *The bactericidal effect of surface micro-discharge plasma under different ambient conditions.* New J. Phys. 13, 023026.

[54] Verboncoeur, J. P. (2005) *Particle simulation of plasmas: review and advances.* Plasma Phys. Control. Fusion 47, A231.

[55] Watnick, P. Kolter, R. (200) *Biofilm, City of Microbes.* Journal of Bacteriology, 182, 10, 2675-79.

[56] Gumbiner, B. M. (1996) *Cell Adhesion: The Molecular Basis of Tissue Architecture and Morphogenesis.* Cell, 84, 3, 345-357.

[57] Ciofu, O. Tolker-Nielsen, T .(2019). *Tolerance and Resistance of Pseudomonas aeruginosa Biofilms to Antimicrobial Agents-How P. aeruginosa Can Escape Antibiotics.* Frontiers in Microbiology. 10: 913.

[58] Maisch, T. et. al. (2012) *Contact-Free Inactivation of Candida albicans Biofilms by Cold Atmospheric Air Plasma.* Applied and Environmental Microbiology, 78, 12.

[59] Matthes, R. et. al. (2013) *Antimicrobial Efficacy of Two Surface Barrier Discharges with Air Plasma against In Vitro Biofilms.* PLoS ONE 8, 7, e70462.

[60] Salgado, B. A. B. et. al. (2013) *Surface barrier discharges for Escherichia coli biofilm inactivation: Modes of action and the importance of UV radiation.* PLoS ONE 16, 3, e0247589.

[61] Gavahian, M. Khaneghah. A. M. (2019) *Cold plasma as a tool for the elimination of food contaminants: Recent advances and future trends*. Critical Reviews in Food Science & Nutrition, 59, 10.

[62] Rana, S. et. al. (2020) *Atmospheric cold plasma (ACP) treatment improved in-package shelf-life of strawberry fruit.* J. Food Sci. Technol. 57, 102–112.

[63] Misra, N. et. al. (2014) *In-package atmospheric pressure cold plasma treatment of cherry tomatoes.* Journal of Bioscience and Bioengineering, 118, 2, 177-182.

[64] Tappi, S. et. al. (2014) *Atmospheric gas plasma treatment of fresh-cut apples.* Innovative Food Science & Emerging Technologies, 21, 114-122.

[65] Xiang, Q. et. al. (2018) *Effects of dielectric barrier discharge plasma on the inactivation of Zygosaccharomyces rouxii and quality of apple juice.* Food Chemistry, 254, 201-207.

[66] Katrine-Rød, S. et. al. (2012) *Cold atmospheric pressure plasma treatment of ready-to-eat meat: Inactivation of Listeria innocua and changes in product quality.* Food Microbiology, 30, 1, 233-238.

[67] Fridman, G. et. al. (2008) *Applied plasma medicine.* Plasma Proc. Polym. 5 503–33.

[68] Shahbazi Rad, Z. Abbasi Davani, F. (2020) *Measurements of the electrical parameters and wound area for investigation on the effect of different non-thermal atmospheric pressure plasma sources on wound healing time.* Journal of the International Measurement Confederation, 155.

[69] Fridman, G. et. al. (2006) *Blood Coagulation and Living Tissue Sterilization by Floating-Electrode Dielectric Barrier Discharge in Air*. Plasma Chemistry and Plasma Processing, 26, 425–442.

[70] Kong, M. G. et. al. (2009) *Plasma Medicine: An Introductory Review.* J. Phys, 11, 115012.

[71] Kim, J. Y. et. al. (2013) *The Efficiency of Atmospheric Dielectric Barrier Discharge Plasma against Escherichia coli and Bacillus cereus on Dried Laver (Porphyra tenera).* Foods, 9, 1013.

[72] Garcia-Alcantara, E. et. al. (2013) *Accelerated mice skin acute wound healing in vivo by combined treatment of argon and helium plasma needle.* Arch. Med. Res 44 (3), 169-177.

[73] Fridman, G. et. al. (2005) *Use of non-thermal atmospheric pressure plasma discharge for coagulation and sterilization of surface wounds.* 17th International Symposium on Plasma Chemistry. Toronto, Canada.

[74] Tanaka, H. et. al. (2018) *New Hopes for Plasma-Based Cancer Treatment.* Plasma, 1, 1, 150-155.

[75] Nuccitelli, R. et. al. (2006). *Nanosecond pulsed electric fields cause melanomas to self-destruct.* Biochemical and Biophysical Research Communications, 344 (2), 351-360.

[76] Zhang X. H. et. al. (2008) *Ablation of liver cancer cells in vitro by a plasma needle.* Appl. Phys. Lett. 93, 021502.

[77] Nupangtha, W. (2021) *A surface dielectric barrier discharge non-thermal plasma to induce cell death in colorectal cancer cells*. AIP Advances, 11, 075222.

[78] Lu X P, Cao Y G, Yang P, Xiong Q, Xiong Z L, Xian Y B and Pan Y (2009) *An RC plasma device for sterilization of root canal of teeth*. IEEE Trans. Plasma Sci. 37 668–73

[79] Sun, P. et. al. (2011) *Atmospheric pressure cold plasma as an antifungal therapy.* Appl. Phys. Lett. 98, 021501.

[80] Glover, J. L. et. al. (1982) *The plasma scalpel: a new thermal knife.* Lasers Surg. Med. 2 (1), 101-106.

[81] Elsaie, M. L. and Kammer, J. N. (2008) *Evaluation of plasma skin regeneration technology for cutaneous remodeling.* J. Cosmet. Dermatol. 7, 309–11.

[82] Moradi, E. et. al. (2020) *Prolonging shelf life of chicken breast fillets by using plasma-improved chitosan/low density polyethylene bilayer film containing summer savory essential oil*. Macromolecules, 156, 321-328.

[83] Boeuf, J. P. Pitchford, L. C. (2005) *Electrohydrodynamic force and aerodynamic flow acceleration in surface dielectric barrier discharge*. Journal of Applied Physics 97, 10.

[84] Singh, K. P. (2006) *Modeling of dielectric barrier discharge plasma actuator with atmospheric air chemistry*. Collection of Technical Papers - 37th AIAA Plasmadynamics and Lasers Conference, 2, 576-586.

[85] Audier, P. (2012) *Study of a Surface Barrier Discharge. Flow Control Applications over a naca0012 aerofoil. PhD, Universite d'Orleans, Orleans, France.*

[86] Wilde, N. D. (2018) *Optimization of Surface Dielectric Barrier Discharge Ion Sources for Electroaerodynamic Propulsion.* MSc, Massachusetts Institute of Technology, Cambridge, USA.

[87] Browning, P. Shambaugh, B. and Dygert. J. *Experimental study of dielectric barrier discharge driven duct flow for propulsion applications in unmanned aerial systems*. SAE Technical Paper 2017-01-2063.

[88] Hof, B. et. al. (2010) *Eliminating turbulence in spatially intermittent flows.* Science 327, 1491.

[89] Huang, X. Zhang, X. (2008). *Streamwise and Spanwise Plasma Actuators for Flow-Induced Cavity Noise Control*. Physics of Fluids, 20 (3): 037101–037101–10.

[90] Rodrigues, F. F. et. al. (2018) *Experimental Analysis of Dielectric Barrier Discharge Plasma Actuators Thermal Characteristics Under External Flow Influence*. J. Heat Transfer. 140(10): 102801.

[91] Miralai, S. F. et. al. (2000) *Electrical and optical diagnostics of dielectric barrier discharges (DBD) in HE and N2 for polymer treatment.* Plasmas and Polymers, 5 (2), 63-77.

[92] Bruggeman, P. and Brandenburg, R. (2013) At*mospheric pressure discharge filaments and microplasmas: physics, chemistry and diagnostics.* J. Phys. D: Appl. Phys. 46, 464001.

[93] Shuai, Y. Tingfeng, Y. Baohong, Y. (2019) *An ICCD camera-based time-domain ultrasound-switchable fluorescence imaging system.* Scientific Reports, 9, 10552.

[94] Callegari, T. et. al. (2014) *Pattern formation and dynamics of plasma filaments in dielectric barrier discharges*. Plasma Sources Sci. Technol. 23, 054003.

[95] Purwins, H. G. (2010) *Dissipative Solutions.* Advances in Physics, 59, 5.

[96] Vila, R. et. al. (1998) *Dielectric spectroscopy of alumina ceramics over a wide frequency range.* Journal of Nuclear Materials, 253, 1, 141-148.

[97] Pavlovich, M. J. Clark, D. S. Graves, D. B. (2014) *Quantification of air plasma chemistry for surface disinfection*. Plasma Sources Sci. Technol. 23, 065036.

[98] Bansemer, R. et. al. (2017) Investigation and control of the 0_3 to NO transition in a novel sub-atmospheric pressure dielectric barrier discharge Plasma Sources Sci. Technol. 26, 065005.

[99] Kogelschatz, U. (2003) *Dielectric-Barrier Discharges: Their History, Discharge Physics, and Industrial Applications.* Plasma Chemistry and Plasma Processing volume 23, 1–46.

[100] Falkenstein, Z. and Coogan, J. J. (1997) *Microdischarge behaviour in the silent discharge of nitrogen - oxygen and water - air mixtures.* J. Phys. D: Appl. Phys. 30, 817.

[101] Mericam-Bourdet, N. et. al. (2012) *Effect of voltage waveform on dielectric barrier discharge ozone production efficiency.* European Physical Journal: Applied Physics, EDP Sciences, 57 (3).

[102] Nupangtha, W. et. al. (2021) *A surface dielectric barrier discharge non-thermal plasma to induce cell death in colorectal cancer cells.* AIP Advances 11, 075222.

[103] Li, J. et. al. (2019) *A Review of Recent Advances of Dielectric Barrier Discharge Plasma in Catalysis. 2nd Edn. (Düsseldorf: Verlag DVS).*

[104] Dickenson, A. et. al. (2018) *The generation and transport of reactive nitrogen species from a low temperature atmospheric pressure air plasma source*. Phys. Chem. 20, 28499-28510.

[105] Voráč, J. et. al. (2019) *Time and space-resolved LIF measurement of the concentration of OH radicals generated by surface barrier discharge emerging from liquid water.* Plasma Sources Science and Technology, 28, 105008.

[106] Ambrico, P. F. et. al. (2008) *On the Measurement of N2(A3Σ +u) Metastable in N2 Surface-Dielectric Barrier Discharge at Atmospheric Pressure.* Plasma Chemistry and Plasma Processing, 28, 299–316.

[107] Teramotoa, Y. et. al. (2014) *Measurement of OH (X2Σ) in immediate vicinity of dielectric surface under pulsed dielectric barrier discharge at atmospheric pressure using two geometries of laser-induced fluorescence.* Journal of Applied Physics 115, 133302.

[108] Li, D. et. al. (2016) *OH radical production in an atmospheric pressure surface micro-discharge array.* Journal of Physics D: Applied Physics, 49, 45.

[109] Nishida, H. et. al. (2020) *Single-Pixel Particle Image Velocimetry for Characterization of Dielectric Barrier Discharge Plasma Actuators.* AIAA Journal, 58 (11).

[110] Cristofolinia, A. et. al. (2012) *Schlieren imaging in a dielectric barrier discharge actuator for airflow control.* Journal of Applied Physics 111, 033302.

[111] Neretti, G. Cristofolini, A. Borghic, C. A. (2014) *Experimental investigation on a vectorized aerodynamic dielectric barrier discharge plasma actuator array.* Journal of Applied Physics, 115, 163304.

[112] Gao, G. et. al. (2017) *Comparison of the surface dielectric barrier discharge characteristics under different electrode gaps.* Physics of Plasmas, 24, 013510.

[113] Do, H. et. al. (2007) *Bluff Body Flow Separation Control Using Surface Dielectric Barrier Discharges.* 45th AIAA Aerospace Sciences Meeting and Exhibit. AIAA 2007-939.

[114] Moreau, E. et. al. (2008) *Electric wind induced by sliding discharge in air at atmospheric pressure.* Journal of Electrostatics, 66, 1–2, 107-114.

[115] Zito, J. C. et. al. (2012) Flow and force inducement using micron size dielectric barrier discharge actuators. Appl. Phys. Lett. 100, 193502.

[116] Dickenson, A. (2017) *Directional mass transport in an atmospheric pressure surface barrier discharge.*

[117] Xie, Q. (2019) *Effect of rise time on nanosecond pulsed surface dielectric barrier discharge actuator.* IEEE Transactions on Dielectrics and Electrical Insulation, 26, 2.

[118] Sato, S. et. al. (2018) Induced Flow Simulation with Detailed Discharge Modeling in Dielectric-Barrier-Discharge Plasma Actuator. AIAA, 2018-1293.

[119] Leonov, S. B. et. al. (2016) *Dynamics of near-surface electric discharges and mechanisms of their interaction with the airflow.* Plasma Sources Sci. Technol. 25, 063001.

[120] Benard, N. Moreau, E. (2014) *Electrical and mechanical characteristics of surface AC dielectric barrier discharge plasma actuators applied to airflow control.* Exp. Fluids, 55, 1846.

[121] Jussot, R. (2012) *Thermal Characterization of a DBD Plasma Actuator: Dielectric Temperature Measurements Using Infrared Thermography*. 40th Fluid Dynamics Conference and Exhibit, Chicago, Illinois.

[122] Hsiao, R. C. et. al. (2015) *Numerical Study on Heat Flow During Catalytic Dissociation of Ozone in a Dielectric Barrier Discharge Ozonizer*. IEEE Transactions on Plasma Science, 43, 2.

[123] Takaki, K. et. al. (2004) *Effect of electrode shape in dielectric barrier discharge plasma reactor for NOx removal.* IEEE Transactions on Plasma Science, 32, 1.

[124] Eliasson, B. Egli, U. Kogelschatz, U. (1994) *Modelling of dielectric barrier discharge chemistry.* Pure and Applied Chemistry, 66, 6.

[125] Sakiyama, Y. et. al. (2012). *Plasma chemistry model of surface microdischarge in humid air and dynamics* of reactive neutral species*.* J. Phys. D: Appl. Phys. 45, 42.

[126] Shimizu, T. Sakiyama, Y. Graves, D. B. Zimmermann, J. L. Morfill, G. E. (2012) *Efficient modeling of atmospheric pressure surface micro-discharge plasma chemistry.* New J. Phys. 14, 103028.

[127] Shimizu, T. et. al. (2012) *The dynamics of ozone generation and mode transition in air surface micro-discharge plasma at atmospheric pressure.* Journal of Physics 14, 103028.

[128] Yi, C. et. al. (2017) *Self-consistent plasma chemistry model for surface microdischarge in humid air including effects of ohmic heating and gas flow.* Plasma Sources Sci. Technol. 26, 105007.

[129] Bansemer, R. et. al. (2017) *Investigation and control of the O3-to NO-transition in a novel sub-atmospheric pressure dielectric barrier discharge.* Plasma Sources Sci. Technol. 26, 065005.

[130] Liu, Z. C. et. al. (2015) *Physicochemical processes in the indirect interaction between surface air plasma and deionized water.* J. Phys. D: Appl. Phys. 48, 495201.

[131] Liu, D. X. (2016) *Aqueous reactive species induced by a surface air discharge: Heterogeneous mass transfer and liquid chemistry pathways.* Scientific Reports, 6, 23737.

[132] Hasan, M. I. Walsh, J. (2016) *Numerical investigation of the spatiotemporal distribution of chemical species in an atmospheric surface barrier-discharge.* Journal of Applied Physics 119, 203302.

[133] Hasan, M. I. (2017) *Influence of gas flow velocity on the transport of chemical species in an atmospheric pressure air plasma discharge.* Appl. Phys. Lett. 110, 134102.

[134] Patankar, S. V. (1980) *Numerical Heat Transfer and Fluid Flow.* New York, McGraw-Hill, p 102. ISBN: 0-89116-522-3.

[135] Solov'ev, V. R. et. al. (2008) *Numerical simulation of a surface barrier discharge.* Plasma Physics Reports, 34, 594–608.

[136] Enloe, C. L. et. al. (2004) *Mechanisms and Responses of a Single Dielectric Barrier Plasma Actuator: Geometric Effects.* AIAA JOURNAL, 42, 3, 80840-6222.

[137] Boeuf, J. P. Lagmich, Y. Pitchford, L. C. (2009) *Contribution of positive and negative ions to the electrohydrodynamic force in a dielectric barrier discharge plasma actuator operating in air.* Journal of Applied Physics, 106, 023115.

[138] Balaji, J. Cho, Y-C. & Shyy, W.(2008) M*odeling of dielectric barrier discharge plasma actuator.* Journal of Applied Physics, 103, 053304.

[139] Starikovskii, A. Y. et. al. (2009) *SDBD plasma actuator with nanosecond pulse-periodic discharge.* Plasma Sources Sci. Technol. 18, 034015.

[140] Zhu, Y. et. al. (2017) *Nanosecond surface dielectric barrier discharge in atmospheric pressure air: I. measurements and 2D modeling of morphology, propagation and hydrodynamic perturbations*. Plasma Sources Sci. Technol. 26, 125004.

[141] Kourtzanidis, K. (2017) Three-Electrode Sliding Nanosecond Dielectric Barrier Discharge Actuator: Modeling and Physics. AIAA JOURNAL, 55, 4.

[142] Zhu, Y. Starikovskaia, S. (2018) *Fast gas heating of nanosecond pulsed surface dielectric barrier discharge: spatial distribution and fractional contribution from kinetics.* Plasma Sources Sci. Technol. 27, 124007.

[143] Nishida, H. Nonomura, T. & Abe, T. (2014) *Three-dimensional simulations of discharge plasma evolution on a dielectric barrier discharge plasma actuator.* Journal of Applied Physics 115, 133301.

[144] Babaeva, N. Y. Tereshonok, D. V. & Naidis, G. V. (2016) *Fluid and hybrid modeling of nanosecond surface discharges: effect of polarity and secondary electrons emission.* Plasma Sources Sci. Technol. 25, 044008.

[145] Gaitonde, D. McCrink, M. (2012) A Semi-Empirical Model of a Nanosecond Pulsed Plasma Actuator for Flow Control Simulations with LES. AIAA, 2012-0184.

[146] Kogelschatz, U. Baessler, P. (1987) *Determination of Nitrous Oxide and Dinitrogen Pentoxide Concentrations in the Output of Air-Fed Ozone Generators of High Power Density*. The Journal of the International Ozone Association, 9, 3, 195-206.

[147] Wang, J. C. (2013) Characteristics of a radio-frequency micro-dielectric barrier discharge array. Plasma Sources Sci. Technol. 22, 025015.

[148] Pryor, R. W. (2015) *Modeling Dielectric Heating: A First Principles Approach*. Proceedings of the 2015 Comsol Conference, Boston.

[149] Hagelaar, G. J. M. Pitchford, L. C. (2005) *Solving the Boltzmann equation to obtain electron transport coefficients and rate coefficients for fluid models. P*lasma Sources Sci. Technol. 14, 722-733.

[150] Biagi database, www.lxcat.net, retrieved May 15, 2019.

[151] Hansen, L. et. al. (2021) *Understanding the energy balance of a surface barrier discharge for various molecular gases by a multi-diagnostic approach.* Journal of Applied Physics 129, 053308.

[152] Moreau, E. et. al. (2013) *Surface Dielectric Barrier Discharge Plasma Actuators*. ERCOFTAC Bulletin, 94.

[153] Babaeva, N. (2016) *Fluid and hybrid modeling of nanosecond surface discharges: effect of polarity and secondary electrons emission.* Plasma Sources Science and Technology, 25, 044008.

[154] Kim, J. et. al. (2018) *Discharge Characteristics and Plasma Erosion of Various Dielectric Materials in the Dielectric Barrier Discharges.* Appl. Sci. 8, 1294.

[155] Ordonez, C. A. (1996) *Numerical determination of plasma ion reflection coefficients at a sheath-surface interface.* Journal of Nuclear Materials, 228, 2, 201-6.

[156] Zhang, X. et. al. (2016) *Ozone Production With Dielectric Barrier Discharge: Effects of Power Source and Humidity.* EEE Transaction on Plasma Science, 44, 10.

[157] Abdelaziz, A. A. et. al. (2018) *Quantitative Analysis of Ozone and Nitrogen Oxides Produced by a Low Power Miniaturized Surface Dielectric Barrier Discharge: Effect of Oxygen Content and Humidity Level*. Plasma Chemistry and Plasma Processing. 39, 165–185.

[158] Zhu, Y. et. al. (2013) *Numerical investigation of energy transfer for fast gas heating in an atmospheric nanosecond-pulsed DBD under different negative slopes*. Journal of Physics D: Applied Physics, 46, 49.

[159] Sigmund, P. (1987) *Mechanisms and theory of physical sputtering by particle impact*. Nuclear Instruments and Methods in Physics Research Section B; Beam Interactions with Materials and Atoms, 27, 1, 1-20.

[160] Engineering ToolBox, (2010). Relative Permittivity - the Dielectric Constant. [online] Available at: https://www.engineeringtoolbox.com/relative-permittivity-d_1660.html (Accessed 01/05/2019).

[161] MATLAB and Statistics Toolbox Release 2012b, The MathWorks, Inc., Natick, Massachusetts, United States.

[162] Lagmich, Y. et. al. (2007) *Electrohydrodynamic force and scaling laws in surface dielectric barrier discharge*. Applied Physics Letters, 90, 0151502.

[163] Material Properties Data: Alumina (Aluminum Oxide) Archived 2010-04-01 at the Wayback Machine. Makeitfrom.com. (Accessed 11/05/2020).

[164] Jonscher, A. K. (1977) *The 'Universal' Dielectric Constant*. Nature, 267, 673-9.

[165] Wang, Y. N. et. al. (2020) *Analysis of Output Characteristics of Capillary Discharge Based Pulsed Plasma Thruster.* Journal of Propulsion Technology, 41 (1), 149-156.

[166] Kolobov, V. and Arslanbekov, R. (2016) *Electrostatic PIC with adaptive Cartesian mesh*. J. Phys.: Conf. Ser. 719, 012020.

[167] Abdollahzadeh, M. et. al. (2016) *Implementation of the classical plasma–fluid model for simulation of dielectric barrier discharge (DBD) actuators in OpenFOAM.* Computers & Fluids, 128, 10, 77-90.

[168] Shahbazi Rad, Z. Abbasi Davani, F. (2020) *Measurements of the electrical parameters and wound area for investigation on the effect of different non-thermal atmospheric pressure plasma sources on wound healing time.* Journal of the International Measurement Confederation, 155.

[169] Limam, S. (2011) *Non-thermal plasma treatment of contaminated surfaces: Remote exposure to atmospheric pressure dielectric barrier discharge effluent.* Advanced Materials Research, 324, 469-472.

[170] Gerhard, C. et. al. (2018) *Plasma jet cleaning of optics: Cleaning of silver-coated mirrors by means of atmospheric pressure plasma jets*. Vakuum in Forschung und Praxis, 30, 3, 32-35.

Appendix A: Chemical reactions in the chemistry module

This appendix contains the list of reactions incorporated in the chemistry module used in this work. In the table below T_e refers to the electron temperature (K) in the discharge and T_g refers to the temperature of the gas (K).

Index	Reaction	Rate constant[a]
(R1)	$e + N_2 \rightarrow N(^2D) + N + e$	$3.99 \times 10^{-17} \varepsilon^{2.24} \exp(-9.10/\varepsilon)$
(R2)	$e + N_2 \rightarrow N_2(A\ ^3\Sigma) + e$	$3.34 \times 10^{-16} \varepsilon^{-0.06} \exp(-8.50/\varepsilon)$
(R3)	$e + N_2 \rightarrow N_2(B\ ^3\Pi) + e$	$8.44 \times 10^{-15} \varepsilon^{-0.33} \exp(-9.15/\varepsilon)$
(R4)	$e + N_2 \rightarrow N_2^+ + e + e$	$1 \times 10^{-16} \varepsilon^{1.90} \exp(-14.6/\varepsilon)$
(R5)	$e + N \rightarrow N(^2D) + e$	$5.06 \times 10^{-15} \exp(-10.8/\varepsilon^{3.95})$
(R6)	$e + N \rightarrow N^+ + e + e$	$1.45 \times 10^{-17} \varepsilon^{2.58} \exp(-8.54/\varepsilon)$
(R7)	$e + O_2 \rightarrow O + O + e$	$2.03 \times 10^{-14} \varepsilon^{-0.10} \exp(-8.47/\varepsilon)$
(R8)	$e + O_2 \rightarrow O(^1D) + O + e$	$1.82 \times 10^{-14} \varepsilon^{-0.13} \exp(-10.7/\varepsilon)$
(R9)	$e + O_2 \rightarrow O_2(a\ ^1\Delta) + e$	$1.04 \times 10^{-15} \exp(-2.59/\varepsilon)$
(R10)	$e + O_2 \rightarrow O_2^+ + e + e$	$9.54 \times 10^{-12} \varepsilon^{-1.05} \exp(-55.6/\varepsilon)$
(R11)	$e + O_3 \rightarrow O + O_2 + e$	$1.78 \times 10^{-12} \varepsilon^{-0.614} \exp(-11.5/\varepsilon)$
(R12)	$e + O \rightarrow O(^1D) + e$	$7.46 \times 10^{-15} \exp(-5.58/\varepsilon^{1.47})$
(R13)	$e + O \rightarrow O^+ + e + e$	$4.75 \times 10^{-15} \varepsilon^{0.61} \exp(-22.1/\varepsilon)$
(R14)	$e + H_2O \rightarrow H_2O^+ + e + e$	$9.65 \times 10^{-18} \varepsilon^{2.53} \exp(-8.99/\varepsilon)$
(R15)	$e + H_2O \rightarrow OH^+ + H + e + e$	$9.89 \times 10^{-12} \varepsilon^{-1.64} \exp(-67.6/\varepsilon)$
(R16)	$e + H_2O \rightarrow H^+ + OH + e + e$	$7.45 \times 10^{-15} \varepsilon^{0.34} \exp(-54.2/\varepsilon)$
(R17)	$e + H_2O \rightarrow O^+ + H_2 + e + e$	$7.4 \times 10^{-16} \varepsilon^{0.45} \exp(-55.5/\varepsilon)$
(R18)	$e + H_2O \rightarrow H_2^+ + O + e + e$	$8.49 \times 10^{-15} \varepsilon^{-1.23} \exp(-74.0/\varepsilon)$
(R19)	$e + H_2O \rightarrow OH + H + e$	$5.15 \times 10^{-15} \varepsilon^{0.62} \exp(-10.9/\varepsilon)$
(R20)	$e + H_2O \rightarrow H_2 + O(^1D) + e$	$5.19 \times 10^{-18} \varepsilon^{1.2} \exp(-13.8/\varepsilon)$
(R21)	$e + H_2 \rightarrow H + H + e$	$3.29 \times 10^{-15} \varepsilon^{0.578} \exp(-7.56/\varepsilon)$
(R22)	$e + H_2 \rightarrow H_2^+ + e + e$	$4 \times 10^{-17} \varepsilon^{2.13} \exp(-14.9/\varepsilon)$
(R23)	$e + N_2O_5 \rightarrow NO_2^+ + NO_3 + e + e$	$2.43 \times 10^{-17} \varepsilon^{2.77} \exp(-5.62/\varepsilon)$
(R24)	$e + N^+ + M \rightarrow N + M$	$3.12 \times 10^{-35} / T_e^{1.5}$
(R25)	$e + N_2^+ \rightarrow N + N$	$1.66 \times 10^{-12} / T_e^{0.7}$
(R26)	$e + N_2^+ \rightarrow N(^2D) + N$	$1.5 \times 10^{-12} / T_e^{0.7}$
(R27)	$e + N_2^+ + M \rightarrow N_2 + M$	$3.12 \times 10^{-35} / T_e^{1.5}$
(R28)	$e + N_3^+ \rightarrow N_2 + N$	$3.46 \times 10^{-12} / T_e^{0.5}$
(R29)	$e + N_4^+ \rightarrow N_2 + N_2$	$4.73 \times 10^{-11} / T_e^{0.53}$
(R30)	$e + O^+ + M \rightarrow O + M$	$3.12 \times 10^{-35} / T_e^{1.5}$
(R31)	$e + O_2^+ \rightarrow O + O$	$1.68 \times 10^{-11} / T_e^{0.7}$
(R32)	$e + O_2^+ \rightarrow O + O(^1D)$	$1.24 \times 10^{-11} / T_e^{0.7}$
(R33)	$e + O_2^+ + M \rightarrow O_2 + M$	$3.12 \times 10^{-35} / T_e^{1.5}$
(R34)	$e + O_4^+ \rightarrow O_2 + O_2$	$2.42 \times 10^{-11} / T_e^{0.5}$
(R35)	$e + N_2O^+ \rightarrow N_2 + O$	$3.46 \times 10^{-12} / T_e^{0.5}$
(R36)	$e + NO^+ \rightarrow N + O$	$1.07 \times 10^{-11} / T_e^{0.85}$
(R37)	$e + NO^+ \rightarrow N(^2D) + O$	$4.28 \times 10^{-11} / T_e^{0.85}$
(R38)	$e + NO^+ + M \rightarrow NO + M$	$3.12 \times 10^{-35} / T_e^{1.5}$
(R39)	$e + NO_2^+ \rightarrow NO + O$	$3.46 \times 10^{-12} / T_e^{0.5}$
(R40)	$e + H_2^+ \rightarrow H + H$	$1.86 \times 10^{-13} / T_e^{0.43}$
(R41)	$e + H_3^+ \rightarrow H + H_2$	$5.20 \times 10^{-11} / T_e^{0.5}$
(R42)	$e + H_3^+ \rightarrow H + H + H$	$1.14 \times 10^{-11} / T_e^{0.97}$
(R43)	$e + H_2O^+ \rightarrow OH + H$	$2.73 \times 10^{-12} / T_e^{0.5}$
(R44)	$e + H_2O^+ \rightarrow O + H_2$	$1.37 \times 10^{-12} / T_e^{0.5}$
(R45)	$e + H_2O^+ \rightarrow O + H + H$	$1.37 \times 10^{-12} / T_e^{0.5}$
(R46)	$e + H_3O^+ \rightarrow OH + H + H$	$5.46 \times 10^{-12} / T_e^{0.5}$
(R47)	$e + e + N^+ \rightarrow N + e$	$1 \times 10^{-31} (T_g/T_e)^{4.5}$
(R48)	$e + e + N_2^+ \rightarrow N_2 + e$	$1 \times 10^{-31} (T_g/T_e)^{4.5}$
(R49)	$e + e + O^+ \rightarrow O + e$	$1 \times 10^{-31} (T_g/T_e)^{4.5}$
(R50)	$e + e + O_2^+ \rightarrow O_2 + e$	$1 \times 10^{-31} (T_g/T_e)^{4.5}$
(R51)	$e + e + NO^+ \rightarrow NO + e$	$1 \times 10^{-31} (T_g/T_e)^{4.5}$
(R52)	$e + e + H^+ \rightarrow H + e$	$1 \times 10^{-31} (T_g/T_e)^{4.5}$
(R53)	$e + e + H_2^+ \rightarrow H_2 + e$	$1 \times 10^{-31} (T_g/T_e)^{4.5}$
(R54)	$e + e + OH^+ \rightarrow OH + e$	$1 \times 10^{-31} (T_g/T_e)^{4.5}$
(R55)	$e + e + H_2O^+ \rightarrow H_2O + e$	$1 \times 10^{-31} (T_g/T_e)^{4.5}$
(R56)	$e + O + O_2 \rightarrow O^- + O_2$	1×10^{-43}
(R57)	$e + O + O_2 \rightarrow O_2^- + O$	1×10^{-43}
(R58)	$e + O_2 + O_2 \rightarrow O_2^- + O_2$	$1.4 \times 10^{-41} T_g/T_e \exp(-600/T_g) \times \exp\{700(T_e - T_g)/(T_e T_g)\}$
(R59)	$e + O_2 + N_2 \rightarrow O_2^- + N_2$	$1.1 \times 10^{-43} (T_g/T_e)^2 \exp(-70/T_g) \times \exp\{1500(T_e - T_g)/(T_e T_g)\}$
(R60)	$e + O_2 \rightarrow O^- + O$	$2.63 \times 10^{-16} \varepsilon^{-0.495} \exp(-5.65/\varepsilon)$
(R61)	$e + O_2 \rightarrow O_2^-$	$9.72 \times 10^{-15} \varepsilon^{-1.62} \exp(-14.2/\varepsilon)$ for $\varepsilon > 1.1$ 2.78×10^{-20} for $\varepsilon < 1.1$
(R62)	$e + O_3 \rightarrow O^- + O_2$	1×10^{-17}

(R63)	$e + O_3 \rightarrow O_2^- + O$	1×10^{-15}
(R64)	$e + O_3 + M \rightarrow O_3^- + M$	1×10^{-43}
(R65)	$e + N_2O \rightarrow O^- + N_2$	2×10^{-16}
(R66)	$e + NO + M \rightarrow NO^- + M$	8×10^{-43}
(R67)	$e + NO_2 \rightarrow O^- + NO$	1×10^{-17}
(R68)	$e + NO_2 + M \rightarrow NO_2^- + M$	1.5×10^{-42}
(R69)	$e + NO_3 + M \rightarrow NO_3^- + M$	1×10^{-42}
(R70)	$e + H_2O \rightarrow H^- + OH$	$4.42 \times 10^{-14} \varepsilon^{-2.0} \exp(-13.39/\varepsilon)$
(R71)	$e + H_2O \rightarrow O^- + H_2$	$2.97 \times 10^{-15} \varepsilon^{-1.56} \exp(-13.67/\varepsilon)$
(R72)	$e + H_2O \rightarrow OH^- + H$	$9.6 \times 10^{-16} \varepsilon^{-1.70} \exp(-13.31/\varepsilon)$
(R73)	$e + HNO_3 \rightarrow NO_2^- + OH$	5×10^{-14}
(R74)	$O^- + N \rightarrow NO + e$	2.6×10^{-16}
(R75)	$O^- + N_2 \rightarrow N_2O + e$	1×10^{-18}
(R76)	$O^- + N_2(A\,^3\Sigma) \rightarrow N_2 + O + e$	2.2×10^{-15}
(R77)	$O^- + N_2(B\,^3\Pi) \rightarrow N_2 + O + e$	1.9×10^{-15}
(R78)	$O^- + O \rightarrow O_2 + e$	1.4×10^{-16}
(R79)	$O^- + O_2 \rightarrow O_3 + e$	1×10^{-18}
(R80)	$O^- + O_2(a\,^1\Delta) \rightarrow O_3 + e$	3×10^{-16}
(R81)	$O^- + O_3 \rightarrow O_2 + O_2 + e$	3×10^{-16}
(R82)	$O^- + NO \rightarrow NO_2 + e$	2.6×10^{-16}
(R83)	$O^- + H_2 \rightarrow H_2O + e$	7×10^{-16}
(R84)	$O_2^- + N \rightarrow NO_2 + e$	5×10^{-16}
(R85)	$O_2^- + N_2 \rightarrow N_2 + O_2 + e$	$1.9 \times 10^{-18} (T_g/300)^{0.5} \exp(-4990/T_g)$
(R86)	$O_2^- + N_2(A\,^3\Sigma) \rightarrow N_2 + O_2 + e$	2.1×10^{-15}
(R87)	$O_2^- + N_2(B\,^3\Pi) \rightarrow N_2 + O_2 + e$	2.5×10^{-15}
(R88)	$O_2^- + O \rightarrow O_3 + e$	1.5×10^{-16}
(R89)	$O_2^- + O_2 \rightarrow O_2 + O_2 + e$	$2.7 \times 10^{-16}\ (T_g/300)^{0.5} \exp(-5590/T_g)$
(R90)	$O_2^- + O_3 \rightarrow O_3 + O_2 + e$	6×10^{-16}
(R91)	$O_2^- + O_2(a\,^1\Delta) \rightarrow O_2 + O_2 + e$	2×10^{-16}
(R92)	$O_2^- + H \rightarrow HO_2 + e$	1.4×10^{-15}
(R93)	$O_3^- + O \rightarrow O_2 + O_2 + e$	3×10^{-16}
(R94)	$O_3^- + O_2 \rightarrow O_3 + O_2 + e$	2.3×10^{-17}
(R95)	$O_3^- + O_3 \rightarrow O_2 + O_2 + O_2 + e$	3×10^{-16}
(R96)	$NO^- + M \rightarrow NO + M + e$	2.40×10^{-19}
(R97)	$NO^- + NO \rightarrow NO + NO + e$	5×10^{-18}
(R98)	$NO^- + N_2O \rightarrow NO + N_2O + e$	5.1×10^{-18}
(R99)	$NO^- + H_2 \rightarrow NO + H_2 + e$	2.3×10^{-19}
(R100)	$NO_2^- + O \rightarrow NO_3 + e$	1×10^{-18}
(R10)1	$NO_2^- + N \rightarrow N_2 + O_2 + e$	1×10^{-18}
(R102)	$NO_3^- + O \rightarrow NO_2 + O_2 + e$	1×10^{-18}
(R103)	$NO_3^- + N \rightarrow N_2 + O_3 + e$	1×10^{-18}
(R104)	$H^- + O_2 \rightarrow HO_2 + e$	1.2×10^{-15}
(R105)	$H^- + H \rightarrow H_2 + e$	1.8×10^{-15}
(R106)	$OH^- + O \rightarrow HO_2 + e$	2×10^{-16}
(R107)	$OH^- + H \rightarrow H_2O + e$	1.8×10^{-15}
(R108)	$N^+ + N + M \rightarrow N_2^+ + M$	1×10^{-41}
(R109)	$N^+ + N_2 + M \rightarrow N_3^+ + M$	4.6×10^{-41}
(R110)	$N^+ + N_2O \rightarrow NO^+ + N_2$	5.5×10^{-16}
(R111)	$N^+ + NO \rightarrow NO^+ + N$	4.72×10^{-16}
(R112)	$N^+ + NO \rightarrow N_2^+ + O$	8.33×10^{-17}
(R113)	$N^+ + NO \rightarrow O^+ + N_2$	1×10^{-18}
(R114)	$N^+ + NO_2 \rightarrow NO_2^+ + N$	3×10^{-16}
(R115)	$N^+ + NO_2 \rightarrow NO^+ + NO$	5×10^{-16}
(R116)	$N^+ + O \rightarrow O^+ + N$	1×10^{-18}
(R117)	$N^+ + O + M \rightarrow NO^+ + M$	1×10^{-41}
(R118)	$N^+ + O_2 \rightarrow NO^+ + O$	2.7×10^{-16}
(R119)	$N^+ + O_2 \rightarrow O^+ + NO$	2.8×10^{-17}
(R120)	$N^+ + O_2 \rightarrow O_2^+ + N$	3×10^{-16}
(R121)	$N^+ + O_3 \rightarrow NO^+ + O_2$	5×10^{-16}
(R122)	$N^+ + OH \rightarrow OH^+ + N$	3.4×10^{-16}
(R123)	$N^+ + OH \rightarrow NO^+ + H$	3.4×10^{-16}
(R124)	$N^+ + H_2O \rightarrow H_2O^+ + N$	1.19×10^{-15}
(R125)	$N^+ + H_2O \rightarrow NO^+ + H_2$	2.1×10^{-16}
(R126)	$N_2^+ + N \rightarrow N^+ + N_2$	1×10^{-18}
(R127)	$N_2^+ + N + M \rightarrow N_3^+ + M$	$1 \times 10^{-41}\ (300/T_g)$

(R128)	$N_2^+ + N_2 + M \rightarrow N_4^+ + M$	$1 \times 10^{-41}\ (300/T_g)$
(R129)	$N_2^+ + N_2(A\ ^3\Sigma) \rightarrow N_3^+ + N$	3×10^{-16}
(R130)	$N_2^+ + N_2O \rightarrow N_2O^+ + N_2$	6×10^{-16}
(R131)	$N_2^+ + N_2O \rightarrow NO^+ + N + N_2$	4×10^{-16}
(R132)	$N_2^+ + NO \rightarrow NO^+ + N_2$	3.9×10^{-16}
(R133)	$N_2^+ + NO_2 \rightarrow NO^+ + N_2O$	5×10^{-17}
(R134)	$N_2^+ + NO_2 \rightarrow NO_2^+ + N_2$	3×10^{-16}
(R135)	$N_2^+ + O \rightarrow NO^+ + N$	1.4×10^{-16}
(R136)	$N_2^+ + O \rightarrow NO^+ + N(^2D)$	$1.8 \times 10^{-16}\ (300/T_g)$
(R137)	$N_2^+ + O \rightarrow O^+ + N_2$	$1 \times 10^{-17}\ (300/T_g)^{0.5}$
(R138)	$N_2^+ + O_2 \rightarrow O_2^+ + N_2$	5×10^{-17}
(R139)	$N_2^+ + O_3 \rightarrow O_2^+ + O + N_2$	1×10^{-16}
(R140)	$N_2^+ + H_2O \rightarrow H_2O^+ + N_2$	2.3×10^{-15}
(R141)	$N_3^+ + N \rightarrow N_2^+ + N_2$	6.6×10^{-17}
(R142)	$N_3^+ + O_2 \rightarrow O_2^+ + N + N_2$	2.3×10^{-17}
(R143)	$N_3^+ + O_2 \rightarrow NO^+ + O + N_2$	2×10^{-17}
(R144)	$N_3^+ + O_2 \rightarrow NO_2^+ + N_2$	4.4×10^{-17}
(R145)	$N_3^+ + NO \rightarrow NO^+ + N_2 + N$	7×10^{-17}
(R146)	$N_3^+ + NO \rightarrow N_2O^+ + N_2$	7×10^{-17}
(R147)	$N_3^+ + N_2O \rightarrow NO^+ + N_2 + N_2$	5×10^{-17}
(R148)	$N_3^+ + NO_2 \rightarrow NO^+ + NO + N_2$	7×10^{-17}
(R149)	$N_3^+ + NO_2 \rightarrow NO_2^+ + N + N_2$	7×10^{-17}
(R150)	$N_4^+ + N_2 \rightarrow N_2^+ + N_2 + N_2$	$2.1 \times 10^{-16} \exp(T_g/121)$
(R151)	$N_4^+ + N_2O \rightarrow N_2O^+ + N_2 + N_2$	3×10^{-16}
(R152)	$N_4^+ + N \rightarrow N^+ + N_2 + N_2$	1×10^{-17}
(R153)	$N_4^+ + NO \rightarrow NO^+ + N_2 + N_2$	3.9×10^{-16}
(R154)	$N_4^+ + NO_2 \rightarrow NO_2^+ + N_2 + N_2$	2.5×10^{-16}
(R155)	$N_4^+ + NO_2 \rightarrow NO^+ + N_2O + N_2$	5×10^{-17}
(R156)	$N_4^+ + O \rightarrow O^+ + N_2 + N_2$	2.5×10^{-16}
(R157)	$N_4^+ + O_2 \rightarrow O_2^+ + N_2 + N_2$	2.4×10^{-16}
(R158)	$N_4^+ + H_2 \rightarrow H_2^+ + N_2 + N_2$	$3 \times 10^{-16} \exp(-1800/T_g)$
(R159)	$N_4^+ + H_2O \rightarrow H_2O^+ + N_2 + N_2$	3×10^{-15}
(R160)	$O^+ + N + M \rightarrow NO^+ + M$	1×10^{-41}
(R161)	$O^+ + N_2 + M \rightarrow NO^+ + N + M$	$6 \times 10^{-41}\ (300/T_g)^2$
(R162)	$O^+ + O + M \rightarrow O_2^+ + M$	1×10^{-41}
(R163)	$O^+ + O_2 \rightarrow O_2^+ + O$	$2.1 \times 10^{-17}\ (300/T_g)^{0.5}$
(R164)	$O^+ + O_3 \rightarrow O_2^+ + O_2$	1×10^{-16}
(R165)	$O^+ + N(^2D) \rightarrow N^+ + O$	1.3×10^{-16}
(R166)	$O^+ + NO \rightarrow NO^+ + O$	1×10^{-18}
(R167)	$O^+ + NO \rightarrow O_2^+ + N$	3×10^{-18}
(R168)	$O^+ + N_2O \rightarrow N_2O^+ + O$	6.3×10^{-16}
(R169)	$O^+ + N_2O \rightarrow NO^+ + NO$	2.3×10^{-16}
(R170)	$O^+ + N_2O \rightarrow O_2^+ + N_2$	2×10^{-17}
(R171)	$O^+ + NO_2 \rightarrow NO^+ + O_2$	5×10^{-16}
(R172)	$O^+ + NO_2 \rightarrow NO_2^+ + O$	1.6×10^{-15}
(R173)	$O^+ + H \rightarrow H^+ + O$	6.8×10^{-16}
(R174)	$O^+ + H_2 \rightarrow OH^+ + H$	1.7×10^{-15}
(R175)	$O^+ + OH \rightarrow OH^+ + O$	3.3×10^{-16}
(R176)	$O^+ + OH \rightarrow O_2^+ + H$	3.6×10^{-16}
(R177)	$O^+ + H_2O \rightarrow H_2O^+ + O$	3.2×10^{-15}
(R178)	$O_2^+ + O_2 + M \rightarrow O_4^+ + M$	$5.5 \times 10^{-43}\ (300/T_g)^{2.7}$
(R179)	$O_2^+ + N \rightarrow NO^+ + O$	1.5×10^{-16}
(R180)	$O_2^+ + N_2 \rightarrow NO^+ + NO$	1×10^{-23}
(R181)	$O_2^+ + N_2O_5 \rightarrow NO_2^+ + NO_3 + O_2$	8.8×10^{-16}
(R182)	$O_2^+ + NO \rightarrow NO^+ + O_2$	4.6×10^{-16}
(R183)	$O_2^+ + NO_2 \rightarrow NO_2^+ + O_2$	6.6×10^{-16}
(R184)	$O_2^+ + NO_2 \rightarrow NO^+ + O_3$	1×10^{-17}
(R185)	$O_4^+ + O \rightarrow O_2^+ + O_3$	3×10^{-16}
(R186)	$O_4^+ + O_2 \rightarrow O_2^+ + O_2 + O_2$	$3.3 \times 10^{-12}\ (300/T_g)^4 \exp(-5030/T_g)$
(R187)	$O_4^+ + NO \rightarrow NO^+ + O_2 + O_2$	6.80×10^{-16}
(R188)	$O_4^+ + NO_2 \rightarrow NO_2^+ + O_2 + O_2$	3×10^{-16}
(R189)	$O^- + O_2 + M \rightarrow O_3^- + M$	$1.1 \times 10^{-42}\ (300/T_g)$
(R190)	$O^- + O_2(a\ ^1\Delta) \rightarrow O_2^- + O$	1×10^{-16}
(R191)	$O^- + O_3 \rightarrow O_3^- + O$	8×10^{-16}

(R192)	$O^- + N_2O \rightarrow NO^- + NO$	2×10^{-16}
(R193)	$O^- + N_2O \rightarrow N_2O^- + O$	2×10^{-18}
(R194)	$O^- + NO + M \rightarrow NO_2^- + M$	1×10^{-41}
(R195)	$O^- + NO_2 \rightarrow NO_2^- + O$	1.2×10^{-15}
(R196)	$O^- + NO_3 \rightarrow NO_3^- + O$	3×10^{-16}
(R197)	$O^- + H_2 \rightarrow OH^- + H$	3.3×10^{-17}
(R198)	$O^- + H_2O \rightarrow OH^- + OH$	1.4×10^{-15}
(R199)	$O_2^- + O \rightarrow O^- + O_2$	3.3×10^{-16}
(R200)	$O_2^- + O_2 + M \rightarrow O_4^- + M$	$3.5 \times 10^{-43}\ (300/T_g)$
(R201)	$O_2^- + O_3 \rightarrow O_3^- + O_2$	3.5×10^{-16}
(R202)	$O_2^- + N_2O \rightarrow O_3^- + N_2$	1×10^{-17}
(R203)	$O_2^- + NO_2 \rightarrow NO_2^- + O_2$	7×10^{-16}
(R204)	$O_2^- + NO_3 \rightarrow NO_3^- + O_2$	5×10^{-16}
(R205)	$O_2^- + HNO_3 \rightarrow NO_3^- + HO_2$	2.8×10^{-16}
(R206)	$O_3^- + O \rightarrow O_2^- + O_2$	1×10^{-17}
(R207)	$O_3^- + NO \rightarrow NO_2^- + O_2$	1×10^{-17}
(R208)	$O_3^- + NO \rightarrow NO_3^- + O$	1×10^{-17}
(R209)	$O_3^- + NO_2 \rightarrow NO_3^- + O_2$	2×10^{-17}
(R210)	$O_3^- + NO_2 \rightarrow NO_2^- + O_3$	7×10^{-17}
(R211)	$O_3^- + NO_3 \rightarrow NO_3^- + O_3$	5×10^{-16}
(R212)	$O_3^- + H \rightarrow OH^- + O_2$	8.4×10^{-16}
(R213)	$O_4^- + NO \rightarrow NO_3^- + O_2$	2.5×10^{-16}
(R214)	$O_4^- + O \rightarrow O^- + O_2 + O_2$	3×10^{-16}
(R215)	$O_4^- + O \rightarrow O_3^- + O_2$	4×10^{-16}
(R216)	$O_4^- + N_2 \rightarrow O_2^- + O_2 + N_2$	$1 \times 10^{-16} \exp(-1044/T_g)$
(R217)	$N_2O^+ + NO \rightarrow NO^+ + N_2O$	2.3×10^{-16}
(R218)	$N_2O^+ + N_2O \rightarrow NO^+ + NO + N_2$	1.2×10^{-17}
(R219)	$N_2O^+ + NO_2 \rightarrow NO^+ + N_2 + O_2$	4.29×10^{-16}
(R220)	$N_2O^+ + NO_2 \rightarrow NO_2^+ + N_2O$	2.21×10^{-16}
(R221)	$N_2O^+ + O_2 \rightarrow NO^+ + NO_2$	4.59×10^{-17}
(R222)	$N_2O^+ + O_2 \rightarrow O_2^+ + N_2O$	2.24×10^{-16}
(R223)	$NO^+ + N_2O_5 \rightarrow NO_2^+ + NO_2 + NO_2$	5.9×10^{-16}
(R224)	$NO^+ + O_3 \rightarrow NO_2^+ + O_2$	1×10^{-21}
(R225)	$NO^+ + N + M \rightarrow N_2O^+ + M$	$1 \times 10^{-41}\ (300/T_g)$
(R226)	$NO^- + N_2O \rightarrow NO_2^- + N_2$	2.8×10^{-20}
(R227)	$NO^- + NO_2 \rightarrow NO_2^- + NO$	3×10^{-16}
(R228)	$NO^- + NO_3 \rightarrow NO_3^- + NO$	3×10^{-16}
(R229)	$NO^- + O_2 \rightarrow O_2^- + NO$	5×10^{-16}
(R230)	$NO^- + O_3 \rightarrow O_3^- + NO$	3×10^{-16}
(R231)	$NO^- + O \rightarrow O^- + NO$	3×10^{-16}
(R232)	$NO_2^+ + NO \rightarrow NO^+ + NO_2$	2.75×10^{-16}
(R233)	$NO_2^- + N_2O_5 \rightarrow NO_3^- + NO_3 + NO$	7×10^{-16}
(R234)	$NO_2^- + NO \rightarrow NO^- + NO_2$	2.75×10^{-16}
(R235)	$NO_2^- + NO_2 \rightarrow NO_3^- + NO$	4×10^{-18}
(R236)	$NO_2^- + NO_3 \rightarrow NO_3^- + NO_2$	5×10^{-16}
(R237)	$NO_2^- + O_3 \rightarrow NO_3^- + O_2$	1.8×10^{-17}
(R238)	$NO_2^- + H \rightarrow OH^- + NO$	4×10^{-16}
(R239)	$NO_2^- + N_2O \rightarrow NO_3^- + N_2$	5×10^{-19}
(R240)	$NO_2^- + HNO_3 \rightarrow NO_3^- + HNO_2$	1.6×10^{-15}
(R241)	$NO_3^- + NO \rightarrow NO_2^- + NO_2$	3×10^{-21}
(R242)	$H^+ + O \rightarrow O^+ + H$	3.8×10^{-16}
(R243)	$H^+ + O_2 \rightarrow O_2^+ + H$	1.17×10^{-15}
(R244)	$H^+ + NO \rightarrow NO^+ + H$	1.9×10^{-15}
(R245)	$H^+ + H_2 + M \rightarrow H_3^+ + M$	3.1×10^{-41}
(R246)	$H^+ + H_2O \rightarrow H_2O^+ + H$	8.2×10^{-15}
(R247)	$H^- + N_2O \rightarrow OH^- + N_2$	1.1×10^{-15}
(R248)	$H^- + NO_2 \rightarrow NO_2^- + H$	2.9×10^{-15}
(R249)	$H^- + H_2O \rightarrow OH^- + H_2$	3.8×10^{-15}
(R250)	$H_2^+ + O_2 \rightarrow O_2^+ + H_2$	7.83×10^{-16}
(R251)	$H_2^+ + H \rightarrow H^+ + H_2$	6.4×10^{-16}
(R252)	$H_2^+ + H_2 \rightarrow H_3^+ + H$	2×10^{-15}
(R253)	$H_2^+ + H_2O \rightarrow H_3O^+ + H$	3.43×10^{-15}
(R254)	$H_2^+ + H_2O \rightarrow H_2O^+ + H_2$	3.86×10^{-15}
(R255)	$H_3^+ + O \rightarrow OH^+ + H_2$	8×10^{-16}
(R256)	$H_3^+ + H_2O \rightarrow H_3O^+ + H_2$	3×10^{-15}
(R257)	$H_3^+ + NO_2 \rightarrow NO^+ + OH + H_2$	7×10^{-16}

(R258)	$OH^+ + O_2 \rightarrow O_2^+ + OH$	5.9×10^{-16}
(R259)	$OH^+ + NO \rightarrow NO^+ + OH$	5.2×10^{-16}
(R260)	$OH^+ + NO_2 \rightarrow NO^+ + HO_2$	1.3×10^{-15}
(R261)	$OH^+ + N_2O \rightarrow N_2O^+ + OH$	2.13×10^{-16}
(R262)	$OH^+ + H_2 \rightarrow H_2O^+ + H$	9.7×10^{-16}
(R263)	$OH^+ + OH \rightarrow H_2O^+ + O$	7×10^{-16}
(R264)	$OH^+ + H_2O \rightarrow H_2O^+ + OH$	1.59×10^{-15}
(R265)	$OH^+ + H_2O \rightarrow H_3O^+ + O$	1.3×10^{-15}
(R266)	$OH^- + O_3 \rightarrow O_3^- + OH$	9×10^{-16}
(R267)	$OH^- + NO_2 \rightarrow NO_2^- + OH$	1.9×10^{-15}
(R268)	$H_2O^+ + N \rightarrow NO^+ + H_2$	1.9×10^{-16}
(R269)	$H_2O^+ + O \rightarrow O_2^+ + H_2$	5.5×10^{-17}
(R270)	$H_2O^+ + O_2 \rightarrow O_2^+ + H_2O$	4.3×10^{-16}
(R271)	$H_2O^+ + NO \rightarrow NO^+ + H_2O$	4.6×10^{-16}
(R272)	$H_2O^+ + NO_2 \rightarrow NO_2^+ + H_2O$	1.2×10^{-15}
(R273)	$H_2O^+ + H_2 \rightarrow H_3O^+ + H$	7.6×10^{-16}
(R274)	$H_2O^+ + H_2O \rightarrow H_3O^+ + OH$	1.7×10^{-15}
(R275)	$H_3O^+ + NO \rightarrow NO^+ + H + H_2O$	1.5×10^{-18}
(R276)	$H_3O^+ + N_2O_5 \rightarrow NO_2^+ + HNO_3 + H_2O$	5.5×10^{-16}
(R277)	$O^+ + O^- \rightarrow O + O$	$2 \times 10^{-13}\ (300/T_g)^{0.5}$
(R278)	$O^+ + O_2^- \rightarrow O_2 + O$	$2 \times 10^{-13}\ (300/T_g)^{0.5}$
(R279)	$O^+ + O_3^- \rightarrow O_3 + O$	$2 \times 10^{-13}\ (300/T_g)^{0.5}$
(R280)	$O^+ + O_4^- \rightarrow O_2 + O_2 + O$	1×10^{-13}
(R281)	$O^+ + N_2O^- \rightarrow N_2O + O$	$2 \times 10^{-13}\ (300/T_g)^{0.5}$
(R282)	$O^+ + NO^- \rightarrow NO + O$	$2 \times 10^{-13}\ (300/T_g)^{0.5}$
(R283)	$O^+ + NO_2^- \rightarrow NO_2 + O$	$2 \times 10^{-13}\ (300/T_g)^{0.5}$
(R284)	$O^+ + NO_3^- \rightarrow NO_3 + O$	$2 \times 10^{-13}\ (300/T_g)^{0.5}$
(R285)	$O^+ + H^- \rightarrow O + H$	$2 \times 10^{-13}\ (300/T_g)^{0.5}$
(R286)	$O^+ + OH^- \rightarrow O + OH$	$2 \times 10^{-13}\ (300/T_g)^{0.5}$
(R287)	$O_2^+ + O^- \rightarrow O + O + O$	1×10^{-13}
(R288)	$O_2^+ + O^- \rightarrow O + O_2$	$2 \times 10^{-13}\ (300/T_g)^{0.5}$
(R289)	$O_2^+ + O_2^- \rightarrow O_2 + O_2$	$2 \times 10^{-13}\ (300/T_g)^{0.5}$
(R290)	$O_2^+ + O_2^- \rightarrow O_2 + O + O$	1×10^{-13}
(R291)	$O_2^+ + O_3^- \rightarrow O_3 + O_2$	$2 \times 10^{-13}\ (300/T_g)^{0.5}$
(R292)	$O_2^+ + O_3^- \rightarrow O_3 + O + O$	1×10^{-13}
(R293)	$O_2^+ + O_4^- \rightarrow O_2 + O_2 + O_2$	1×10^{-13}
(R294)	$O_2^+ + N_2O^- \rightarrow N_2O + O_2$	$2 \times 10^{-13}\ (300/T_g)^{0.5}$
(R295)	$O_2^+ + N_2O^- \rightarrow N_2O + O + O$	1×10^{-13}
(R296)	$O_2^+ + NO^- \rightarrow NO + O_2$	$2 \times 10^{-13}\ (300/T_g)^{0.5}$
(R297)	$O_2^+ + NO^- \rightarrow NO + O + O$	1×10^{-13}
(R298)	$O_2^+ + NO_2^- \rightarrow NO_2 + O_2$	$2 \times 10^{-13}\ (300/T_g)^{0.5}$
(R299)	$O_2^+ + NO_2^- \rightarrow NO_2 + O + O$	1×10^{-13}
(R300)	$O_2^+ + NO_3^- \rightarrow NO_3 + O_2$	$2 \times 10^{-13}\ (300/T_g)^{0.5}$
(R301)	$O_2^+ + NO_3^- \rightarrow NO_3 + O + O$	1×10^{-13}
(R302)	$O_2^+ + H^- \rightarrow H + O_2$	$2 \times 10^{-13}\ (300/T_g)^{0.5}$
(R303)	$O_2^+ + H^- \rightarrow H + O + O$	1×10^{-13}
(R304)	$O_2^+ + OH^- \rightarrow OH + O_2$	$2 \times 10^{-13}\ (300/T_g)^{0.5}$
(R305)	$O_2^+ + OH^- \rightarrow OH + O + O$	1×10^{-13}
(R306)	$O_4^+ + O^- \rightarrow O + O_2 + O_2$	1×10^{-13}
(R307)	$O_4^+ + O_2^- \rightarrow O_2 + O_2 + O_2$	1×10^{-13}
(R308)	$O_4^+ + O_3^- \rightarrow O_3 + O_2 + O_2$	1×10^{-13}
(R309)	$O_4^+ + O_4^- \rightarrow O_2 + O_2 + O_2 + O_2$	1×10^{-13}
(R310)	$O_4^+ + N_2O^- \rightarrow N_2O + O_2 + O_2$	1×10^{-13}
(R311)	$O_4^+ + NO^- \rightarrow NO + O_2 + O_2$	1×10^{-13}
(R312)	$O_4^+ + NO_2^- \rightarrow NO_2 + O_2 + O_2$	1×10^{-13}
(R313)	$O_4^+ + NO_3^- \rightarrow NO_3 + O_2 + O_2$	1×10^{-13}
(R314)	$O_4^+ + H^- \rightarrow H + O_2 + O_2$	1×10^{-13}
(R315)	$O_4^+ + OH^- \rightarrow OH + O_2 + O_2$	1×10^{-13}
(R316)	$N^+ + N_2O^- \rightarrow N_2O + N$	$2 \times 10^{-13}\ (300/T_g)^{0.5}$
(R317)	$N^+ + NO^- \rightarrow NO + N$	$2 \times 10^{-13}\ (300/T_g)^{0.5}$
(R318)	$N^+ + NO_2^- \rightarrow NO_2 + N$	$2 \times 10^{-13}\ (300/T_g)^{0.5}$
(R319)	$N^+ + NO_3^- \rightarrow NO_3 + N$	$2 \times 10^{-13}\ (300/T_g)^{0.5}$
(R320)	$N^+ + O^- \rightarrow O + N$	$2 \times 10^{-13}\ (300/T_g)^{0.5}$

(R321)	$N^+ + O_2^- \rightarrow O_2 + N$	$2 \times 10^{-13}\ (300/T_g)^{0.5}$
(R322)	$N^+ + O_3^- \rightarrow O_3 + N$	$2 \times 10^{-13}\ (300/T_g)^{0.5}$
(R323)	$N^+ + O_4^- \rightarrow O_2 + O_2 + N$	1×10^{-13}
(R324)	$N^+ + H^- \rightarrow N + H$	$2 \times 10^{-13}\ (300/T_g)^{0.5}$
(R325)	$N^+ + OH^- \rightarrow N + OH$	$2 \times 10^{-13}\ (300/T_g)^{0.5}$
(R326)	$N_2^+ + N_2O^- \rightarrow N_2O + N_2$	$2 \times 10^{-13}\ (300/T_g)^{0.5}$
(R327)	$N_2^+ + N_2O^- \rightarrow N_2O + N + N$	1×10^{-13}
(R328)	$N_2^+ + NO^- \rightarrow NO + N_2$	$2 \times 10^{-13}\ (300/T_g)^{0.5}$
(R329)	$N_2^+ + NO^- \rightarrow NO + N + N$	1×10^{-13}
(R330)	$N_2^+ + NO_2^- \rightarrow NO_2 + N_2$	$2 \times 10^{-13}\ (300/T_g)^{0.5}$
(R331)	$N_2^+ + NO_2^- \rightarrow NO_2 + N + N$	1×10^{-13}
(R332)	$N_2^+ + NO_3^- \rightarrow NO_3 + N_2$	$2 \times 10^{-13}\ (300/T_g)^{0.5}$
(R333)	$N_2^+ + NO_3^- \rightarrow NO_3 + N + N$	1×10^{-13}
(R334)	$N_2^+ + O^- \rightarrow O + N + N$	1×10^{-13}
(R335)	$N_2^+ + O^- \rightarrow O + N_2$	$2 \times 10^{-13}\ (300/T_g)^{0.5}$
(R336)	$N_2^+ + O_2^- \rightarrow O_2 + N + N$	1×10^{-13}
(R337)	$N_2^+ + O_2^- \rightarrow O_2 + N_2$	$2 \times 10^{-13}\ (300/T_g)^{0.5}$
(R338)	$N_2^+ + O_3^- \rightarrow O_3 + N + N$	1×10^{-13}
(R339)	$N_2^+ + O_3^- \rightarrow O_3 + N_2$	$2 \times 10^{-13}\ (300/T_g)^{0.5}$
(R340)	$N_2^+ + O_4^- \rightarrow O_2 + O_2 + N_2$	1×10^{-13}
(R341)	$N_2^+ + H^- \rightarrow H + N_2$	$2 \times 10^{-13}\ (300/T_g)^{0.5}$
(R342)	$N_2^+ + H^- \rightarrow H + N + N$	1×10^{-13}
(R343)	$N_2^+ + OH^- \rightarrow OH + N_2$	$2 \times 10^{-13}\ (300/T_g)^{0.5}$
(R344)	$N_2^+ + OH^- \rightarrow OH + N + N$	1×10^{-13}
(R345)	$N_2O^+ + N_2O^- \rightarrow N_2O + N_2O$	$2 \times 10^{-13}\ (300/T_g)^{0.5}$
(R346)	$N_2O^+ + N_2O^- \rightarrow N_2O + N_2 + O$	1×10^{-13}
(R347)	$N_2O^+ + NO^- \rightarrow NO + N_2O$	$2 \times 10^{-13}\ (300/T_g)^{0.5}$
(R348)	$N_2O^+ + NO^- \rightarrow NO + N_2 + O$	1×10^{-13}
(R349)	$N_2O^+ + NO_2^- \rightarrow NO_2 + N_2O$	$2 \times 10^{-13}\ (300/T_g)^{0.5}$
(R350)	$N_2O^+ + NO_2^- \rightarrow NO_2 + N_2 + O$	1×10^{-13}
(R351)	$N_2O^+ + NO_3^- \rightarrow NO_3 + N_2O$	$2 \times 10^{-13}\ (300/T_g)^{0.5}$
(R352)	$N_2O^+ + NO_3^- \rightarrow NO_3 + N_2 + O$	1×10^{-13}
(R353)	$N_2O^+ + O^- \rightarrow O + N_2O$	$2 \times 10^{-13}\ (300/T_g)^{0.5}$
(R354)	$N_2O^+ + O^- \rightarrow O + N_2 + O$	1×10^{-13}
(R355)	$N_2O^+ + O_2^- \rightarrow O_2 + N_2O$	$2 \times 10^{-13}\ (300/T_g)^{0.5}$
(R356)	$N_2O^+ + O_2^- \rightarrow O_2 + N_2 + O$	1×10^{-13}
(R357)	$N_2O^+ + O_3^- \rightarrow O_3 + N_2O$	$2 \times 10^{-13}\ (300/T_g)^{0.5}$
(R358)	$N_2O^+ + O_3^- \rightarrow O_3 + N_2 + O$	1×10^{-13}
(R359)	$N_2O^+ + O_4^- \rightarrow O_2 + O_2 + N_2O$	1×10^{-13}
(R360)	$N_2O^+ + H^- \rightarrow H + N_2O$	$2 \times 10^{-13}\ (300/T_g)^{0.5}$
(R361)	$N_2O^+ + H^- \rightarrow H + N_2 + O$	1×10^{-13}
(R362)	$N_2O^+ + OH^- \rightarrow OH + N_2O$	$2 \times 10^{-13}\ (300/T_g)^{0.5}$
(R363)	$N_2O^+ + OH^- \rightarrow OH + N_2 + O$	1×10^{-13}
(R364)	$N_3^+ + N_2O^- \rightarrow N_2O + N_2 + N$	1×10^{-13}
(R365)	$N_3^+ + NO^- \rightarrow NO + N_2 + N$	1×10^{-13}
(R366)	$N_3^+ + NO_2^- \rightarrow NO_2 + N_2 + N$	1×10^{-13}
(R367)	$N_3^+ + NO_3^- \rightarrow NO_3 + N_2 + N$	1×10^{-13}
(R368)	$N_3^+ + O^- \rightarrow O + N_2 + N$	1×10^{-13}
(R369)	$N_3^+ + O_2^- \rightarrow O_2 + N_2 + N$	1×10^{-13}
(R370)	$N_3^+ + O_3^- \rightarrow O_3 + N_2 + N$	1×10^{-13}
(R371)	$N_3^+ + O_4^- \rightarrow O_2 + O_2 + N + N_2$	1×10^{-13}
(R372)	$N_3^+ + H^- \rightarrow H + N_2 + N$	1×10^{-13}
(R373)	$N_3^+ + OH^- \rightarrow OH + N_2 + N$	1×10^{-13}
(R374)	$N_4^+ + N_2O^- \rightarrow N_2O + N_2 + N_2$	1×10^{-13}
(R375)	$N_4^+ + NO^- \rightarrow NO + N_2 + N_2$	1×10^{-13}
(R376)	$N_4^+ + NO_2^- \rightarrow NO_2 + N_2 + N_2$	1×10^{-13}
(R377)	$N_4^+ + NO_3^- \rightarrow NO_3 + N_2 + N_2$	1×10^{-13}
(R378)	$N_4^+ + O^- \rightarrow O + N_2 + N_2$	1×10^{-13}
(R379)	$N_4^+ + O_2^- \rightarrow O_2 + N_2 + N_2$	1×10^{-13}
(R380)	$N_4^+ + O_3^- \rightarrow O_3 + N_2 + N_2$	1×10^{-13}
(R381)	$N_4^+ + O_4^- \rightarrow O_2 + O_2 + N_2 + N_2$	1×10^{-13}
(R382)	$N_4^+ + H^- \rightarrow H + N_2 + N_2$	1×10^{-13}
(R383)	$N_4^+ + OH^- \rightarrow OH + N_2 + N_2$	1×10^{-13}
(R384)	$NO^+ + N_2O^- \rightarrow N_2O + NO$	$2 \times 10^{-13}\ (300/T_g)^{0.5}$
(R385)	$NO^+ + N_2O^- \rightarrow N_2O + N + O$	1×10^{-13}
(R386)	$NO^+ + NO^- \rightarrow NO + NO$	$2 \times 10^{-13}\ (300/T_g)^{0.5}$

(R387)	$NO^+ + NO^- \rightarrow NO + N + O$	1×10^{-13}
(R388)	$NO^+ + NO_2^- \rightarrow NO_2 + NO$	$2 \times 10^{-13}\ (300/T_g)^{0.5}$
(R389)	$NO^+ + NO_2^- \rightarrow NO_2 + N + O$	1×10^{-13}
(R390)	$NO^+ + NO_3^- \rightarrow NO_3 + NO$	$2 \times 10^{-13}\ (300/T_g)^{0.5}$
(R391)	$NO^+ + NO_3^- \rightarrow NO_3 + N + O$	1×10^{-13}
(R392)	$NO^+ + O^- \rightarrow O + N + O$	1×10^{-13}
(R393)	$NO^+ + O^- \rightarrow O + NO$	$2 \times 10^{-13}\ (300/T_g)^{0.5}$
(R394)	$NO^+ + O_2^- \rightarrow O_2 + N + O$	1×10^{-13}
(R395)	$NO^+ + O_2^- \rightarrow O_2 + NO$	$2 \times 10^{-13}\ (300/T_g)^{0.5}$
(R396)	$NO^+ + O_3^- \rightarrow O_3 + N + O$	1×10^{-13}
(R397)	$NO^+ + O_3^- \rightarrow O_3 + NO$	$2 \times 10^{-13}\ (300/T_g)^{0.5}$
(R398)	$NO^+ + O_4^- \rightarrow O_2 + O_2 + NO$	1×10^{-13}
(R399)	$NO^+ + H^- \rightarrow H + NO$	$2 \times 10^{-13}\ (300/T_g)^{0.5}$
(R400)	$NO^+ + H^- \rightarrow H + N + O$	1×10^{-13}
(R401)	$NO^+ + OH^- \rightarrow OH + NO$	$2 \times 10^{-13}\ (300/T_g)^{0.5}$
(R402)	$NO^+ + OH^- \rightarrow OH + N + O$	1×10^{-13}
(R403)	$NO_2^+ + N_2O^- \rightarrow N_2O + NO_2$	$2 \times 10^{-13}\ (300/T_g)^{0.5}$
(R404)	$NO_2^+ + N_2O^- \rightarrow N_2O + N + O_2$	1×10^{-13}
(R405)	$NO_2^+ + NO^- \rightarrow NO + NO_2$	$2 \times 10^{-13}\ (300/T_g)^{0.5}$
(R406)	$NO_2^+ + NO^- \rightarrow NO + N + O_2$	1×10^{-13}
(R407)	$NO_2^+ + NO_2^- \rightarrow NO_2 + NO_2$	$2 \times 10^{-13}\ (300/T_g)^{0.5}$
(R408)	$NO_2^+ + NO_2^- \rightarrow NO_2 + N + O_2$	1×10^{-13}
(R409)	$NO_2^+ + NO_3^- \rightarrow NO_3 + NO_2$	$2 \times 10^{-13}\ (300/T_g)^{0.5}$
(R410)	$NO_2^+ + NO_3^- \rightarrow NO_3 + N + O_2$	1×10^{-13}
(R411)	$NO_2^+ + O^- \rightarrow O + NO_2$	$2 \times 10^{-13}\ (300/T_g)^{0.5}$
(R412)	$NO_2^+ + O^- \rightarrow O + N + O_2$	1×10^{-13}
(R413)	$NO_2^+ + O_2^- \rightarrow O_2 + NO_2$	$2 \times 10^{-13}\ (300/T_g)^{0.5}$
(R414)	$NO_2^+ + O_2^- \rightarrow O_2 + N + O_2$	1×10^{-13}
(R415)	$NO_2^+ + O_3^- \rightarrow O_3 + NO_2$	$2 \times 10^{-13}\ (300/T_g)^{0.5}$
(R416)	$NO_2^+ + O_3^- \rightarrow O_3 + N + O_2$	1×10^{-13}
(R417)	$NO_2^+ + O_4^- \rightarrow O_2 + O_2 + NO_2$	1×10^{-13}
(R418)	$NO_2^+ + H^- \rightarrow H + NO_2$	$2 \times 10^{-13}\ (300/T_g)^{0.5}$
(R419)	$NO_2^+ + H^- \rightarrow H + N + O_2$	1×10^{-13}
(R420)	$NO_2^+ + OH^- \rightarrow OH + NO_2$	$2 \times 10^{-13}\ (300/T_g)^{0.5}$
(R421)	$NO_2^+ + OH^- \rightarrow OH + N + O_2$	1×10^{-13}
(R422)	$H^+ + N_2O^- \rightarrow N_2O + H$	$2 \times 10^{-13}\ (300/T_g)^{0.5}$
(R423)	$H^+ + NO^- \rightarrow NO + H$	$2 \times 10^{-13}\ (300/T_g)^{0.5}$
(R424)	$H^+ + NO_2^- \rightarrow NO_2 + H$	$2 \times 10^{-13}\ (300/T_g)^{0.5}$
(R425)	$H^+ + NO_3^- \rightarrow NO_3 + H$	$2 \times 10^{-13}\ (300/T_g)^{0.5}$
(R426)	$H^+ + O^- \rightarrow O + H$	$2 \times 10^{-13}\ (300/T_g)^{0.5}$
(R427)	$H^+ + O_2^- \rightarrow O_2 + H$	$2 \times 10^{-13}\ (300/T_g)^{0.5}$
(R428)	$H^+ + O_3^- \rightarrow O_3 + H$	$2 \times 10^{-13}\ (300/T_g)^{0.5}$
(R429)	$H^+ + O_4^- \rightarrow O_2 + O_2 + H$	1×10^{-13}
(R430)	$H^+ + H^- \rightarrow H + H$	$2 \times 10^{-13}\ (300/T_g)^{0.5}$
(R431)	$H^+ + OH^- \rightarrow OH + H$	$2 \times 10^{-13}\ (300/T_g)^{0.5}$
(R432)	$H_2^+ + N_2O^- \rightarrow N_2O + H_2$	$2 \times 10^{-13}\ (300/T_g)^{0.5}$
(R433)	$H_2^+ + N_2O^- \rightarrow N_2O + H + H$	1×10^{-13}
(R434)	$H_2^+ + NO^- \rightarrow NO + H_2$	$2 \times 10^{-13}\ (300/T_g)^{0.5}$
(R435)	$H_2^+ + NO^- \rightarrow NO + H + H$	1×10^{-13}
(R436)	$H_2^+ + NO_2^- \rightarrow NO_2 + H_2$	$2 \times 10^{-13}\ (300/T_g)^{0.5}$
(R437)	$H_2^+ + NO_2^- \rightarrow NO_2 + H + H$	1×10^{-13}
(R438)	$H_2^+ + NO_3^- \rightarrow NO_3 + H_2$	$2 \times 10^{-13}\ (300/T_g)^{0.5}$
(R439)	$H_2^+ + NO_3^- \rightarrow NO_3 + H + H$	1×10^{-13}
(R440)	$H_2^+ + O^- \rightarrow O + H + H$	1×10^{-13}
(R441)	$H_2^+ + O^- \rightarrow O + H_2$	$2 \times 10^{-13}\ (300/T_g)^{0.5}$
(R442)	$H_2^+ + O_2^- \rightarrow O_2 + H + H$	1×10^{-13}
(R443)	$H_2^+ + O_2^- \rightarrow O_2 + H_2$	$2 \times 10^{-13}\ (300/T_g)^{0.5}$
(R444)	$H_2^+ + O_3^- \rightarrow O_3 + H + H$	1×10^{-13}
(R445)	$H_2^+ + O_3^- \rightarrow O_3 + H_2$	$2 \times 10^{-13}\ (300/T_g)^{0.5}$
(R446)	$H_2^+ + O_4^- \rightarrow O_2 + O_2 + H_2$	1×10^{-13}
(R447)	$H_2^+ + H^- \rightarrow H + H_2$	$2 \times 10^{-13}\ (300/T_g)^{0.5}$
(R448)	$H_2^+ + H^- \rightarrow H + H + H$	1×10^{-13}
(R449)	$H_2^+ + OH^- \rightarrow OH + H_2$	$2 \times 10^{-13}\ (300/T_g)^{0.5}$

(R450)	$H_2^+ + OH^- \rightarrow OH + H + H$	1×10^{-13}
(R451)	$H_3^+ + N_2O^- \rightarrow N_2O + H + H_2$	1×10^{-13}
(R452)	$H_3^+ + NO^- \rightarrow NO + H + H_2$	1×10^{-13}
(R453)	$H_3^+ + NO_2^- \rightarrow NO_2 + H + H_2$	1×10^{-13}
(R454)	$H_3^+ + NO_3^- \rightarrow NO_3 + H + H_2$	1×10^{-13}
(R455)	$H_3^+ + O^- \rightarrow O + H + H_2$	1×10^{-13}
(R456)	$H_3^+ + O_2^- \rightarrow O_2 + H + H_2$	1×10^{-13}
(R457)	$H_3^+ + O_3^- \rightarrow O_3 + H + H_2$	1×10^{-13}
(R458)	$H_3^+ + O_4^- \rightarrow O_2 + O_2 + H + H_2$	1×10^{-13}
(R459)	$H_3^+ + H^- \rightarrow H + H + H_2$	1×10^{-13}
(R460)	$H_3^+ + OH^- \rightarrow OH + H + H_2$	1×10^{-13}
(R461)	$OH^+ + N_2O^- \rightarrow N_2O + OH$	$2 \times 10^{-13}\ (300/T_g)^{0.5}$
(R462)	$OH^+ + N_2O^- \rightarrow N_2O + O + H$	1×10^{-13}
(R463)	$OH^+ + NO^- \rightarrow NO + OH$	$2 \times 10^{-13}\ (300/T_g)^{0.5}$
(R464)	$OH^+ + NO^- \rightarrow NO + O + H$	1×10^{-13}
(R465)	$OH^+ + NO_2^- \rightarrow NO_2 + OH$	$2 \times 10^{-13}\ (300/T_g)^{0.5}$
(R466)	$OH^+ + NO_2^- \rightarrow NO_2 + O + H$	1×10^{-13}
(R467)	$OH^+ + NO_3^- \rightarrow NO_3 + OH$	$2 \times 10^{-13}\ (300/T_g)^{0.5}$
(R468)	$OH^+ + NO_3^- \rightarrow NO_3 + O + H$	1×10^{-13}
(R469)	$OH^+ + O^- \rightarrow O + O + H$	1×10^{-13}
(R470)	$OH^+ + O^- \rightarrow O + OH$	$2 \times 10^{-13}\ (300/T_g)^{0.5}$
(R471)	$OH^+ + O_2^- \rightarrow O_2 + O + H$	1×10^{-13}
(R472)	$OH^+ + O_2^- \rightarrow O_2 + OH$	$2 \times 10^{-13}\ (300/T_g)^{0.5}$
(R473)	$OH^+ + O_3^- \rightarrow O_3 + O + H$	1×10^{-13}
(R474)	$OH^+ + O_3^- \rightarrow O_3 + OH$	$2 \times 10^{-13}\ (300/T_g)^{0.5}$
(R475)	$OH^+ + O_4^- \rightarrow O_2 + O_2 + OH$	1×10^{-13}
(R476)	$OH^+ + H^- \rightarrow H + OH$	$2 \times 10^{-13}\ (300/T_g)^{0.5}$
(R477)	$OH^+ + H^- \rightarrow H + O + H$	1×10^{-13}
(R478)	$OH^+ + OH^- \rightarrow OH + OH$	$2 \times 10^{-13}\ (300/T_g)^{0.5}$
(R479)	$OH^+ + OH^- \rightarrow OH + O + H$	1×10^{-13}
(R480)	$H_2O^+ + N_2O^- \rightarrow N_2O + H_2O$	$2 \times 10^{-13}\ (300/T_g)^{0.5}$
(R481)	$H_2O^+ + N_2O^- \rightarrow N_2O + OH + H$	1×10^{-13}
(R482)	$H_2O^+ + NO^- \rightarrow NO + H_2O$	$2 \times 10^{-13}\ (300/T_g)^{0.5}$
(R483)	$H_2O^+ + NO^- \rightarrow NO + OH + H$	1×10^{-13}
(R484)	$H_2O^+ + NO_2^- \rightarrow NO_2 + H_2O$	$2 \times 10^{-13}\ (300/T_g)^{0.5}$
(R485)	$H_2O^+ + NO_2^- \rightarrow NO_2 + OH + H$	1×10^{-13}
(R486)	$H_2O^+ + NO_3^- \rightarrow NO_3 + H_2O$	$2 \times 10^{-13}\ (300/T_g)^{0.5}$
(R487)	$H_2O^+ + NO_3^- \rightarrow NO_3 + OH + H$	1×10^{-13}
(R488)	$H_2O^+ + O^- \rightarrow O + OH + H$	1×10^{-13}
(R489)	$H_2O^+ + O^- \rightarrow O + H_2O$	$2 \times 10^{-13}\ (300/T_g)^{0.5}$
(R490)	$H_2O^+ + O_2^- \rightarrow O_2 + OH + H$	1×10^{-13}
(R491)	$H_2O^+ + O_2^- \rightarrow O_2 + H_2O$	$2 \times 10^{-13}\ (300/T_g)^{0.5}$
(R492)	$H_2O^+ + O_3^- \rightarrow O_3 + OH + H$	1×10^{-13}
(R493)	$H_2O^+ + O_3^- \rightarrow O_3 + H_2O$	$2 \times 10^{-13}\ (300/T_g)^{0.5}$
(R494)	$H_2O^+ + O_4^- \rightarrow O_2 + O_2 + H_2O$	1×10^{-13}
(R495)	$H_2O^+ + H^- \rightarrow H + H_2O$	$2 \times 10^{-13}\ (300/T_g)^{0.5}$
(R496)	$H_2O^+ + H^- \rightarrow H + OH + H$	1×10^{-13}
(R497)	$H_2O^+ + OH^- \rightarrow OH + H_2O$	$2 \times 10^{-13}\ (300/T_g)^{0.5}$
(R498)	$H_2O^+ + OH^- \rightarrow OH + OH + H$	1×10^{-13}
(R499)	$H_3O^+ + N_2O^- \rightarrow N_2O + H_2O + H$	1×10^{-13}
(R500)	$H_3O^+ + NO^- \rightarrow NO + H_2O + H$	1×10^{-13}
(R501)	$H_3O^+ + NO_2^- \rightarrow NO_2 + H_2O + H$	1×10^{-13}
(R502)	$H_3O^+ + NO_3^- \rightarrow NO_3 + H_2O + H$	1×10^{-13}
(R503)	$H_3O^+ + O^- \rightarrow O + H_2O + H$	1×10^{-13}
(R504)	$H_3O^+ + O_2^- \rightarrow O_2 + H_2O + H$	1×10^{-13}
(R505)	$H_3O^+ + O_3^- \rightarrow O_3 + H_2O + H$	1×10^{-13}
(R506)	$H_3O^+ + O_4^- \rightarrow O_2 + O_2 + H_2O + H$	1×10^{-13}
(R507)	$H_3O^+ + H^- \rightarrow H + H_2O + H$	1×10^{-13}
(R508)	$H_3O^+ + OH^- \rightarrow OH + H_2O + H$	1×10^{-13}
(R509)	$N + N + M \rightarrow N_2 + M$	$8.3 \times 10^{-46} \exp(500/T_g)$
(R510)	$N + NO \rightarrow N_2 + O$	$2.1 \times 10^{-17} \exp(100/T_g)$
(R511)	$N + NO_2 \rightarrow N_2O + O$	$5.8 \times 10^{-18} \exp(220/T_g)$
(R512)	$N + NO_2 \rightarrow N_2 + O + O$	9.1×10^{-19}
(R513)	$N + NO_2 \rightarrow NO + NO$	6×10^{-19}
(R514)	$N + NO_2 \rightarrow N_2 + O_2$	7×10^{-19}
(R515)	$N + O + M \rightarrow NO + M$	$6.3 \times 10^{-45} \exp(140/T_g)$

(R516)	$N + O_2 \rightarrow NO + O$	$1.5 \times 10^{-17} \exp(-3600/T_g)$
(R517)	$N + O_3 \rightarrow NO + O_2$	5×10^{-22}
(R518)	$N + OH \rightarrow H + NO$	7.5×10^{-17}
(R519)	$N + HO_2 \rightarrow NO + OH$	$1.7 \times 10^{-17} \exp(-1000/T_g)$
(R520)	$N(^2D) + N_2 \rightarrow N + N_2$	$5 \times 10^{-18} \exp(-1620/T_g)$
(R521)	$N(^2D) + N_2O \rightarrow N_2 + NO$	$1.5 \times 10^{-17} \exp(-570/T_g)$
(R522)	$N(^2D) + NO \rightarrow N_2O$	6×10^{-17}
(R523)	$N(^2D) + NO \rightarrow O + N_2$	4.5×10^{-17}
(R524)	$N(^2D) + O \rightarrow N + O$	7×10^{-19}
(R525)	$N(^2D) + O_2 \rightarrow NO + O$	$1.5 \times 10^{-18} (T_g/300)^{0.5}$
(R526)	$N(^2D) + O_2 \rightarrow NO + O(^1D)$	$6 \times 10^{-18} (T_g/300)^{0.5}$
(R527)	$N_2(A\,^3\Sigma) + N_2 \rightarrow N_2 + N_2$	2.2×10^{-20}
(R528)	$N_2(A\,^3\Sigma) + N_2(A\,^3\Sigma) \rightarrow N_2(B\,^3\Pi) + N_2$	4×10^{-16}
(R529)	$N_2(A\,^3\Sigma) + N_2O \rightarrow O + N_2 + N_2$	8×10^{-17}
(R530)	$N_2(A\,^3!\Sigma) + N_2O \rightarrow NO + N + N_2$	8×10^{-17}
(R531)	$N_2(A\,^3\Sigma) + NO_2 \rightarrow N_2 + NO + O$	1.3×10^{-17}
(R532)	$N_2(A\,^3\Sigma) + O_2 \rightarrow N_2 + O + O$	$5 \times 10^{-18} \exp(-210/T_g)$
(R533)	$N_2(A\,^3\Sigma) + O_2 \rightarrow O_2(a\,^1\Delta) + N_2$	1×10^{-18}
(R534)	$N_2(A\,^3\Sigma) + N \rightarrow N + N_2$	5×10^{-17}
(R535)	$N_2(A\,^3\Sigma) + O \rightarrow NO + N(^2D)$	7×10^{-18}
(R536)	$N_2(A\,^3\Sigma) + O \rightarrow O(^1D) + N_2$	2.3×10^{-17}
(R537)	$N_2(A\,^3\Sigma) + H_2O \rightarrow H + OH + N_2$	5×10^{-20}
(R538)	$N_2(B\,^3\Pi) + N_2 \rightarrow N_2(A\,^3\Sigma) + N_2$	5×10^{-17}
(R539)	$N_2(B\,^3\Pi) + \rightarrow N_2(A\,^3\Sigma)$	1.25×10^{5}
(R540)	$N_2(B\,^3\Pi) + NO \rightarrow N_2(A\,^3\Sigma) + NO$	2.4×10^{-16}
(R541)	$N_2(B\,^3\Pi) + O_2 \rightarrow N_2 + O + O$	3×10^{-16}
(R542)	$N_2(B\,^3\Pi) + H_2 \rightarrow N_2(A\,^3\Sigma) + H_2$	2.5×10^{-17}
(R543)	$O + O + M \rightarrow O_2 + M$	$3.2 \times 10^{-47} \exp(900/T_g)$
(R544)	$O + O_2 + M \rightarrow O_3 + M$	$3.4 \times 10^{-46} (300/T_g)^{1.2}$
(R545)	$O + O_3 \rightarrow O_2 + O_2$	$8 \times 10^{-18} \exp(-2060/T_g)$
(R546)	$O + NO + M \rightarrow NO_2 + M$	$1 \times 10^{-43} (300/T_g)^{1.6}$
(R547)	$O + NO_2 \rightarrow NO + O_2$	$6.5 \times 10^{-18} \exp(120/T_g)$
(R548)	$O + NO_2 + M \rightarrow NO_3 + M$	$9 \times 10^{-44} (300/T_g)^{2}$
(R549)	$O + NO_3 \rightarrow O_2 + NO_2$	1.7×10^{-17}
(R550)	$O + H + M \rightarrow OH + M$	1.62×10^{-44}
(R551)	$O + OH \rightarrow H + O_2$	$2.2 \times 10^{-17} \exp(-350/T_g)$
(R552)	$O + H_2O_2 \rightarrow OH + HO_2$	$3.3 \times 10^{-17} \exp(-2950/T_g)$
(R553)	$O + HO_2 \rightarrow OH + O_2$	$8.3 \times 10^{-17} \exp(-500/T_g)$
(R554)	$O + HNO \rightarrow OH + NO$	5.99×10^{-17}
(R555)	$O + HNO_2 \rightarrow NO_2 + OH$	$2 \times 10^{-17} \exp(-3000/T_g)$
(R556)	$O(^1D) + O_2 \rightarrow O + O_2$	$6.4 \times 10^{-18} \exp(67/T_g)$
(R557)	$O(^1D) + O \rightarrow O + O$	8×10^{-18}
(R558)	$O(^1D) + O_2(a\,^1\Delta) \rightarrow O + O_2$	1×10^{-17}
(R559)	$O(^1D) + O_2 \rightarrow O + O_2(a\,^1\Delta)$	1×10^{-18}
(R560)	$O(^1D) + O_3 \rightarrow O + O + O_2$	1.2×10^{-16}
(R561)	$O(^1D) + O_3 \rightarrow O_2 + O_2$	1.2×10^{-16}
(R562)	$O(^1D) + N_2 \rightarrow O + N_2$	$1.8 \times 10^{-17} \exp(107/T_g)$
(R563)	$O(^1D) + N_2 + M \rightarrow N_2O + M$	9×10^{-49}
(R564)	$O(^1D) + N_2O \rightarrow N_2 + O_2$	4.4×10^{-17}
(R565)	$O(^1D) + N_2O \rightarrow NO + NO$	7.2×10^{-17}
(R566)	$O(^1D) + NO \rightarrow O + NO$	4×10^{-17}
(R567)	$O(^1D) + NO_2 \rightarrow NO + O_2$	1.4×10^{-16}
(R568)	$O(^1D) + H_2 \rightarrow OH + H$	1.1×10^{-16}
(R569)	$O(^1D) + H_2O \rightarrow OH + OH$	2.2×10^{-16}
(R570)	$O_2(a\,^1\Delta) + O_2 \rightarrow O_2 + O_2$	$3.8 \times 10^{-24} \exp(-205/T_g)$
(R571)	$O_2(a\,^1\Delta) + O_3 \rightarrow O + O_2 + O_2$	$5.2 \times 10^{-17} \exp(-2840/T_g)$
(R572)	$O_2(a\,^1\Delta) + M \rightarrow O_2 + M$	8×10^{-27}
(R573)	$O_2(a\,^1\Delta) + NO \rightarrow O_2 + NO$	2.5×10^{-17}
(R574)	$O_2(a\,^1\Delta) + N_2 \rightarrow O_2 + N_2$	1.5×10^{-24}
(R575)	$O_3 + NO \rightarrow NO_2 + O_2$	$1.8 \times 10^{-18} \exp(-1370/T_g)$
(R576)	$O_3 + NO_2 \rightarrow NO_3 + O_2$	$1.4 \times 10^{-19} \exp(-2470/T_g)$
(R577)	$O_3 + M \rightarrow O + O_2 + M$	$3.92 \times 10^{-16} \exp(-11\,400/T_g)$
(R578)	$O_3 + H \rightarrow OH + O_2$	$2.8 \times 10^{-17} (T_g/300)^{0.75}$

(R579)	$O_3 + OH \rightarrow HO_2 + O_2$	$1.6 \times 10^{-18} \exp(-1000/T_g)$
(R580)	$O_3 + HO_2 \rightarrow OH + O_2 + O_2$	$1.4 \times 10^{-20} \exp(-600/T_g)$
(R581)	$NO + NO_2 + M \rightarrow N_2O_3 + M$	$3.09 \times 10^{-46} \ (300/T_g)^{7.7}$
(R582)	$NO + NO_3 \rightarrow NO_2 + NO_2$	$1.8 \times 10^{-17} \exp(110/T_g)$
(R583)	$NO + OH + M \rightarrow HNO_2 + M$	$7.4 \times 10^{-43} \ (300/T_g)^{2.4}$
(R584)	$NO + H + M \rightarrow HNO + M$	$1 \times 10^{-44} \exp(300/T_g)$
(R585)	$NO + HO_2 \rightarrow OH + NO_2$	$3.4 \times 10^{-18} \exp(270/T_g)$
(R586)	$NO + HO_2 \rightarrow O_2 + HNO$	$3.3 \times 10^{-19} \exp(-1000/T_g)$
(R587)	$NO_2 + NO_2 + M \rightarrow N_2O_4 + M$	$1.17 \times 10^{-45} \ (300/T_g)^{3.8}$
(R588)	$NO_2 + NO_3 + M \rightarrow N_2O_5 + M$	$2.8 \times 10^{-42} \ (300/T_g)^{3.5}$
(R589)	$NO_2 + NO_3 \rightarrow NO_2 + NO + O_2$	$2.3 \times 10^{-19} \exp(-1600/T_g)$
(R590)	$NO_2 + H \rightarrow OH + NO$	1.47×10^{-16}
(R591)	$NO_2 + OH + M \rightarrow HNO_3 + M$	$2.2 \times 10^{-42} \ (300/T_g)^{2.9}$
(R592)	$NO_3 + NO_3 \rightarrow NO_2 + NO_2 + O_2$	$5 \times 10^{-18} \exp(-3000/T_g)$
(R593)	$NO_3 + H \rightarrow OH + NO_2$	$5.8 \times 10^{-16} \exp(-750/T_g)$
(R594)	$NO_3 + OH \rightarrow HO_2 + NO_2$	2×10^{-17}
(R595)	$NO_3 + HO_2 \rightarrow NO_2 + OH + O_2$	4.8×10^{-18}
(R596)	$NO_3 + HO_2 \rightarrow HNO_3 + O_2$	9.2×10^{-19}
(R597)	$N_2O_3 + M \rightarrow NO + NO_2 + M$	$1.03 \times 10^{-16} \exp(-2628/T_g)$
(R598)	$N_2O_4 + M \rightarrow NO_2 + NO_2 + M$	$1.09 \times 10^{-13} \exp(-4952/T_g)$
(R599)	$N_2O_5 + M \rightarrow NO_2 + NO_3 + M$	$1 \times 10^{-9} \ (300/T_g)^{3.5} \exp(-11\,000/T_g)$
(R600)	$H + O_2 + M \rightarrow HO_2 + M$	$5.4 \times 10^{-44} \ (T_g/300)^{-1.8}$
(R601)	$H + H + M \rightarrow H_2 + M$	$1.8 \times 10^{-42}/T_g$
(R602)	$H + OH + M \rightarrow H_2O + M$	$6.1 \times 10^{-38}/T_g^2$
(R603)	$H + H_2O_2 \rightarrow OH + H_2O$	$1.69 \times 10^{-17} \exp(-1800/T_g)$
(R604)	$H + H_2O_2 \rightarrow HO_2 + H_2$	$2.8 \times 10^{-18} \exp(-1900/T_g)$
(R605)	$H + HO_2 \rightarrow H_2 + O_2$	5.6×10^{-18}
(R606)	$H + HO_2 \rightarrow O + H_2O$	2.4×10^{-18}
(R607)	$H + HO_2 \rightarrow OH + OH$	$4.2 \times 10^{-16} \exp(-950/T_g)$
(R608)	$H + HNO \rightarrow NO + H_2$	$3 \times 10^{-17} \exp(-500/T_g)$
(R609)	$H + HNO_2 \rightarrow NO_2 + H_2$	$2 \times 10^{-17} \exp(-3700/T_g)$
(R610)	$H + HNO_3 \rightarrow NO_2 + H_2O$	$1.39 \times 10^{-20} \ (T_g/298)^{3.29} \exp(-3160/T_g)$
(R611)	$H_2 + OH \rightarrow H + H_2O$	$3.2 \times 10^{-17} \exp(-2600/T_g)$
(R612)	$OH + OH \rightarrow O + H_2O$	$8.8 \times 10^{-18} \exp(-503/T_g)$
(R613)	$OH + OH + M \rightarrow H_2O_2 + M$	$6.9 \times 10^{-43} \ (T_g/300)^{-0.8}$
(R614)	$OH + HO_2 \rightarrow O_2 + H_2O$	$4.8 \times 10^{-17} \exp(250/T_g)$
(R615)	$OH + H_2O_2 \rightarrow HO_2 + H_2O$	$2.9 \times 10^{-18} \exp(-160/T_g)$
(R616)	$OH + HNO \rightarrow NO + H_2O$	$8 \times 10^{-17} \exp(-500/T_g)$
(R617)	$OH + HNO_2 \rightarrow NO_2 + H_2O$	$1.8 \times 10^{-17} \exp(-390/T_g)$
(R618)	$OH + HNO_3 \rightarrow NO_3 + H_2O$	$1.5 \times 10^{-20} \exp(650/T_g)$
(R619)	$HO_2 + HO_2 \rightarrow H_2O_2 + O_2$	$2.2 \times 10^{-19} \exp(600/T_g)$
(R620)	$HNO + O_2 \rightarrow NO + HO_2$	$5.25 \times 10^{-18} \exp(-1510/T_g)$
(R621)	$HNO + O_2 \rightarrow NO_2 + OH$	1.66×10^{-21}
(R622)	$HNO + HNO \rightarrow N_2O + H_2O$	$1.4 \times 10^{-21} \exp(-1600/T_g)$
(R623)	$HNO_2 + HNO_2 \rightarrow NO + NO_2 + H_2O$	1×10^{-26}
(R624)	$HNO_2 + HNO_3 \rightarrow NO_2 + NO_2 + H_2O$	1.6×10^{-23}